Aus dem Universitätsklinikum Heidelberg
Geschäftsführender Direktor: Prof. Dr. Ingo Autenrieth

Klinik für Herzchirurgie
Ärztlicher Direktor: Prof. Dr. med. Matthias Karck

in Zusammenarbeit mit der Klinik für Kardiologie, Angiologie, Pneumologie
Ärztlicher Direktor: Prof. Dr. Norbert Frey

Patient-specific hemodynamic simulators for cardiovascular therapies

Inauguraldissertation
zur Erlangung des
Doctor scientiarum humanarum (Dr. sc. hum.)
an der
Medizinischen Fakultät Heidelberg
der
Ruprecht-Karls-Universität

Vorgelegt von
M.Sc. Roger Frederick Karl
aus Mannheim
2024

Dekan: Herr Prof. Dr. Michael Boutros
Doktormutter: Frau Jun. Prof. Dr. Sandy Engelhardt

Contents

List of Figures

List of Tables

Abbreviations

AS-R	Aortic simulator requirements
2C-2D	2 velocity components in a 2 dimensional field
CT	Computed tomography
CTA	Computed tomography angiography
DICOM	Digital Imaging and Communications in Medicine
DSA	Digital subtraction angiography
MIMVS	Minimally invasive mitral valve surgery
MVS-R	Mitral valve simulator requirements
PIV	Particle image velocimetry
PISA	Proximal isovelocity surface area
TAAD	Type A aortic dissection
TBAD	Type B aortic dissection
TEER	Transcatheter edge-to-edge repair
TEE	Transesophageal echocardiography
TEVAR	Thoracic endovascular aortic repair
USB	Universal serial bus

Symbol	Quantity	Unit
HR	Heart rate in beats per minute	[bpm]
CO	Cardiac output	[l/min]
CVC	Compliance volume compression	[ml]
EROa	Effective regurgitation orifice area	[mm^2]
μ	Hounsfield-Unit	[HU]
P	Pressure	[Pa]
$\mathbf{r}_{PISA}$	Radius of the proximal isovelocity surface area	[mm]
RF	Regurgitation fraction	[%]
RFlow	Regurgitation flow	[ml/s]
RVol	Regurgitation volume	[ml]
SBP	Systolic blood pressure	[mmHg]
SV	Stroke volume	[ml]
$\mathbf{V}_a$	Aliasing speed / Nyquist-Limit	[m/s]
$\mathbf{V}_{max}$	Maximum regurgitation speed	[m/s]
VTI	Velocity time integral	[mm]

1 Introduction

1.1 Motivation

Cardiovascular diseases are the most common causes of death worldwide (Roth et al., 2020). Representative examples include the insufficiency of the mitral valve, called mitral regurgitation, and type B aortic dissection (TBAD). Besides medication, both diseases are commonly treated with surgical and interventional approaches. For mitral regurgitation, procedures such as minimally invasive mitral valve surgery (MIMVS) and transcatheter edge-to-edge repair (TEER) are employed (Girdauskas et al., 2019; Flint et al., 2021). Thoracic endovascular aortic repair (TEVAR) is a commonly applied procedure for TBAD (Alfson and Ham, 2017). These procedures are highly complex, require years of training, and need regular practice to maintain a consistent level of proficiency (Chikwe et al., 2017; Chhatriwalla et al., 2019; Gennai et al., 2022).

Accumulating adequate experience requires accessible training opportunities. However, the absence of training modalities poses a significant challenge in the education of physicians, particularly for intricate procedures as mentioned above. In clinical settings, it is a common practice for initial training to involve live patients, under direct supervision by an experienced physician. Regular practice not only permits experience to be gained but also a consistently high level of performance to be maintained. It is widely recognized that centers with high procedure volumes are associated with improved outcomes (Chikwe et al., 2017; Chhatriwalla et al., 2019; Gennai et al., 2022). Therefore, there is also a demand for training methods targeting experienced physicians to ensure their proficiency remains at its peak.

Potential training modalities include practicing on animals or utilizing *in-vitro* training simulators. However, animal training is cost-intensive and raises ethical concerns, hampering its use in clinical routine (Simkin et al., 2017). Moreover, not all pathologies, such as aortic dissections or ischemic mitral regurgitation, can be easily replicated in animal models. The use of *in-vitro* simulators is also scarce, mainly owing to the challenges of recreating a realistic environment and replicating different potentially patient-specific pathologies.

During TEER, MIMVS, and TEVAR, many unforeseen complications can occur, depending on the patient and specific disease manifestation. TEER might not achieve adequate mitral valve repair (García-Villarreal, 2022), TEVAR could result in unintentional great vessel coverage (Chen et al., 2020), or MIMVS may include improper annuloplasty ring sizing (Bothe et al., 2013). Consequently, in addition to the educational needs, a need for patient-specific

planning solutions arises. These could address queries such as: Is MIMVS or TEER the optimal choice for the patient? How many clips are required? Which annuloplasty ring size is most suitable? What stent-graft should be selected? What potential, unforeseen complications might arise?

Diagnosis and patient-specific planning involve precise medical imaging (Sengupta et al., 2021). With the obtained images and information, the patient is diagnosed, potentially leading to the creation of precise models, for instance patient-specific mitral valve models. Inaccurate medical imaging can result in incorrect diagnoses and potentially lead to misguided treatment decisions. Notably, transesophageal echocardiography (TEE) heavily relies on user proficiency and is linked to significant underestimation of mitral regurgitation (Frerker et al., 2022; Coisne et al., 2002). Nevertheless, it is extensively utilized for diagnosing mitral regurgitation, guiding treatment decisions, providing navigational guidance during TEER, and assessing therapy outcomes (Enriquez-Sarano et al., 2005; Lancellotti et al., 2010).

Innovative and reproducible methodologies are needed that provide avenues for training, patient-specific planning, and fundamental research questions for cardiovascular diseases such as mitral regurgitation and TBAD.

1.2 Objectives

The primary goals of this thesis encompassed the development and validation of a physical hemodynamic simulator, enabling realistic training, patient-specific planning, and fundamental research on mitral valve pathologies (I). Then, using the established simulator, this thesis aimed to assess the accuracy of the flow convergence method of TEE for quantifying mitral regurgitation (II). Finally, I aimed to extend the creation of a realistic hemodynamic environment from a core structure, such as the heart, to a peripheral tubular structure like the aorta. My objective was to establish and validate a simulator that could serve as a tool for training and patient-specific planning of TEVAR procedures to treat TBAD (III). To meet these objectives, as visualized in Figure 1.1 the following considerations were made:

(I) Designing and validating a simulator for mitral valve interventions: Realistic training and planning of procedures like MIMVS and TEER necessitate a hemodynamic environment resembling the *in-vivo* hemodynamics. I aimed to achieve this by designing a hemodynamic simulator that emulates the left heart, creating authentic pressures and flows across the mitral valve. Moreover, the simulator should facilitate the accurate execution of MIMVS and TEER, including the incorporation of necessary medical imaging such as TEE.

(II) Assessing the flow convergence method using particle image velocimetry: The evaluation of the flow convergence method for quantifying mitral regurgitation mandates a reproducible hemodynamic setting, coupled with an alternative non-invasive imaging modality

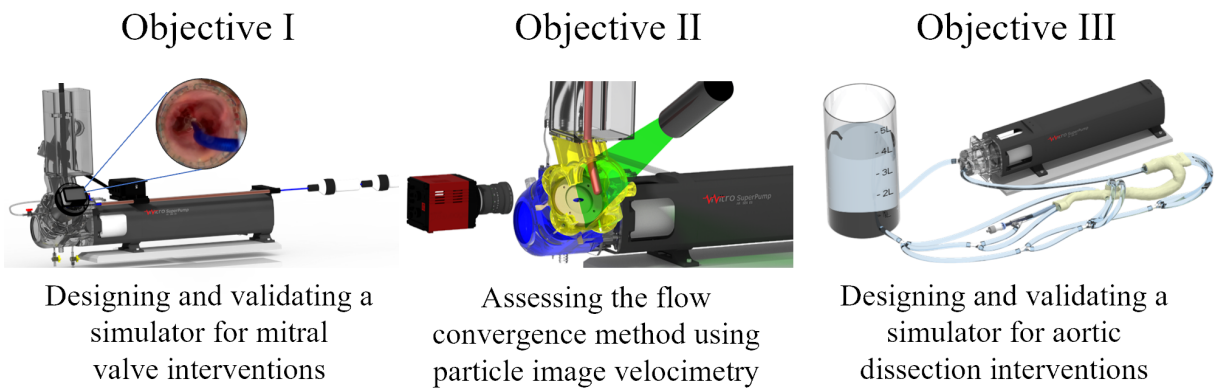

Figure 1.1: Visualization of the objectives of this thesis.

for comparison. Accordingly, the established mitral valve simulator (objective I) was used as a research tool to provide the required hemodynamic environment. Particle image velocimetry (PIV), a precise non-invasive technique inapplicable within human subjects but compatible with *in-vitro* settings provided by the mitral valve simulator, was selected to be compared to the flow convergence method.

(III) Designing and validating a simulator for aortic dissection interventions: The training and planning of TEVAR to treat TBAD require a hemodynamic environment resembling known *in-vivo* conditions. This objective was pursued by designing a pulsatile flow-loop, facilitating the assessment and execution of catheter-based procedures.

1.3 Medical and technical background

The medical background focuses on the mitral valve, aorta, and pathologies related, namely mitral regurgitation and TBAD, as well as their treatments: MIMVS, TEER, and TEVAR. Medical imaging techniques, such as TEE, computed tomography angiography (CTA), and digital subtraction angiography (DSA) are required to diagnose and characterize the pathologies mentioned above and will also be outlined. The technical background comprises the 3D-printing methods used to manufacture the simulators, as well as PIV, a non-medical imaging technology used to assess the flow convergence method.

1.3.1 Mitral valve

This section briefly summarizes the essentials of the mitral valve for this thesis. It comprises the anatomy and function of the mitral valve, characterizes mitral valve insufficiency, and describes the possible treatments MIMVS and TEER.

Anatomy and function

This section makes references to reputable medical sources, including Carpentier (2010) and Kirklin (2013). For a more comprehensive understanding of topics related to the heart and mitral valve surgery, interested readers are encouraged to consult these authoritative works.

Anatomy

The mitral valve is a bicuspid one-way heart valve located within the left part of the heart between the left atrium and the left ventricle. It plays an important role in leading the oxygen-rich blood from the lung to the aorta (Topilsky, 2020).

An overview of the mitral valve anatomy is displayed in Figure 1.2. The mitral valve is comprised of the mitral annulus, anterior and posterior leaflets, chordae tendineae, and papillary muscles (Kirklin, 2013, p. 16-18, Carpentier, 2010, p. 27-39). The mitral annulus encloses the leaflets (Figure 1.2a) and is defined as the junction between the left atrium, left ventricle, and leaflets (Figure 1.2b). It consists of densely packed parallel collagen fibers and has a saddle shape. It stabilizes the mitral valve and is essential for surgeons to place their stitches with sufficient hold (Carpentier, 2010, p. 28-30).

The anterior and posterior leaflets, covering 25 % and 75 % of the orifice, respectively, are each divided into three segments, A1 - A3, and P1 - P3 (Figure 1.2a) (Carpentier, 2010, p. 30-33). The leaflets are connected to the mitral annulus and interconnected at the anterior and posterior commissure. The leaflets touch during systole at the coaptation line, a U-shaped line parallel to the posterior part of the mitral annulus (Figure 1.2a-c). The length of coaptation perpendicular to the annulus plane is 7 - 9 mm, resulting in a leaflet area that is 1.5 to 2 times larger than the mitral annulus area, ensuring proper sealing (Carpentier, 2010, p. 30-33).

The tendons connecting the leaflets and the papillary muscles are called chordae tendineae. Their main function is to transfer the forces between leaflets and papillary muscles, which ensures proper opening and closing of the mitral valve (Carpentier, 2010, p. 33-36). About 4 - 12 chordae tendineae originate from the papillary muscles and branch into 12 - 80 chordae connecting to the leaflets (Figure 1.2c) (Kirklin, 2013, p. 16-18). According to their site of insertion, they are classified into three types, marginal chordae are attached to the edge of the leaflets, intermediary chordae are attached to the ventricular surface of the leaflet, and basal chordae are attached to the commissures and the base of the posterior leaflets (Figure 1.2b). Basal chordae tendineae may also originate from the ventricular wall (Carpentier, 2010, p. 33-36).

The papillary muscles influence the function of the mitral valve by applying force on the chordae and consequently preventing the leaflets from prolapsing during systole and open-

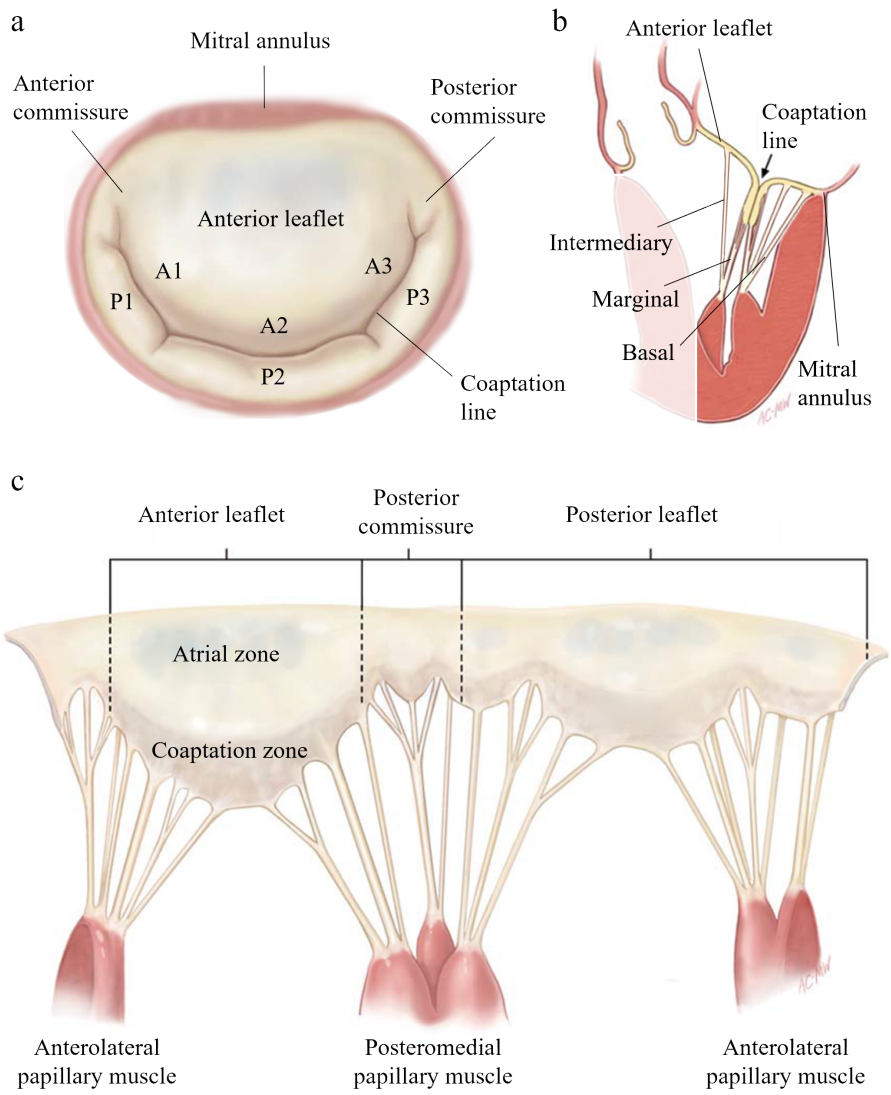

Figure 1.2: The anatomy of the mitral valve. The mitral valve is displayed in a) atrial, b) ventricular cross-section, and c) unfolded view. This figure was originally published in Carpentier (2010), adapted and reused with permission.

ing them during diastole. There are usually two, sometimes even more, papillary muscles, anterolateral and posteromedial. Each papillary muscle consists of several heads or multiple thinner muscles (Carpentier, 2010, p. 33-36). Furthermore, each papillary muscle is connected to several chordae leading to both, the anterior and posterior leaflets. The size of the muscles ranges from 20 - 50 mm with an approximate distance to the mitral valve orifice of 25 mm (Carpentier, 2010, p. 33-36).

Function

The heart functions as a vital pump, propelling oxygen-rich blood through the circulatory system to nourish the body's tissues and organs while transporting oxygen-poor blood to be oxygenated inside the lungs (Brandes et al., 2019, p. 166-168). Healthy individuals have a resting heart rate of 60 - 100 bpm and systolic blood pressure of approximately 120 mmHg

(Brandes et al., 2019, p. 205,216). With a stroke volume of 70 ml a cardiac output of approximately 5 l/min is created (Brandes et al., 2019, p. 166-167). The heart cycle is divided into two phases called systole and diastole, which describe the contraction and relaxation of the heart, respectively (Brandes et al., 2019, p. 166-168). These phases are visible in Fig. 1.3 for the left part of the heart. During diastole, Fig. 1.4, the aortic valve is closed to prevent backflow from the aorta, where the aortic pressure exceeds the ventricular pressure at this point. The left ventricle and left atrium are relaxed and the mitral valve is open, which allows the blood to flow from the lung through the left atrium into the left ventricle (Brandes et al., 2019, p. 166-168).

At the end of the diastole, the left atrium contracts, atrial systole, which increases the atrial and ventricular pressure slightly and finalizes the filling of the left ventricle. Afterwards, the left ventricle contracts, increasing the ventricular pressure, which quickly exceeds the atrial pressure resulting in the closure of the mitral valve (Brandes et al., 2019, p. 166-168). This is the starting point of the systole. The pressure further increases during the isovolumetric contraction until the ventricular pressure exceeds the aortic pressure, which leads to the opening of the aortic valve and consequently to the ejection of blood into the aorta (Brandes et al., 2019, p. 166-168). At this stage, the closed mitral valve prevents the blood from flowing back into the left atrium. The ejection continues until the ventricular pressure drops below the aortic pressure, which results in the closing of the aortic valve, which marks the end of the systole. The left ventricle first relaxes isovolumetric until the ventricular pressure drops below the atrial pressure which leads to the opening of the mitral valve and the heart cycle starts again from the beginning (Brandes et al., 2019, p. 166-168).

A closer look at the mitral valve shows that the relaxation of the left ventricle during diastole leads to dilation of the left ventricle. This applies force on the chordae tendineae and consequently onto the leaflets, which in combination with the blood flow from the left atrium, opens up the mitral valve (Carpentier, 2010, p. 36-39). On the other hand, during systole, the contraction of the left ventricle leads to a contraction of the mitral annulus, which reduces the orifice by 26 ± 3 %, this increases the area where both leaflets come together, the so-called coaptation zone (Carpentier, 2010, p. 28). Due to ventricular contraction, the ventricular pressure exceeds the atrial pressure. Additionally, the papillary muscles contract and apply force through the chordae tendineae onto the leaflets and keep them in position. This prevents the leaflets from prolapsing and consequently opening up into the left atrium(Carpentier, 2010, p. 36-39). This shows, that all parts of the mitral valve play a crucial role in its function, which is still not fully understood.

Mitral valve insufficiency

The mitral valve insufficiency, also called mitral regurgitation, is the second most common valvular heart disease (Nkomo et al., 2006; Nickenig et al., 2013). It is defined as a leakage of the mitral valve which leads to a backflow, called regurgitation, of blood into the left atrium

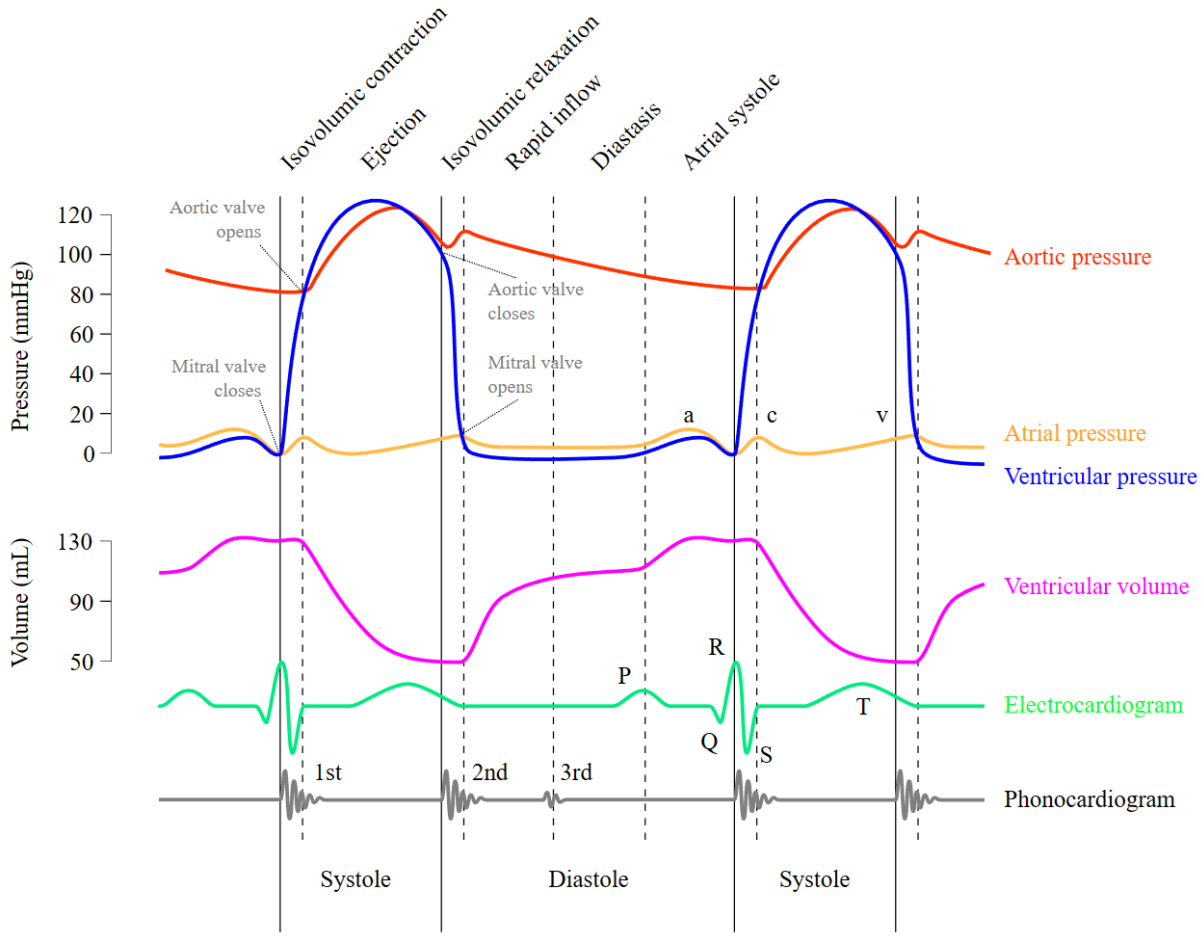

Figure 1.3: Wiggers diagram showing pressure, volume, electrocardiogram and phonocardiogram over one cardiac cycle. This figure was originally published in adh30 (2016), adapted and reused under the CC BY-SA 4.0 - License. [Accessed: 17.01.2024]

and consequently into the lungs during systole. The symptoms of mitral regurgitation are heart failure symptoms such as dyspnea on exertion, fatigue, edema, and dizziness. A clinical examination might show characteristic heart murmurs and heart sounds as well as the consequences of heart failure (pleural effusion, pulmonary congestion, edema) (Enriquez-Sarano et al., 2009; Nickenig et al., 2013).

The classification of mitral regurgitation refers either to the time course (acute, chronic), the origin (primary, secondary), the morphology (normal, abnormal leaflet motion), or the severity (mild, moderate, severe).

The origin of mitral regurgitation is differentiated between primary and secondary as shown in Figure 1.5. Primary mitral regurgitation is caused by defects of the valvular apparatus itself, such as tears in the leaflets, chordae rupture, or the rupture of papillary muscles. Secondary mitral regurgitation is a consequence of ventricular or atrial remodeling, such as atrial or ventricular enlargement, which might lead to a repositioning of the papillary muscles or annulus dilatation (El Sabbagh et al., 2018).

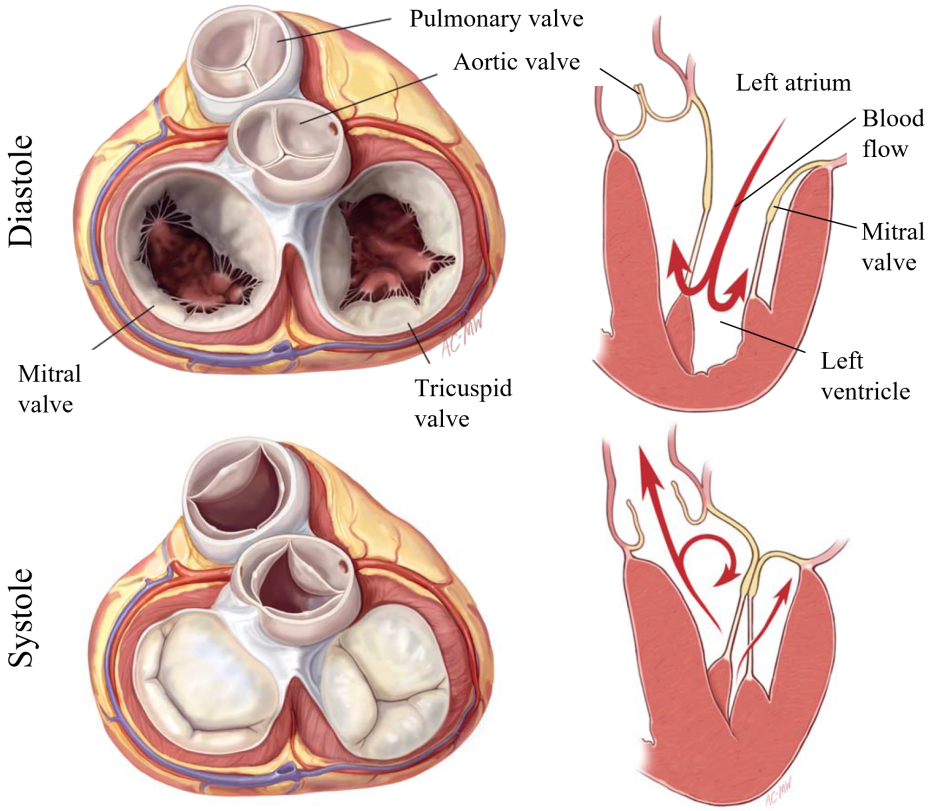

Figure 1.4: The heart during diastole (top) and systole (bottom) in atrial view (left) and cross-section-view of the left ventricle (right). This figure was originally published in Carpentier (2010), adapted and reused with permission.

Furthermore, mitral regurgitation is morphologically classified by Carpentier (Figure 1.5). Type I mitral regurgitation is defined by normal leaflet motion and occurs due to leaflet perforation or annulus dilatation. Type II mitral regurgitation shows excessive leaflet motion, due to for example chordae rupture, chordae elongation, or papillary muscle rupture. In contrast, Type III mitral regurgitation shows restricted leaflet motion. Type IIIa describes the restricted leaflet motion in systole and diastole due to e.g. chordae thickening or fusion, while Type IIIb shows restricted leaflet motion solely in diastole due to e.g. asymmetrical tethering in myocardial infarction (Carpentier, 2010; El Sabbagh et al., 2018; Del Forno et al., 2020).

Two grading systems coexist to classify the severity of mitral regurgitation. One differentiates between mild, moderate, and severe, while the other, a number-based grading system, differentiates between Grades 0 - 4. Grade 0 corresponds with non-pathological mitral valve and Grade 4 defines a severe mitral regurgitation. The severity is defined by qualitative, semi-quantitative, and quantitative metrics. Those metrics are acquired via TEE and will be covered in subsection 1.3.3 (Zoghbi et al., 2017; Dujardin et al., 1997). Mitral regurgitation is usually treated either with medication, MIMVS, TEER, or mitral valve replacement.

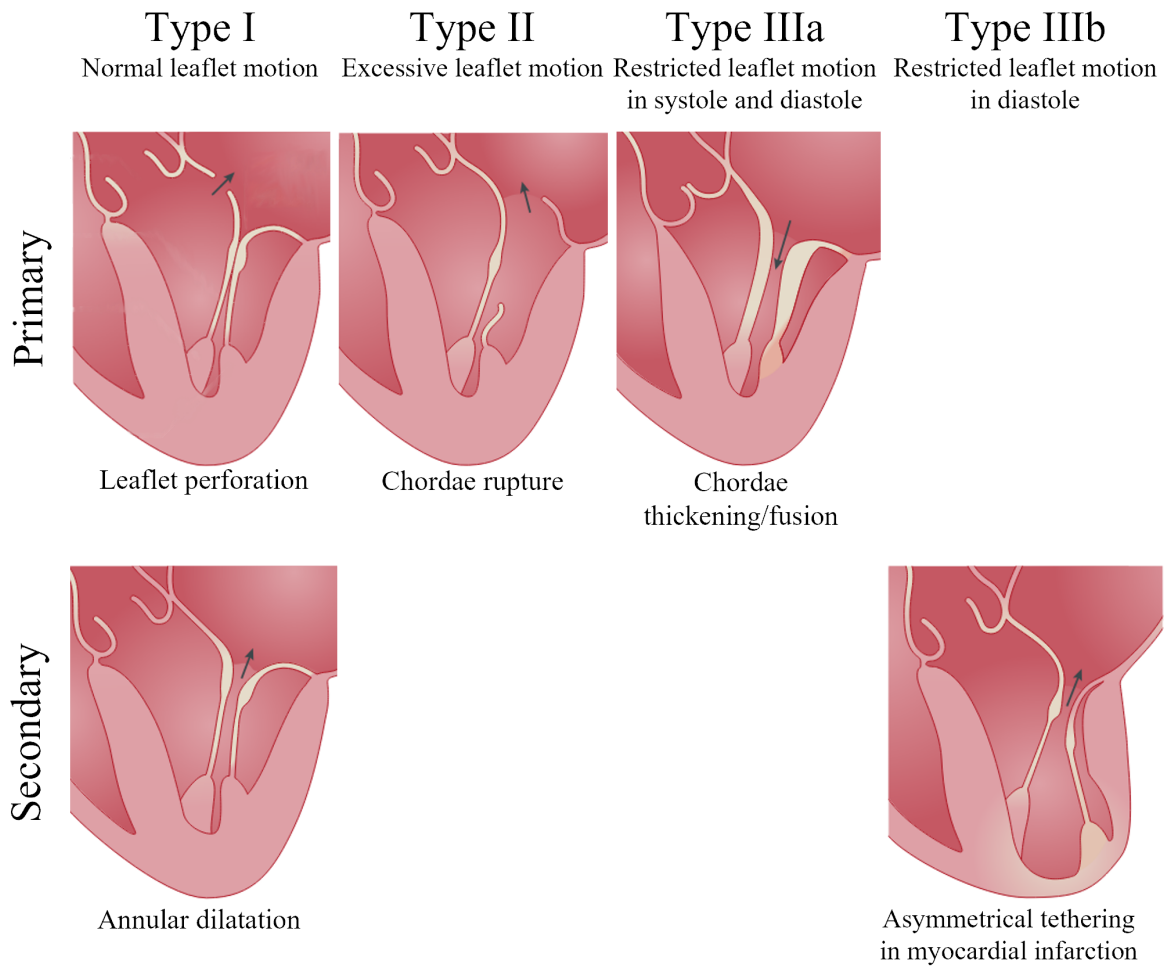

Figure 1.5: Functional and causal classification of mitral regurgitation with exemplary pathologies. This figure was originally published in Del Forno et al. (2020), adapted and reused with permission.

Minimally invasive mitral valve surgery

Mitral valve surgery is a procedure performed to repair or replace the mitral valve. During mitral valve surgery, the patient is put under general anesthesia. The chest is opened either via median sternotomy or right lateral minithoracotomy. The heart is temporally arrested via cardioplegia. The left atrium is opened to gain atrial access to the mitral valve. The mitral valve gets either replaced or repaired. After repair or replacement the left atrium is closed, the heart restarted, and the chest is closed (Carpentier, 2010).

The surgical approach to mitral valve repair has shifted from open surgery (median sternotomy) to minimally invasive surgery (right lateral minithoracotomy). This is due to similar low operative mortality and equally durable results, but reduced sternal complications, transfusion, post-operative pain, and time to return to normal activity, and improved cosmetics (Lange et al., 2017; Goldstone et al., 2013; Falk et al., 2011).

The right lateral minithoracotomy as visible in Figure 1.6 is done by a 50 mm incision in the fourth intercostal space (Javadikasgari et al., 2018; Carpentier, 2010, p. 17-18). Before arresting the heart, a cardiopulmonary bypass is installed between the aorta ascendens and both venae cavae. After cross-clamping the aorta the heart is arrested with cold blood cardioplegia (Carpentier, 2010, p. 17-18). After opening the left atrium by an incision, the mitral valve is evaluated by the surgeon. To repair the mitral valve the surgeon has several techniques to choose and combine. The most important techniques are described in the following.

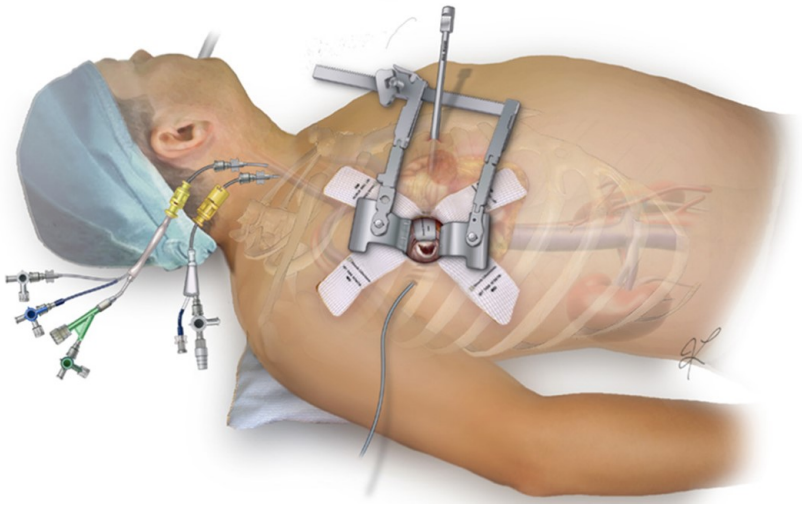

Figure 1.6: Right lateral minithoracotomy providing an atrial view of the mitral valve. This figure was originally published in Javadikasgari et al. (2018), reused with permission.

Mitral valve annuloplasty is a technique where an annuloplasty ring is implanted to remodel and stabilize the annulus as well as to create a large coaptation zone by reducing the mitral annulus diameter if needed. In the first step a sizer as visible in Figure 1.7a is placed on top of the anterior leaflet and a hook is used to stretch the leaflet. Different sizers are used after another to determine the right size for the annuloplasty ring concerning the therapy goal to enlarge, shrink, reshape, or stabilize the mitral annulus. Sutures are placed along the annulus and annuloplasty ring (Figure 1.7a). Finally the sutures are fastened tight (Figure 1.7c) (Carpentier, 2010, p. 63-81).

Mitral valve repair by manipulation of the leaflets is called leafletplasty. Common techniques are the triangular (Figure 1.8) or quadrangular leaflet resection. Triangular leaflet resection is used to treat limited prolapse at the posterior or anterior leaflet. Quadrangular leaflet resection is mainly performed to treat extensive posterior prolapse. Both techniques include the partial resection of the leaflet ((Figure 1.8) a) and the closure of the resected area (Figure 1.8b) (Carpentier, 2010, p. 96-125).

Mitral valve chordaeplasty describes the modification of the chordae tendineae to restore normal leaflet motion. These modifications involve either the shorting, transposition, or implantation of artificial chordae tendineae (Carpentier, 2010, p. 98-110).. Artificial chordae

tendineae, so-called neo-chordae, become necessary when native chordae, e.g. due to chordae rupture (Figure 1.9a), are not adequately available.

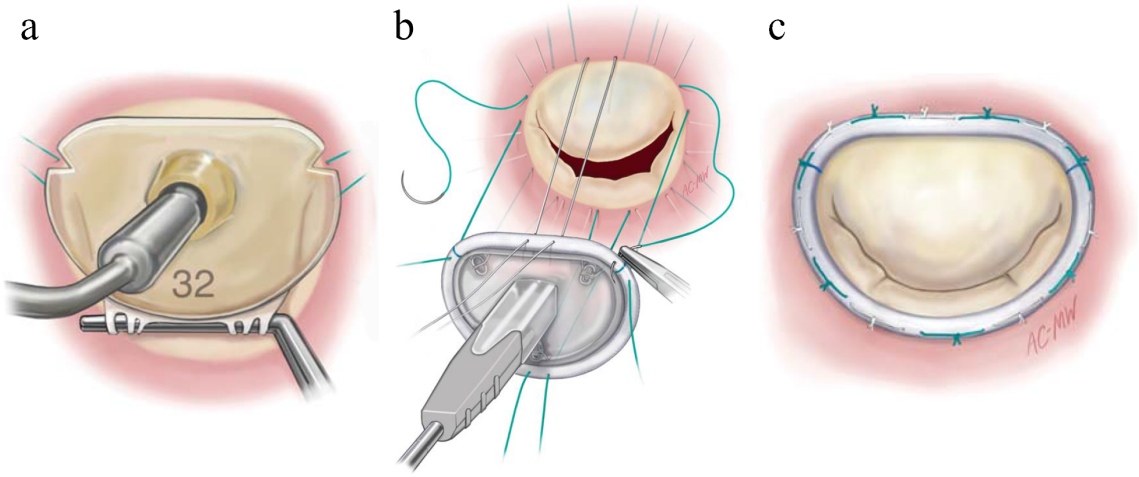

Figure 1.7: Annuloplasty: a) A sizer is used to determine the right size of the annuloplasty ring. b) Sutures are placed along the mitral annulus and the annuloplasty ring. c) The sutures are fastened tight. This figure was originally published in Carpentier (2010), adapted and reused with permission.

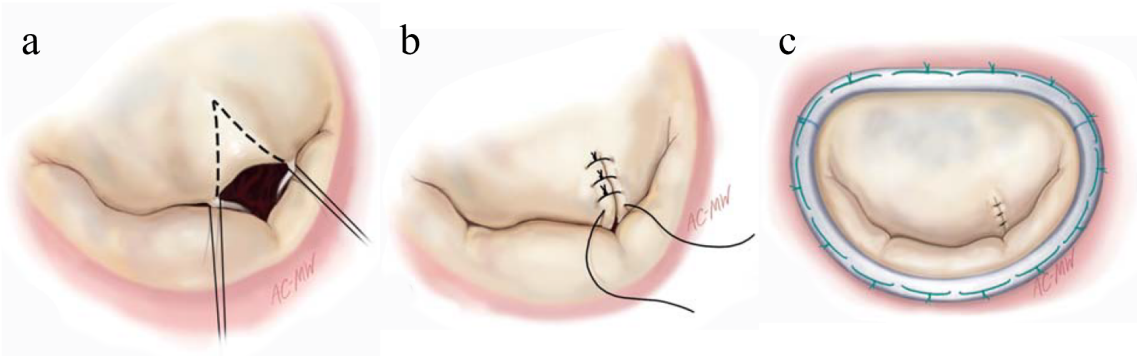

Figure 1.8: Triangular leaflet resection: a) Mitral valve with a prolapse at A2/A3 segment of the anterior leaflet with markings for the triangular leaflet resection. b) After resection the leaflet is repaired. c) The leaflet resection is combined with an annuloplasty. This figure was originally published in Carpentier (2010), adapted and reused with permission.

The neo-chordae, usually made out of polytetrafluoroethylene, commonly known as PTFE, are positioned analog to native chordae between the papillary muscles and the leaflets (Figure 1.9b). The major difficulty remains the adjustment of the neo-chordae length which plays a crucial role to restore the normal leaflet motion. The length has to be adjusted according to the healthy neighboring native chordae tendineae (Figure 1.9c) (Carpentier, 2010, p. 98-110).

Transcatheter edge-to-edge repair

TEER is a percutaneous technique to repair mitral valves. This technique, as seen in Figure 1.10, connects the edges of the anterior and posterior leaflet by placing one or more clips

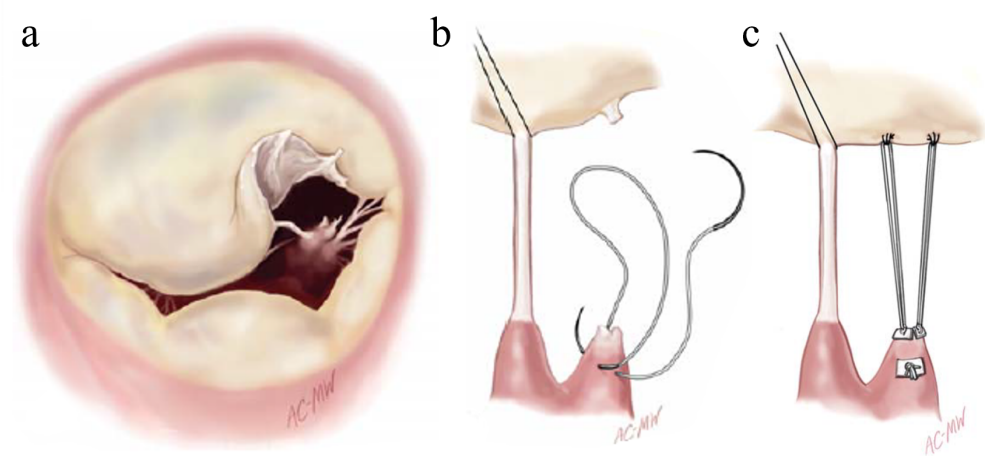

Figure 1.9: Neo-chordae insertion: a) The anterior leaflet prolapses into the left atrium due to chordae tendineae rupture. b) Artificial chordae tendineae (neo-chordae) are sewed into a head of a papillary muscle, and c) neo-chordae connect the leaflet to the papillary muscle with an adequate length. This figure was originally published in Carpentier (2010), adapted and reused with permission.

at the leaflet tips. The goal of this therapy is neither to restore normal leaflet function, nor to remodel the annulus, but to increase the coaptation zone and reduce mitral regurgitation. In contrast to MIMVS there is neither the need to open the chest, nor for a cardiopulmonary bypass, nor to induce cardioplegia. However, not all mitral valve pathologies can be repaired by TEER. TEER is mostly performed on patients who are unsuitable for open heart surgery, mainly due to age, comorbidity, or impaired left ventricle function (Mirabel et al., 2007).

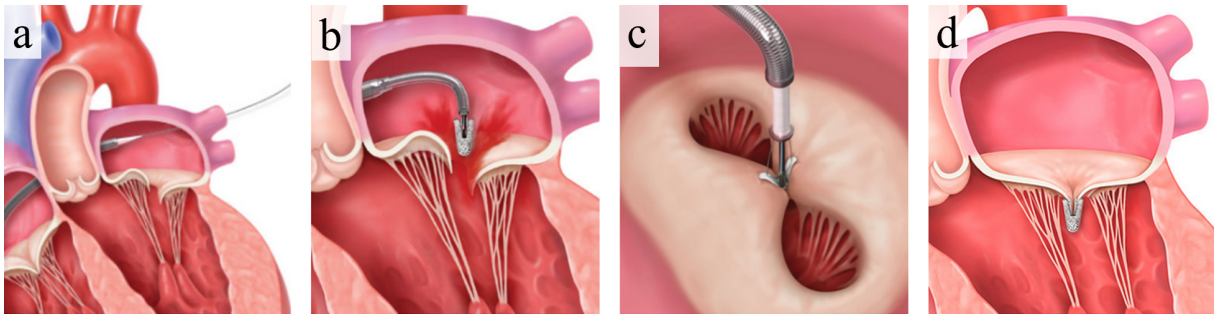

Figure 1.10: Transcatheter edge-to-edge repair: a) the device is navigated from the right common femoral vein via the septum into the left atrium. b) The clip is positioned perpendicular to the annulus plane of the mitral valve. c) The leaflet edges are grasped by the clip. d) The clip connects the leaflet edges and the delivery device is retracted. MitraClip is a trademark of Abbott or its related companies. Reproduced with permission of Abbott, © 2023. All rights reserved.

TEER as described by Rodriguez et al. (2021) is performed in a hybrid operation room. The patient is treated with general anesthesia and put into supine position. A TEE is performed to assess among others the severity of mitral regurgitation. The hemodynamic data is recorded to be compared after TEER. Via venous access at the right common femoral vein and transseptal access, the TEER device is advanced into the left atrium (Figure 1.10a). The guidance is done by using fluoroscopy and TEE. The TEER clip is positioned above the mitral valve,

perpendicular to the annulus plane (Figure 1.10b) in the center of the regurgitation jet visible in the TEE color-doppler. While the clip is approached into the left ventricle, it is maintained that there is neither an anterior/posterior nor a medial/lateral drift. Risks at this stage are mal-location and chordae entanglement. The movement and rotation of the clip before and after crossing the mitral valve are observed via TEE and fluoroscopy. Once the clip crossed the mitral valve and sits in its final position the clip opens to 120°. Once the leaflet has a good position on the clip, the clip is closed to 60°. The position is observed via TEE. Both leaflets can be grasped individually one after another (Figure 1.10c). Once the position is reconfirmed via imaging the clip is fully closed. A complete TEE is done to assess among others the residual mitral regurgitation. If the physicians are satisfied with the outcome the delivery system is retracted (Figure 1.10d), otherwise the clip either has to be re-positioned or additional clips have to be placed. In case of additional clips, the guide sheath of the TEER device remains in the human body enabling access to the left atrium.

1.3.2 Aorta

This section gives a short overview of the aorta's anatomy, function, the pathology of aortic dissection, and TEVAR.

Anatomy and function

The aorta is the biggest arteria of the human body and supplies the body with oxygenated blood from the heart. It is distinguished as shown in Figure 1.11 between the aorta ascendens, aortic arch, and aorta descendens (Zilles and Tillmann, 2010, p. 342-345).. The latter is separated into the thoracic and abdominal aorta, which branches into the arteria iliaca communis dexter and sinistra. Multiple branches along the aorta lead to several different areas, such as the carotid arteries, which lead to the head, or the arteria renalis which supplies the kidneys and branch from the abdominal aorta (Zilles and Tillmann, 2010).

The aorta has a length of 300 - 400 mm and a diameter of 21 - 30 mm and 15 - 30 mm in the thoracic and abdominal parts respectively (Zilles and Tillmann, 2010, p. 343). The walls of blood vessels such as the aorta consist of three layers: the tunica intima, tunica media, and tunica externa, also called adventitia, as visible in Figure 1.12 (Zilles and Tillmann, 2010, p. 338-339).

The tunica intima contains one layer of endothelial cells, which have several functions, such as being the barrier for diffusion and transport between blood and organs, and the control of coagulation and adhesion of thrombocytes and leukocytes (Zilles and Tillmann, 2010, p. 338-339). The tunica media consist of smooth muscles cells which resist a widening of the vessel. Furthermore, the muscle cells can regulate blood pressure. This is called the windkessel effect. The windkessel effect of the aorta is a physiological phenomenon driven by the artery's elasticity. During systole, the aorta expands to store pressurized blood ejected

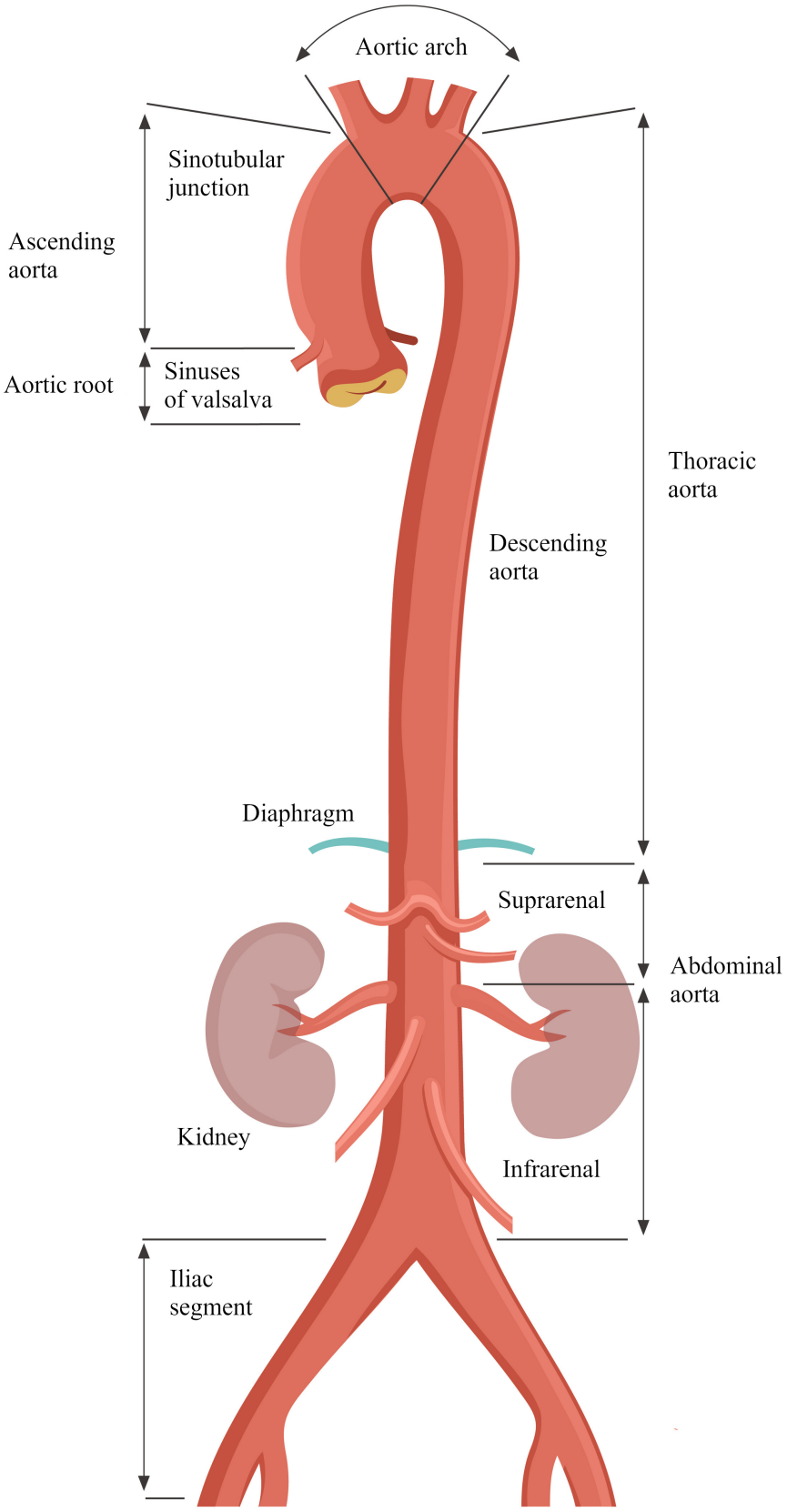

Figure 1.11: The structure of the aorta and main branches. Adapted and reused ©nmfotograd / Adobe Stock #487704211.

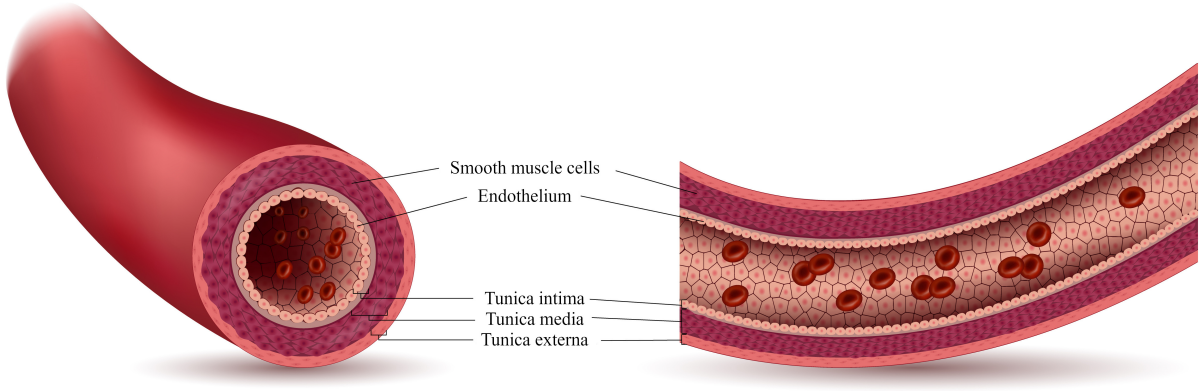

Figure 1.12: The layers of a blood vessel such as the aorta. Adapted and reused ©reineg / Adobe Stock #81283294.

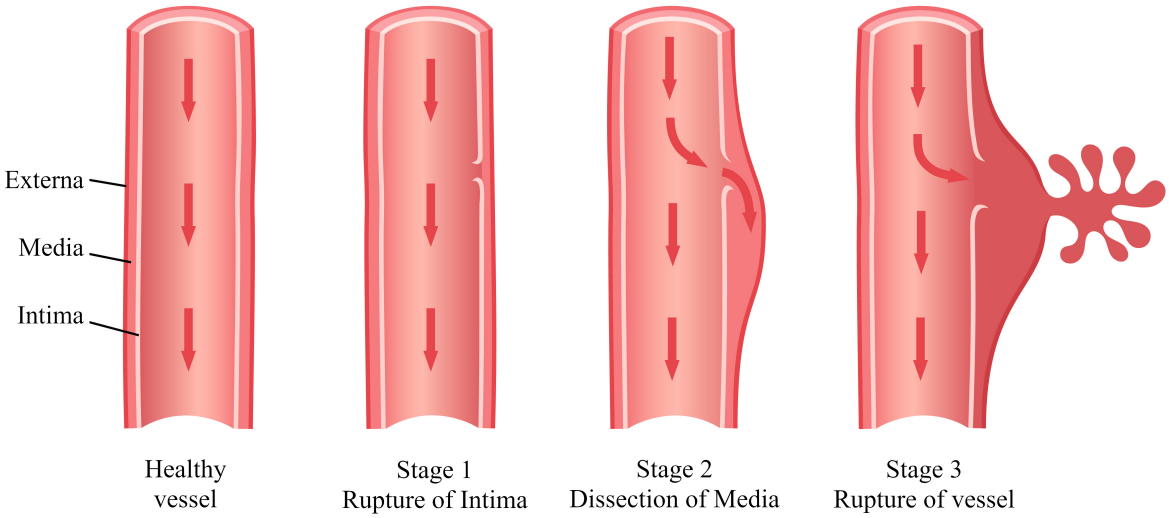

Figure 1.13: Evolution of an aortic dissection: A healthy aorta with the tunica intima intact. In stage 1 the tunica intima ruptures. In Stage 2 blood flows through the rupture resulting in a dissection of the tunica media. At stage 3 the vessel eventually ruptures. Adapted and reused ©Olga/Adobe Stock #306882863.

from the heart, and during diastole, it recoils, releasing stored energy to maintain continuous and steady blood flow. This mechanism helps to smooth out pulsatile blood flow, to reduce the heart's workload, and to stabilize blood pressure in the systemic circulation (Zilles and Tillmann, 2010, p. 338-339). The tunica externa, also called adventitia, consists of connective tissue and integrates the vessel into the surrounding environment (Zilles and Tillmann, 2010, p. 338-339).

Aortic dissection

The aortic dissection is defined by a tear, called entry, in the tunica intima, leading to a separation of the tunica intima and tunica media. Antegrade and retrograde flow through the lesion increases the separation and forms a true and false lumen (Figure 1.13) (Erbel et al., 2014; Corvera, 2016). A Stanford Type A aortic dissection (TAAD) is defined by an entry prox-

imal, and a TBAD by an entry distal to the arteria subclavia sinistra (Figure 1.14).

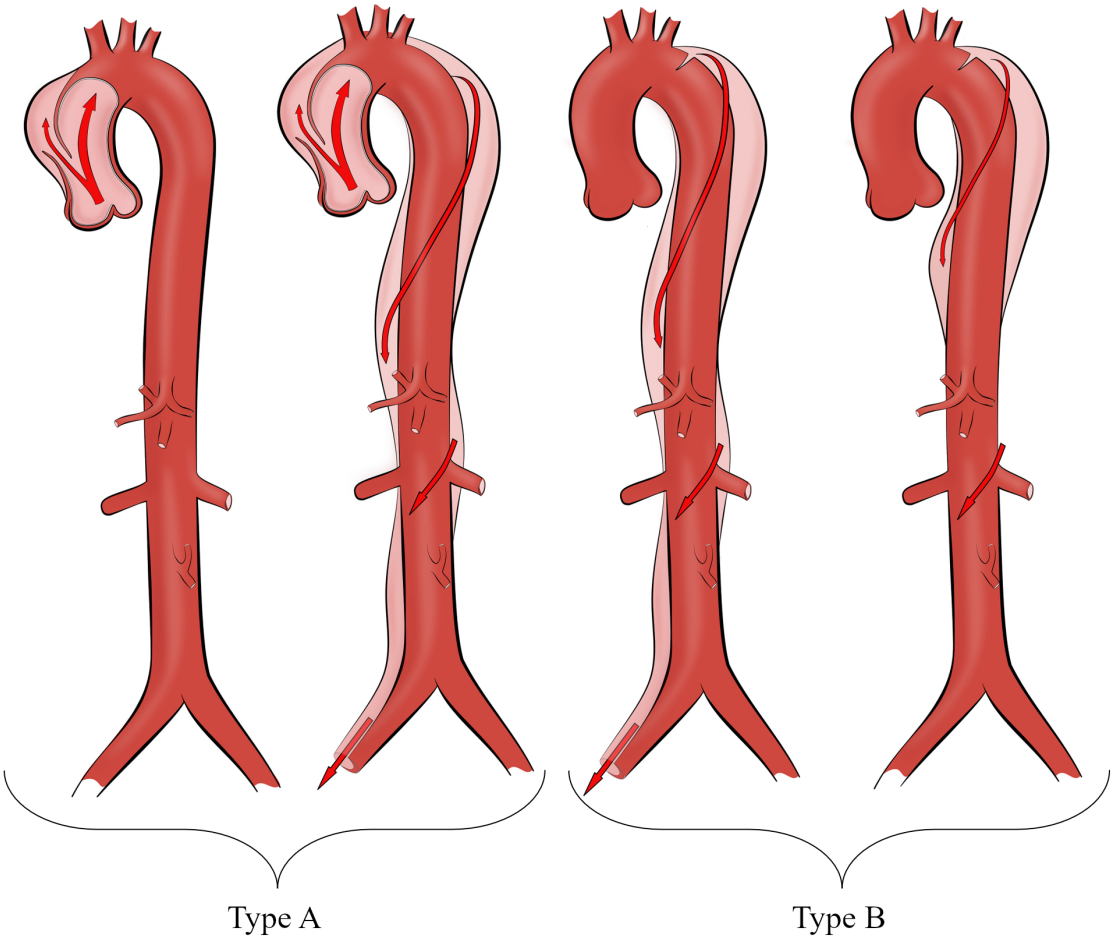

Figure 1.14: Stanford classification of aortic dissections. The type A aortic dissection is defined by an entry proximal to the arteria subclavia sinistra. The type B aortic dissection is defined by an entry distal to the arteria subclavia sinistra. Adapted and reused ©pirke/Adobe Stock #348118071.

TAAD occurs more than twice as commonly as TBAD (Corvera, 2016). TBAD has an incidence of 2.6 - 3.5 cases per 100,000 people/year (Akin et al., 2012). It is distinguished between acute (<14 days), sub-acute (15 - 90 days), and chronic aortic dissection (>90 days) (Erbel et al., 2014).

The risk factors of aortic dissection are hypertension, atherosclerosis, aneurysm, prior cardiac surgery, and connective tissue disorders such as Marfan syndrome (Corvera, 2016). The symptoms of aortic dissection cover severe chest or back pain and hypertension and less commonly congestive heart failure, syncope, cerebrovascular accident, shock, paraplegia, and lower extremity ischemia (Spittell et al., 1993; Hagan et al., 2000).

For this work, the focus is on the TBAD. TBAD is treated conservatively in uncomplicated cases, while in complicated cases, 30 - 42% of TBAD (Tsai et al., 2006; Akin et al., 2011), are treated, when possible, with TEVAR (Akin et al., 2011). Factors of complicated TBAD under

the guidelines of the European Society of Cardiology are early aortic expansion, malperfusion, signs of rupture, uncontrolled hypertension despite full medication, and persistent or recurrent pain (Erbel et al., 2014).

Thoracic endovascular aortic repair

As mentioned in Section 1.3.2 complicated TBAD is treated with TEVAR. The TEVAR procedure (Figure 1.15) has the goal of reconstructing the dissected aorta, sealing the proximal entry, depressurizing the false lumen, and consequently initiating the thrombosis of the latter (Akin et al., 2011). In some cases of malperfusion, it is possible to obliterate the false lumen, by expanding the true lumen due to TEVAR (Szeto et al., 2008).

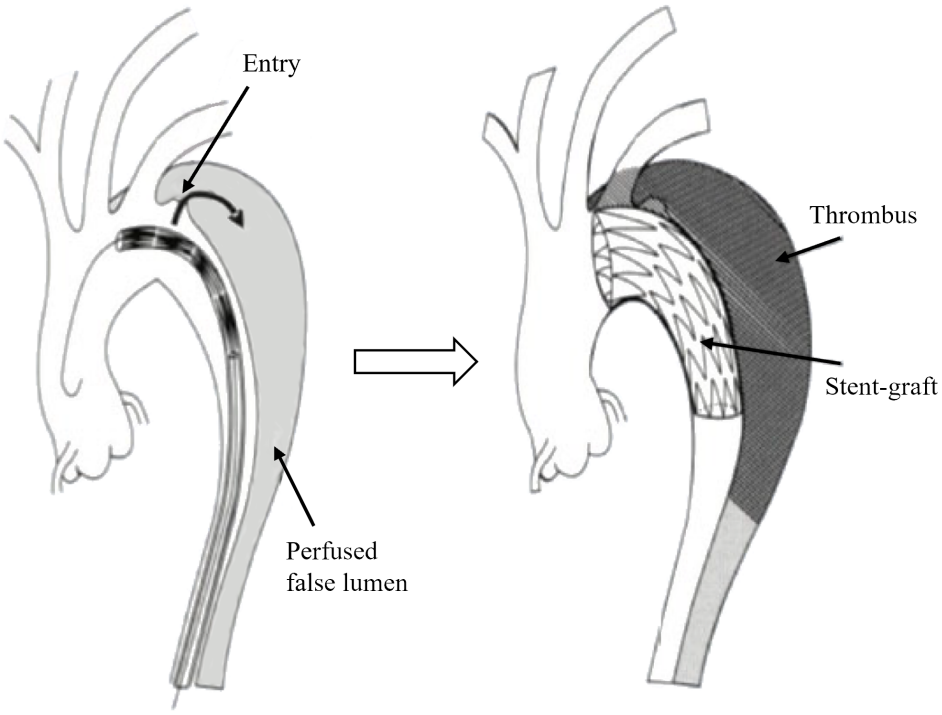

Figure 1.15: Thoracic endovascular aortic repair with the undeployed stent-graft over the stiff wire (left) and the deployed stent-graft sealing the entry and initiating a thrombosis inside the false lumen (right). This figure was originally published in Akin et al. (2011), reused with permission.

.

The TEVAR procedure comprises the following steps (Akin et al., 2011):

1. For each patient the individual stent-graft size has to be determined. Commercially available stent-grafts for TBAD cover outer diameters between 16 - 42 mm. The stent-graft has to cover the primary entry to guide the antegrade flow through the true lumen. Furthermore, proximal and distal landing zones of > 15 - 20 mm each, have to be considered (Upchurch et al., 2021). The use of multiple overlapping stent-grafts is possible. The sizing is done based on CTA or intravascular ultrasound.

2. A hybrid operating room or catheterization laboratory is preferred for the TEVAR procedure.

3. A 20 - 24 Fr introducer sheath is placed in the femoral artery, which is the most common access for this procedure, using the Seldinger technique.

4. A pigtail catheter with a soft wire is navigated under fluoroscopic (DSA) guidance through the true lumen into the aortic arch.

5. The soft wire inside the pigtail catheter is retracted and replaced by a stiff wire. The pigtail catheter gets retracted as well.

6. The stent-graft is carefully advanced into the true lumen and guided by the stiff wire towards its final position.

7. The stent-graft is launched. During launching the systolic blood pressure might be lowered. Several techniques exist to lower pressure such as rapid right ventricular pacing.

8. In case of an incomplete proximal sealing an inflated latex balloon might improve the position of stent-graft struts. This may not be an option for acute TBADs due to the risk of retrograde TAAD.

9. To examine the outcome of the TEVAR procedure via fluoroscopy a second pig-tail catheter can be advanced through the introducer sheath mentioned in step 3.

TEVAR has justified its usage by reducing morbidity and mortality in comparison to open surgical repair, however, several risks such as stroke, spinal cord ischemia, device failure, unintentional great vessel coverage, access site complications, and renal injury, exist (Chen et al., 2020).

1.3.3 Medical imaging and measurements

For the diagnoses and treatment of mitral regurgitation and TBAD different medical imaging technologies are used and therefore need to be taken into account for the design process of the hemodynamic simulators. These technologies comprise ultrasound, especially TEE, used especially for the diagnoses of mitral regurgitation and during mitral valve repair, CT to diagnose TBAD and for post-interventional checkup, and angiography, in specific DSA, during TEVAR. Each technology has its advantages and disadvantages as visible in Table 1.1. While ultrasound does not expose the patient to ionizing radiation CT and angiography do. CT on the other hand does not provide real-time information about the patient, while angiography and ultrasound do. Furthermore, they have different imaging technologies: In angiography, the image is a projection, of the scanned part, while ultrasound and CT provide a cross-sectional view (Figure 1.16). Additionally, the use of ultrasound is less cost-intensive than angiography, and CT is the most expensive technology of the mentioned (Kramme, 2017, p. 364).

Table 1.1: Comparison of medical imaging technologies based on (Kramme, 2017, p. 364). CTA = computed tomography angiography, DSA = digital subtraction angiography, TEE = transesophageal echocardiography.

	TEE	CTA	DSA
ionizing radiation	no	yes	yes
realtime	yes	no	yes
imaging technique	cross-sectional	cross-sectional	projection
total cost	low	very high	high

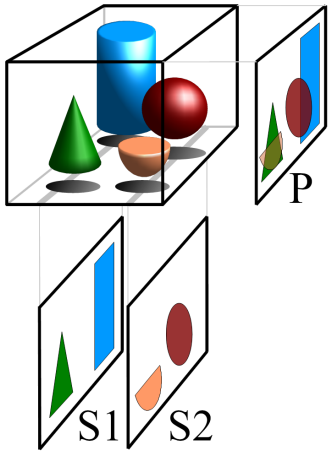

Figure 1.16: Basic principle of projected (P) and cross-sectional imaging (S1 and S2). This figure was originally published in Dtrx (2009), adapted and reused under the CC BY-SA 3.0 - License. [Accessed: 17.01.2024]

Transesophageal echocardiography

TEE is a non-invasive medical imaging technology used to assess the structure and function of the heart by using ultrasound with an inserted transducer into the esophagus as seen in Figure 1.17a. Depending on the position and orientation of the transducer it can show different views of the heart such as the four-chamber view (Figure 1.17b). It utilizes ultrasound waves to create real-time images of the heart and its surrounding blood vessels. By providing detailed visualizations, echocardiography helps doctors diagnose and monitor various cardiovascular conditions.

The transducer emits high-frequency sound waves which are reflected by the heart's structures or erythrocytes in the blood and return as echoes. These echoes are then converted into images that display the heart's chambers, valves, blood flow patterns, and overall cardiac performance.

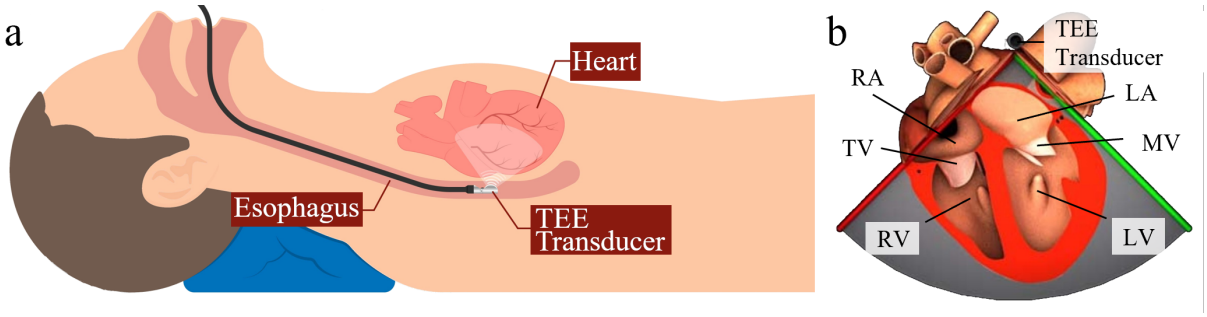

Figure 1.17: Transesophageal echocardiography: a) Ultrasound probe is inserted into the esophagus scanning the heart. Adapted and reused ©rumruay/Adobe Stock #387784723. b) The cross-sectional four-chamber view by TEE. This figure was originally published in http://pie.med.utoronto.ca/tee, TGHDoA (2014), adapted and reused with permission. [Accessed: 17.01.2024] . LA = left atrium, LV = left ventricle, MV = mitral valve, RA = right atrium, RV = right ventricle, TEE = transesophageal echocardiography, TV = tricuspid valve.

Echocardiography offers valuable information about the heart's size, shape, and movement. It can detect abnormalities such as heart valve disorders, congenital heart defects, cardiac masses, and structural abnormalities. Additionally, it provides essential data on heart function, including the measurement of the ejection fraction, regurgitation volume, or pressure gradients across heart valves, and the assessment of blood flow through the heart's chambers and blood vessels.

Echocardiography is widely used in cardiology practice due to its safety, non-invasiveness, and versatility. It helps guide treatment decisions e.g. for mitral regurgitation, guidance during percutaneous interventions such as TEER, monitor the progression of heart conditions, and assess the effectiveness of therapies. Overall, echocardiography plays a crucial role in diagnosing and managing cardiovascular diseases, contributing to improved patient outcomes and quality of care.

Ultrasound can be used in different modes to acquire versatile information. The most important ones for this work are the 2D-B-mode, color-doppler, CW-Doppler, and 3D-mode and shown in Figure 1.18.

The 2D-B-mode (Figure 1.18a) is the most-important cross-sectional ultrasound mode. In this mode, pulsed ultrasound waves are emitted and received by the transducer. The amplitude of the ultrasound reflection is translated into the brightness of an image point, with dark areas weakly, and bright areas strongly reflecting the ultrasound waves. The 2D image is finally created by lining up B-mode lines of image points at a very high frequency. One problem of the technology is the trade-off between high resolution and penetration depth (Kramme, 2017, p. 370-375).

The color-Doppler mode (Figure 1.18b) uses the run-time information to determine the location of a sample volume. Instead of using the information to create an image, the ve-

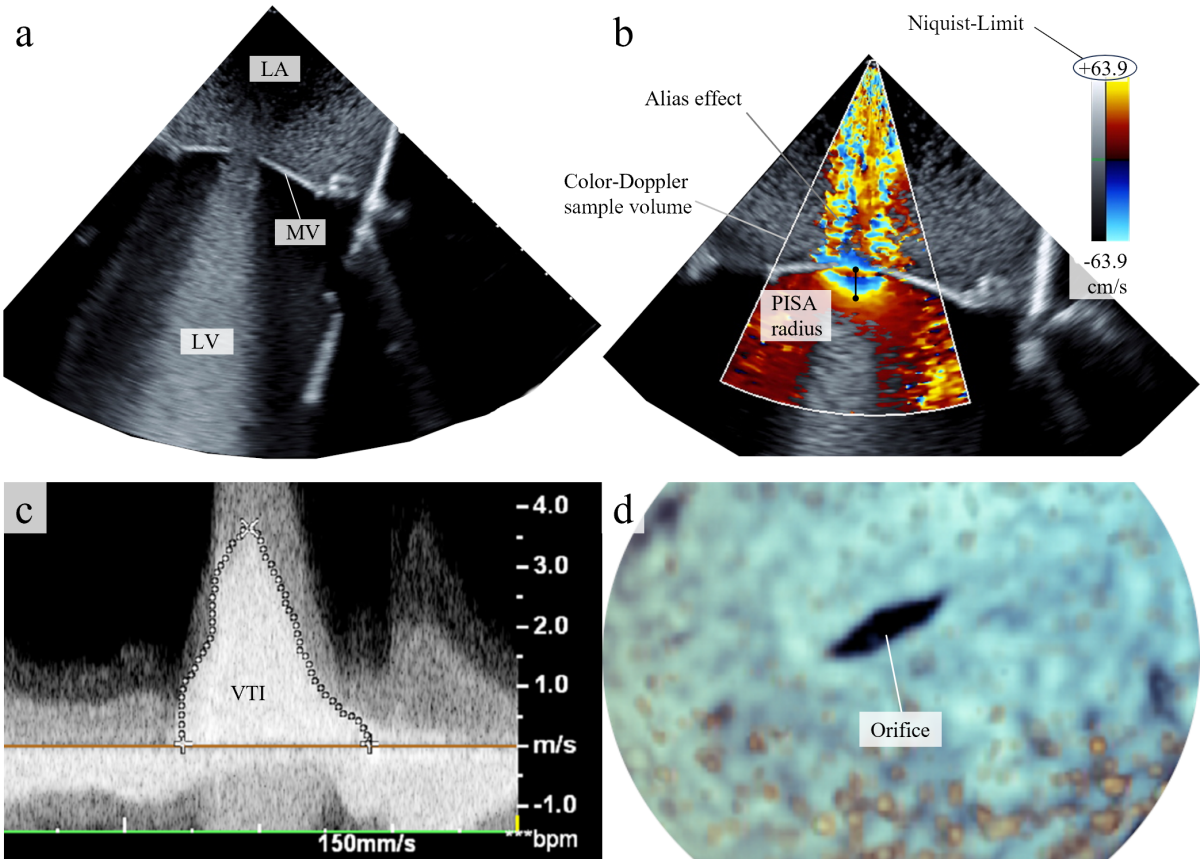

Figure 1.18: Ultrasound modalities used in this work for an artificial mitral valve in a simulator acquired via transesophageal echocardiography: a) 2D-B-mode of the left atrium (LA) and ventricle (LV) showing the orifice of the mitral valve (MV) during mid-systole. b) Color-doppler mode overlaying the 2D-B-mode during mid-systole showing a central jet into the left atrium and the proximal isovelocity surface area (PISA) in the left ventricle, both inside the chosen sample volume. The blue areas show the alias effect and the upper limit of the color bar shows the Nyquist-Limit. c) The continuous wave doppler for one beat of the jet beam axis, with the velocity time integral (VTI) of the systole marked by a physician (dotted line). Visible light grey areas are artifacts. d) 3D mode of the artificial mitral valve showing the slot-like shape of the orifice during mid-systole.

locimetry is measured using the Doppler principle. To create a color-doppler image hundreds of sample volumes are lined up and overlaid onto the B-mode picture. To differ from the grey scale B-mode image, the velocity information is color coded. Flow away from the ultrasound probe is colored blue, and flow towards the ultrasound probe is colored red. If the flow exceeds the sampling rate the alias effect occurs. In this case for example, in the middle of a red area blue sections occur. It is impossible that surrounded by flow towards the probe a small patch of flow is directed the opposite way. This makes it easy to identify the occurrence of the aliasing effect. The aliasing effect can be used to identify the location of maximum speed and to visualize for example the regurgitation jet. The speed of flow where the aliasing effect occurs is called the Nyquist limit or aliasing speed (Kramme, 2017, p. 370-375).

The CW-Doppler (Figure 1.18c), which stands for continuous wave Doppler, is the only non-pulsed ultrasound technique used to measure the velocity of blood flow. Ultrasound is permanently emitted by an emitter, and the reflection is continuously received by the receiver. This mode doesn't allow any depth information, since the run time of sound can not be measured, however, it does allow to accurately measure high velocities (Kramme, 2017, p. 370-375).

Due to the development of matrix-array transducer 3D-imaging is possible without manual or automatic movement of the transducer (Figure 1.18d). Multiple B-mode images with an angular offset are acquired and reconstructed in real-time to create for example the surface of the geometry. The 3D mode can be overlaid with e.g. the color-doppler mode (Kramme, 2017, p. 363 - 381).

Flow convergence method

One application for TEE is the diagnosis and classification of mitral regurgitation as defined by the European Association for Cardio-Thoracic Surgery and the European Society of Cardiology (Table 1.2).
Some qualitative criteria include the mitral valve morphology, size of the left atrium and left ventricle, color flow jet area, or flow convergence. The vena contracta width, pulmonary vein flow, or mitral inflow comprise semi-quantitative criteria. Furthermore, quantitative criteria are regurgitation volume, effective regurgitation orifice area (EROa), and regurgitation fraction. These are determined with the flow convergence method which includes the following steps (Zoghbi et al., 2017):

- Adjusting the aliasing speed (V_a), also known as Nyquist-Limit in color-doppler mode to typically 30 - 40 m/s
- Measuring the Proximal Isovelocity Surface Area (PISA) - radius (r_{PISA}) (Figure 1.18b).
- Calculating the regurgitation flow (RFlow)

$$RFlow = 2\pi r_{PISA}^2 \cdot V_a \tag{1.1}$$

- Measuring the velocity time integral (VTI) and the maximum Speed (V_{max}) in CW-Doppler mode (Figure 1.18c)
- Calculating the EROa

$$EROa = \frac{RFlow}{V_{max}} \tag{1.2}$$

- Calculating the regurgitation volume (RVol)

$$RVol = EROa \cdot VTI \tag{1.3}$$

Table 1.2: Guidelines of the European Association for Cardio-Thoracic Surgery and the European Society of Cardiology to grade the severity of chronic mitral regurgitation by echocardiography. EROa = effective regurgitatant orifice area, LA = left atrium, LV = left ventricle, MV = mitral valve, RF = regurgitation fraction, RVol = regurgitation volume, VCW = vena contracta width (Zoghbi et al., 2017; Vahanian et al., 2022).

	Mild	Moderate		Severe
	Grade 1	Grade 2	Grade 3	Grade 4
Qualitative				
MV morphology	None or mild leaflet abnormality	Moderate leaflet abnormality or moderate tenting		Severe valve lesions
LV and LA size	Usually normal	Normal or mild dilated		Dilated
Color flow jet area	Small, central, narrow, often brief	Variable		Large central jet (> 50 % of LA) or eccentric jet
Flow convergence	Not visible, transient or small	Intermediate in size and duration		Large throughout systole
Semiquantitative				
VCW [cm]	< 0.3	0.3 - 0.7		> 0.7
Pulmonary vein flow	Systolic dominance	Normal or systolic blunting		Minimal to no systolic flow/ systloic flow reversal
Mitral inflow	A-wave dominant	Variable		E-wave dominant (> 1.2 m/s)
Quantitative				
RVol [ml]	< 30	30 - 44	45 - 59	≥ 60
EROa [cm^2]	< 0.20	0.20 - 0.29	0.30 - 0.39	≥ 40
RF [%]	< 30	30 - 39	40 - 49	≥ 50

Computed tomography angiography

CT was the first method to allow for axial cross-section images of the human body without overlay (Kramme, 2017, p-317-336). In contrast to conventional radiography the X-ray tube travels at high speeds on a circular path around the patient's body as visible in Figure 1.19a. The X-ray tube emits radiation which travels through the patient's body and is continuously transmitted to the stationary detector array. On a computer, this information gets stored and an image is reconstructed. The reconstruction creates a cross-sectional axial image in contrast to projection images created by conventional radiography. By moving the patient through the CT scanner, the rotating X-ray tube describes a helical course around the patient's body as visible in Figure 1.19b. This method is also known as spiral CT and enables to create sub-millimeter axial slices of the full length of the patient. Special software allows

one to view the patient from any angle, perspective, and depth. (Gebhart and Schmidt, 2013, p. 826-832).

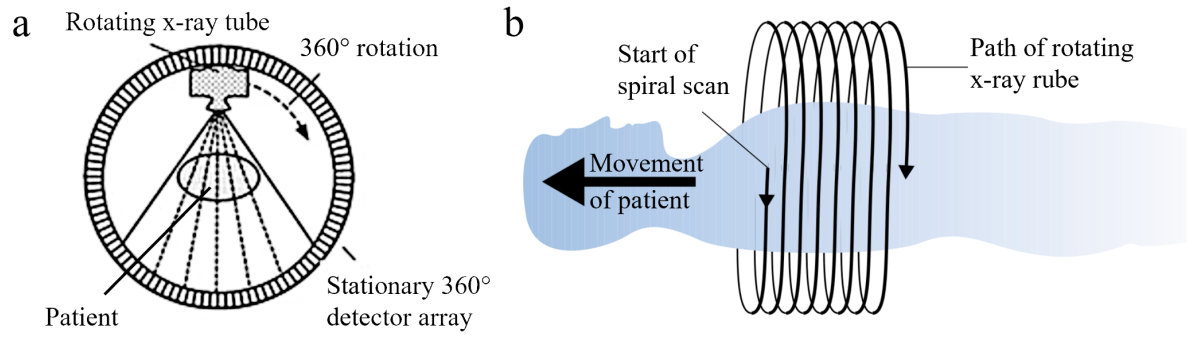

Figure 1.19: The basic principle of modern CT scanners. a) A rotating X-ray tube emits radiation which travels through the patient to a detector array. b) During the rotation, the patient is moved through the CT scanner. In relation to the patient, the X-ray tube moves along a helical path around the patient's body. CT = computed tomography. This figure was originally published in a)Flohr (2013), b)Dixon and Dendy (1998), adapted and reused with permission.

The fundamental challenge in CT is to reconstruct an object using its projections. Mathematically, CT involves an inverse problem, as there is no direct access to the spatial arrangement of the objects being depicted. Only the projections along the rotating detector coordinate are available. From this information, one must deduce the spatial distribution of the objects – essentially working backward. For further information it is referred to Kramme (2017) (p. 317-336). In CT, several kinds of artifacts can affect the image. These artefacts can be patient-based e.g. due to motion or jewellery, physics-based such as beam hardening, or hardware based e.g. ring artefacts. In this work, CT will be used for the assessment of TBAD and TEVAR. The stent-graft used for TEVAR consists of metal which creates artifacts. The metal absorbs the X-ray beams stronger than the surrounding tissue. These metal artifacts might lead to dark stripes between metal parts and star-shaped stripes originating from the metal overlaying the surrounding tissue. For further information an artefacts it is refereed to Kramme (2017) (p. 317-336).

The radiodensity of tissues is displayed in reconstructed images as grey scale values. A dimensionless scale that relates CT values to the radiodensity of water (μ_{water} = 0 HU) was introduced (Equation 1.4). The unit for the radiodensity is called Hounsfield-Unit (HU). Technically, a value range of 4000 HUs could be adequately displayed using 12-bit grey scale values. However, given that most tissues, apart from bones, have CT values that differ only by a small fraction from that of water, distinguishing these differences with the human eye would not be feasible. A technique called windowing, also referred to as grey-level mapping, contrast stretching, histogram modification, or contrast enhancement, was introduced. To enhance the visibility of specific structures a specific range of HUs is mapped on a 256 values grey scale. Figure 1.20a shows the mapping of the so called bone, lung, and soft tissue

windows. Figure 1.20b shows a soft tissue window with a window width of 400 HU and a window level (center) of +60 HU. The CT values below and above the window are displayed in black and white, respectively. Furthermore, it can be seen that even within the soft tissue window soft tissue and blood elements are mapped to similar grey scale values. To increase the visibility of blood or in consequence of blood vessels typically contrast agent is added. The iodine inside the contrast agent increases the CT values of the blood. This technique is called CTA (Kramme, 2017, p-317-336).

$$CT - value = 1000 \frac{\mu - \mu_{water}}{\mu} HU \tag{1.4}$$

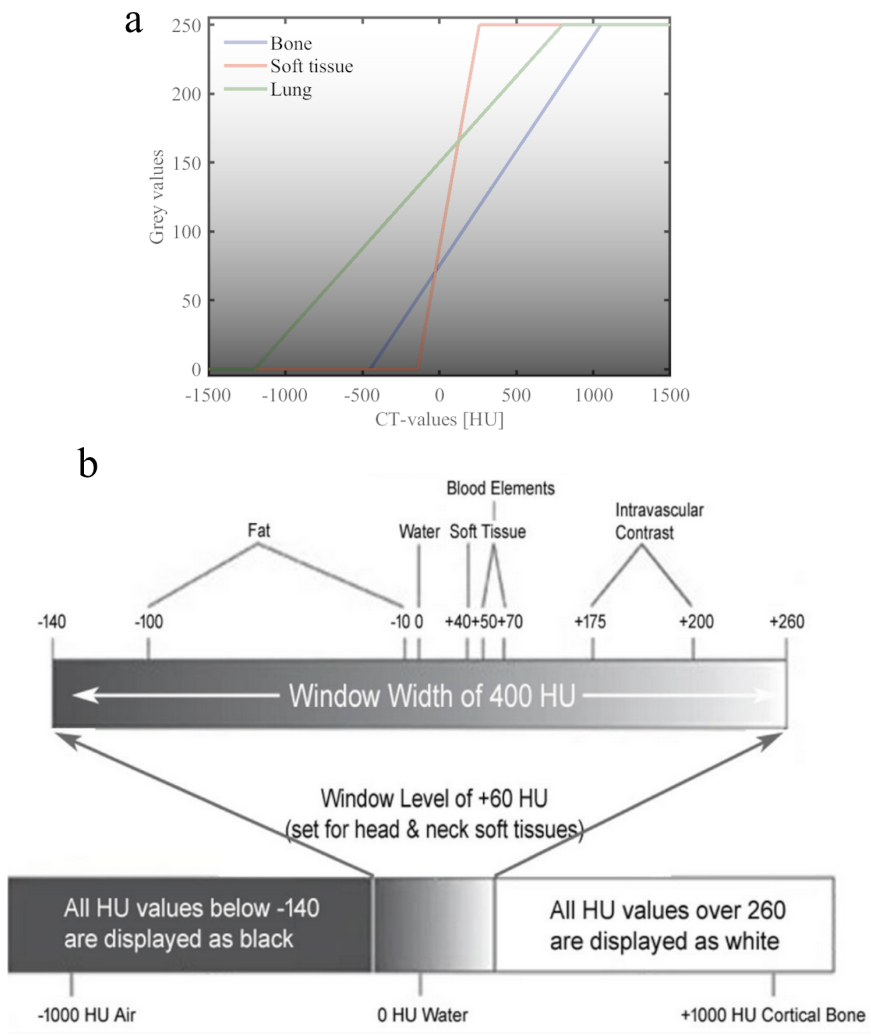

Figure 1.20: CT-windowing. a) The correlation of CT values and grey scale values depending on the observed tissue. b) A typical soft tissue window with a window level of +60 HU and a window width of 400 HU. CT = computed tomography. a) This figure was generated by me, based on (Kramme, 2017, p-317-336). b) This figure was originally published in (Yang, 2020), adapted and reused under the CC BY-NC-ND 4.0 - License .

Digital subtraction angiography

DSA is a special type of angiography used to display and evaluate blood vessels. DSA as shown in Figure 1.21 involves taking a series of X-ray images while a contrast agent is injected into the blood vessels. The X-ray images are then digitally subtracted from each other, resulting in clearer images of the blood vessels without the surrounding bone and tissue (Kramme and Kramme, 2017, p. 306-310). It provides real-time visualization of blood flow and helps guide minimally invasive procedures, such as angioplasty, stent-graft placement, and embolization. In contrast to CTA, for DSA the X-ray tube and the detector are stationary, and instead of cross-sectional views, projection images are created. DSA scanners are usually found in hybrid operation rooms.

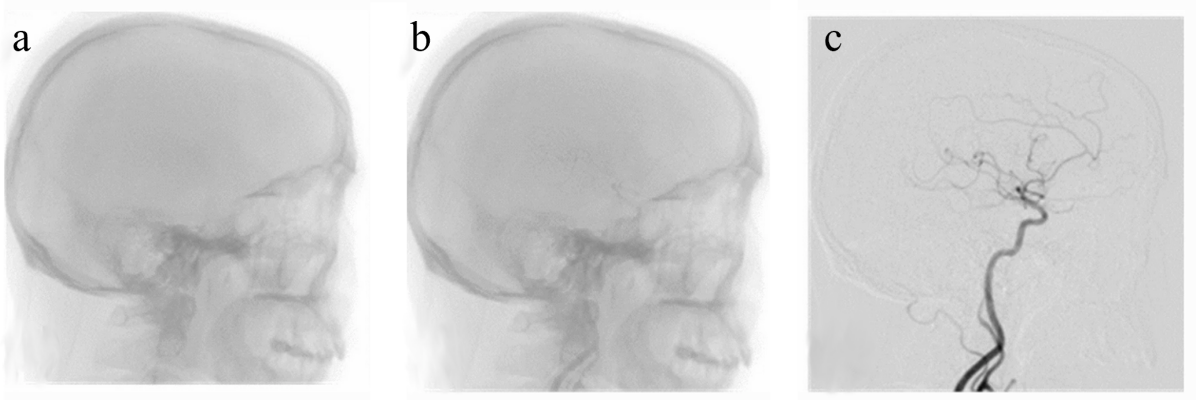

Figure 1.21: Digital subtraction angiography is performed by obtaining a mask image without contrast agent (a), a live image with contrast agent (b), and subtracting the mask image from the live image to get the DSA image (c). This figure was originally published in Gao et al. (2019), adapted and reused with permission.

1.3.4 3D printing

3D printing is an additive manufacturing method that produces parts, based on computer-aided design (CAD), by adding layers onto each other to create the final object. Its benefits are faster production times for small numbers of parts, less material waste, a wide combination of various materials with versatile features, and it allows for complex shapes, which are sometimes not producible with other manufacturing methods (Bhushan and Caspers, 2017). The disadvantages are slow and expensive production times for large numbers of parts, anisotropic material properties due to the layered approach, lower part quality, and sometimes requiring post-processing by traditional manufacturing methods Bhushan and Caspers (2017). Nowadays many different 3D printing technologies exist, which allow for a wide variety of materials or even a combination of different materials. Table 1.3 and Table 1.4. give an overview of the 3D printing technologies and materials used in this work.

Table 1.3: 3D printing technologies used in this work. Boldly written material groups are used in this work, † one material per print, * more than one material per print. Based on Bhushan and Caspers (2017).

Name	Technology	Layer height wall width	Materials	Comments	References
Fused deposition modeling	Extrusion	125-300 μm 600-1000 μm	**thermoplastics** metals composites	popular, fast, cheap, multi-material*, low resolution, poor quality	Shofner et al. (2003); Smith and Dean (2013); Mireles et al. (2013); Boschetto et al. (2012)
Stereo-lithography	Photopolymerization	1-50 μm 300-600 μm	**photoreactive polymers**, metals, ceramics	high resolution, medical applications, post-processing needed, single material†	Bartolo and Gaspar (2008); Bártolo (2011); Lee et al. (2006)
Multi Jet Modeling	Photopolymerization	15-50 μm 300-600 μm	**photoreactive polymers**	multi-material*, high resolution, expensive	Müller et al. (2014); Salmi et al. (2013)

Table 1.4: 3D printing materials used in this work. FDM = fused deposition modeling, MJM = multi jet modeling, MV = mitral valve, PLA = polylactide, PVA = polyvinylalcohol, SLA = stereolithography.

Company/Name	Material group	Printing technology	Features	Application
Ultimaker PLA	thermoplastics	FDM	cheap, easy to print, durable	MV molds
Ultimaker PVA	thermoplastics	FDM	water soluble	MV molds
Formlabs Clear Resin V4	photoreactive polymers	SLA	watertight, high resolution	simulator, tube connectors
Stratasys TangoPlus FLX930	photoreactive polymers	MJM	flexible	aorta phantom
Stratasys SUP706 B	photoreactive polymers	MJM	soluble	aorta phantom support

Fused deposition modeling

Fused deposition modeling (Figure 1.22), also called fused filament fabrication, is one of the most common 3D printing technologies (Hashmi, 2014).

The material, mostly thermoplastics, comes as filament loaded on a spool. The filament is pulled continuously by drive wheels into the extruder. Inside the extruder, the filament melts and flows through the nozzle onto the print bed. The extruder can travel in two directions and will follow the desired shape of the layer. After finishing the layer the often heated print bed lowers itself and the next layer will be printed. Some printers offer double extrusion, which combines multiple materials within one print. An often-used application of double extrusion is the use of water-soluble support materials such as polyvinylalcohol which can

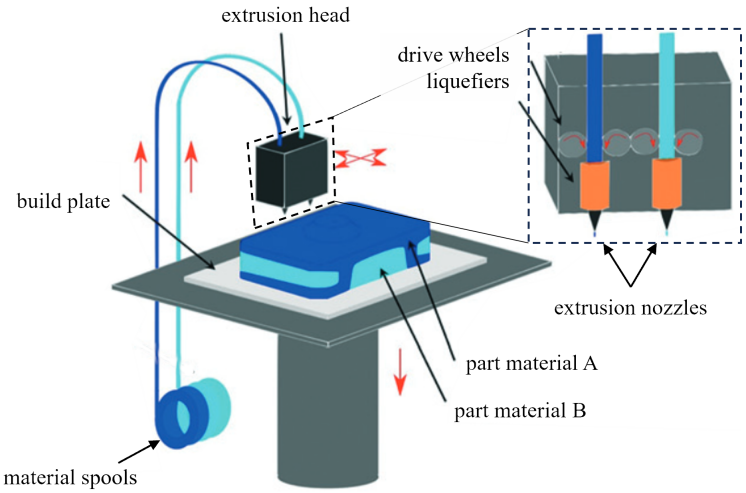

Figure 1.22: The basic principle of fused deposition modeling. Three-dimensional objects are constructed by layering and extruding thermoplastic materials through a heated nozzle. This figure was originally published in Bhattacharjee et al. (2016), adapted and reused with permission.

be washed out after printing, and therefore allow for printing overhanging shapes. The advantages of fused deposition modeling are simplicity, reliability, and affordability (Hashmi, 2014). The disadvantages are weak and anisotropic mechanical properties due to available materials and weak interlayer bonds (Friedrich and Walter, 2020), warping, low surface quality, and low resolution (Bhushan and Caspers, 2017).

Stereolithography

Stereolithography is a 3D printing technology where a liquid photosensitive resin is selectively exposed to UV light and consequently converted into a solid (Figure 1.23) (Rohani Shirvan et al., 2021). A tank is filled with the photosensitive polymer. The build platform is just below the surface of the liquid polymer. A scanning mirror guides the laser beam onto the build platform, follows the desired pattern of the layer, and selectively hardens the polymer by photopolymerization. Then the build platform lowers itself by the height of one layer. The sweeper levels the liquid and ensures equally distributed material. These steps are repeated until the whole part is printed. Stereolithography has the highest resolution and surface quality, but it is only possible to use one material per print (Bhushan and Caspers, 2017).

Multi jet modeling

Multi jet modeling, sometimes also called Polyjet or Photopolymer Inkjet Printing, combines the photopolymerization technology of stereolithography and the usage of multiple materials per print (Figure 1.24). The liquid materials get locally placed in the desired shape on the build platform and a UV lamp cures the extensive area. This turns the liquid into a solid polymer. Afterward, the build platform lowers itself by the height of one layer and the next layer can be printed. One of the major advantages is the possibility to use multiple materials

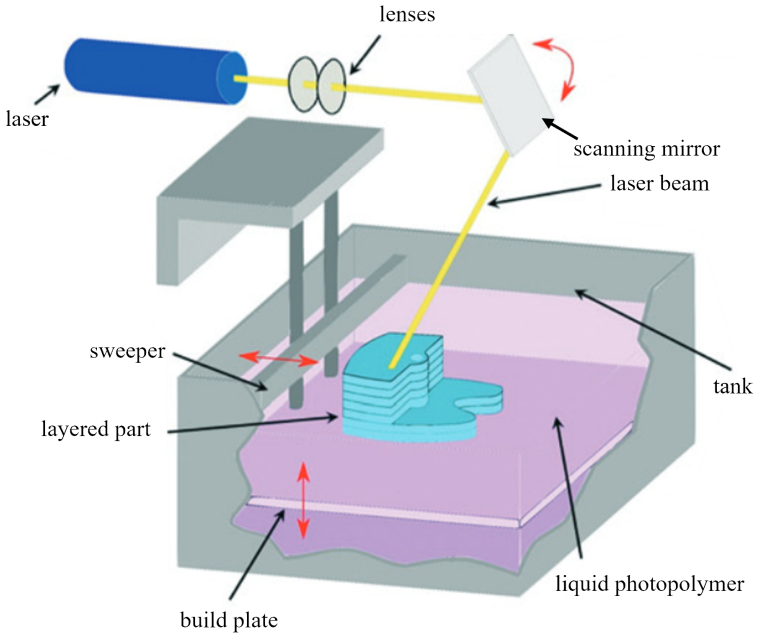

Figure 1.23: The basic principle of Stereolithography. Stereolithography uses a laser to cure liquid resin layer by layer, manufacturing detailed three-dimensional objects. This figure was originally published in Bhattacharjee et al. (2016), adapted and reused with permission.

per print, such as soluble support material, or polymers with different material properties (Bhattacharjee et al., 2016).

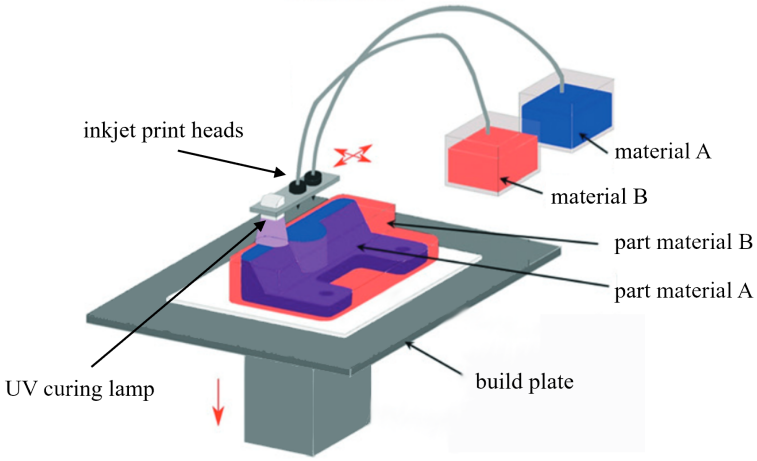

Figure 1.24: The basic principle of multi jet modeling. Multi jet modeling builds three-dimensional objects by selectively jetting and curing layers of liquid photopolymer using multiple print heads. This figure was originally published in Bhattacharjee et al. (2016), adapted and reused with permission.

1.3.5 Particle image velocimetry

PIV is an optical technique to measure the flow velocity of gases or liquids. PIV uses the light scatter of tracer particles to analyze the flow (Raffel et al., 2018, p. 5-14). To determine the flow velocity, the distance traveled by the particles in a known time has to be measured. This

is done by recording two images with a known distance of time (Raffel et al., 2018, p. 5-14). A typical PIV setup is shown in Figure 1.25.

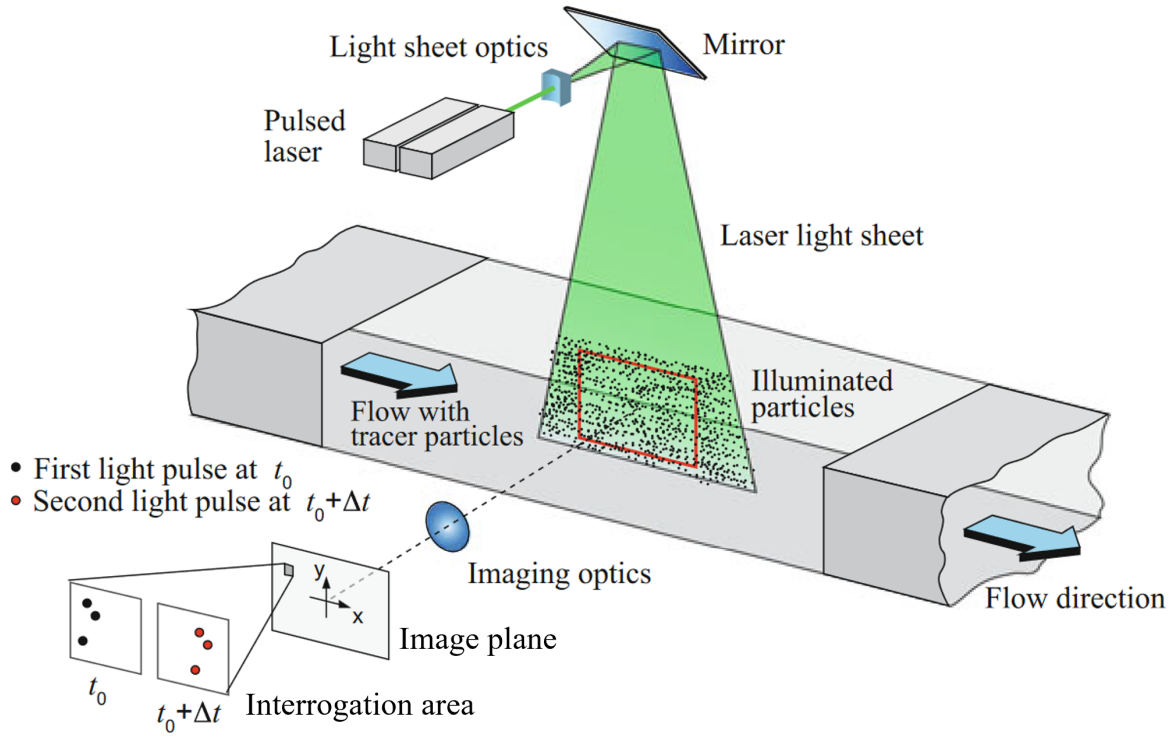

Figure 1.25: The principle of particle image velocimetry. Laser-illuminated particles within the flow are recorded within a defined temporal offset Δt. This figure was originally published in Raffel et al. (2018), reused with permission.

The fluid is seeded with tracer particles as liquids usually do not contain particles. These seedings are assumed to follow the flow dynamics of the fluid. Which can be quantified by the Stokes number for each flow scenario (Raffel et al., 2018, p. 5-14). To visualize the tracer particles suspended in the fluid, they are illuminated by a pulsed planar laser sheet. The reflection of the laser is recorded by a high-quality cross-correlation camera. The particles are illuminated twice within a short time interval t_0 and $t_0 + \Delta$ in order to analyze their deposition and saved into two different image frames. During the evaluation, the image is divided into small interrogation areas (Raffel et al., 2018, p. 5-14). Exemplary frames of the two time points t_0 and $t_0 + \Delta t$ of one interrogation area are shown in Figure 1.25 and in Figure 1.26.

The time delay of the laser pulses needs to be adjusted to the velocity of the fluid and imaging magnification to ensure that the majority of particles does not leave the interrogation area between the pulses (Raffel et al., 2018, p. 5-14). By cross-correlation of the position of particles in the first and second frame a local displacement vector for each interrogation area is calculated as shown in Figure 1.26. This cross-correlation is repeated for each interrogation area resulting in a flow field of the initially captured plane, as displayed in Figure 1.27.

Further post-processing might give further insights into the flow such as the vorticity (Raffel et al., 2018, p. 5-14).

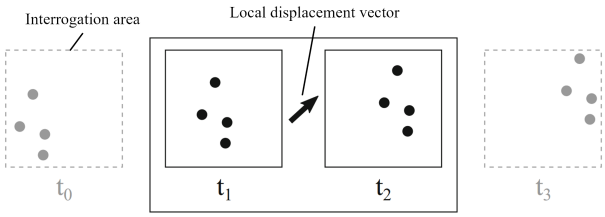

Figure 1.26: Particle displacement within one interrogation area between light pulses, with the local displacement vector between light pulse t_1 and t_2. This figure was originally published in Raffel et al. (2018), adapted and reused with permission.

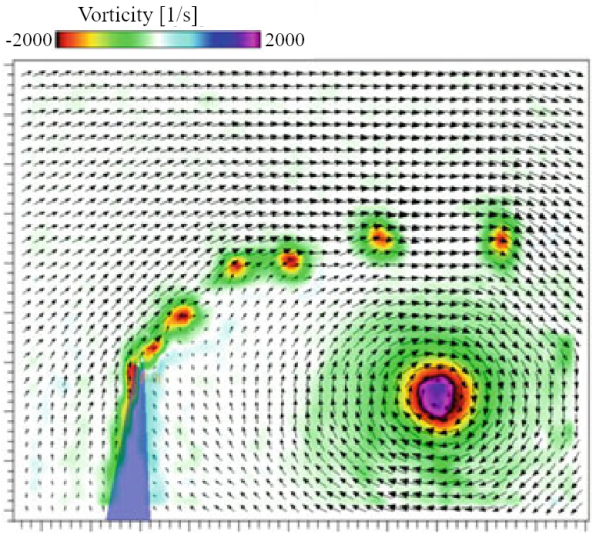

Figure 1.27: Velocity and vorticity field behind a wedge at the sudden onset of flow. This figure was originally published in Raffel et al. (2018), adapted and reused with permission.

PIV does not interfere with the flow and is therefore non-intrusive similar to ultrasound. It allows in the introduced setup the determination of 2 velocity components in a plane (2C-2D PIV), more complex setups even allow for 3 velocity components in a 3D volume (3C-3D PIV) and consequently a more detailed evaluation of the flow than other methods such as via pressure probes or rotational flow sensors such as an anemometer (Raffel et al., 2018, p. 5-14).

1.4 State of the art

This section provides a summary of contemporary research concepts relevant to the advancements of this thesis. Initially, existing simulators to train or plan mitral valve repair are discussed. Following that approaches to assess the flow convergence method are outlined. Lastly, approaches to train and plan transcatheter aortic repair are introduced.

1.4.1 Mitral valve repair simulators

Physical training in mitral valve repair is crucial due to the high complexity of interventions such as MIMVS or TEER. Multiple simulation environments, as visible in Table 1.5, have been developed. Despite sharing the same goal to provide a realistic training tool, the approaches differ clearly from each other. The simulator of Paulsen et al. (2020) stands in contrast to this goal since their intended use case was not training or planning of intervention, but research of the hemodynamics of mitral valves. However, the hemodynamic environment created is of interest for this work. Besides Gollmann-Tepeköylü et al. (2018), who chose an *ex-vivo* approach, other working groups focused on an *in-vitro* approach. Another main difference is that Fischer et al. (2023), Engelhardt et al. (2019), and Sardari Nia et al. (2019) developed a static simulator, without any valve movement or fluid, and Boone et al. (2019), Ginty et al. (2018), Ginty et al. (2019), Gollmann-Tepeköylü et al. (2018), and Zimmermann et al. (2021) developed (hemo-) dynamic simulators. While Gollmann-Tepeköylü et al. (2018)'s, and Zimmermann et al. (2021)'s target intervention was TEER, the others focused on surgical mitral valve repair. In the following, each of these mentioned differences will be illuminated.

Table 1.5: Comparison of mitral valve simulators proposed in literature. CT = chordae tendineae, LL = leaflets, MA = mitral annulus, MVR = surgical mitral valve repair, MIMVS = minimally invasive mitral valve surgery, PM = papillary muscles, TEE = transesophageal echocardiography, TEER = transcatheter edge-to-edge-repair.

Publication	Environment	Patient-specific	Interventions	Structures	TEE
Boone et al. (2019)	hemodynamic	yes	none	MA, LL	yes
Ginty et al. (2018, 2019)	hemodynamic	yes	MVR	MA, LL	yes
Engelhardt et al. (2019); Fischer et al. (2023)	static	yes	MIMVS	MA, LL, CT, PM	no
Sardari Nia et al. (2019)	static	no	MIMVS	MA, LL, PM	no
Gollmann-Tepeköylü et al. (2018)	dynamic	no	TEER	MA, LL, CT, PM	yes
Zimmermann et al. (2021)	dynamic	semi	TEER	LL, CT	no
Paulsen et al. (2020)	hemodynamic	no	none	MA, LL, CT, PM	yes

Hemodynamics

Fischer et al. (2023), Engelhardt et al. (2019), and Sardari Nia et al. (2019) used static simulators as visible in Figure 1.28 to train MIMVS. The benefits of these simulators are the easy

setup and use. They can be easily transported and used by anyone without certain technical knowledge. It is possible to access the mitral valve in a right lateral minithoracotmy-like way. Furthermore, their mitral valves, partially patient-specific allow for visual assessment of the mitral valve as well as the training of chordae-, leaflet-, and annuloplasty. While visual observation of the mitral valve and the repair is possible, a functional observation in terms of improved valve competency is not. Without any hemodynamics, the competency of a mitral valve cannot be evaluated, neither before, nor after repair. This disadvantage is addressed by Boone et al. (2019), Ginty et al. (2018), and Ginty et al. (2019) who introduced a hemodynamic simulator (Figure 1.29). The simulator comprises a flow-loop of the left heart including a pulsatile pump, left atrium, left ventricle, mitral valve, aortic valve, and a reservoir. While hemodynamics mimic known *in-vivo* conditions, the mitral valve has to be removed from the simulator to be repaired. While this is potentially time-consuming, it does not offer realistic access to the mitral valve. However, evaluation of the competency of the mitral valve before and after intervention was shown possible and is potentially promising.

TEER in humans is performed on the beating heart. Consequently, a dynamic simulation of the mitral valve opening and closing is required to allow for realistic training. Gollmann-Tepeköylü et al. (2018) solved this requirement by attaching a porcine heart to a pulsatile pump. This setup mimics a realistic mitral valve behavior and allows for training with TEER devices. However, realistic pressures and flows across the mitral valve are not reported and consequently cannot be evaluated. Zimmermann et al. (2021) introduced an approach where a motor mimics the mitral valve motion without any fluid flow. Consequently, this approach, similar to the static simulators mentioned above, does not allow for mitral valve competency evaluation. In conclusion, a hemodynamic design is required for the simulation of TEER interventions and a quantitative evaluation of the repair.

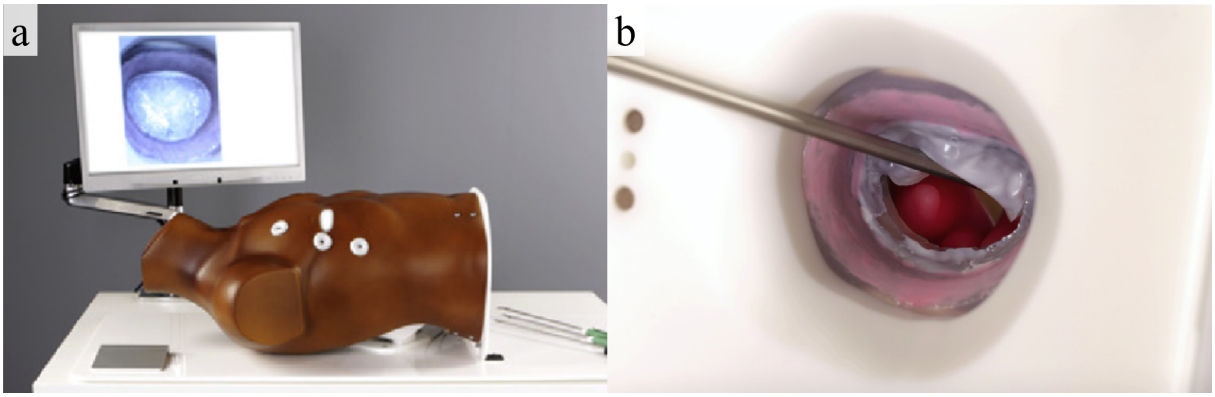

Figure 1.28: Static mitral valve simulator with atrial access to the mitral valve to train mitral valve surgery. a) Overview of the simulator. b) Atrial access to the mitral valve. This figure was originally published in Sardari Nia et al. (2019), adapted and reused with permission.

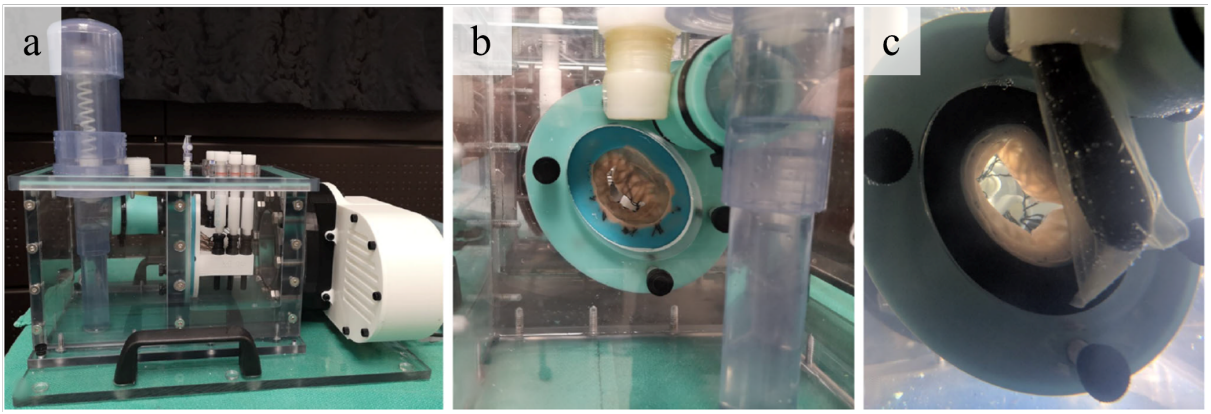

Figure 1.29: Dynamic mitral valve simulator(a), with a silicone mitral valve (b), and integrated transesophageal echocardiography probe (c). This figure was originally published in Ginty et al. (2019), adapted and reused with permission.

Personalized mitral valve repair training and planning

Training of mitral valve intervention such as TEER or MIMVS does not require patient-specific mitral valves. Consequently, simulators introduced by Sardari Nia et al. (2019) or Gollmann-Tepeköylü et al. (2018) allow physicians to train their techniques and gain experience. However, these approaches have limitations, especially the approach of Gollmann-Tepeköylü et al. (2018) which uses *ex-vivo* porcine hearts. Inducing primary mitral regurgitation such as chordae rupture might be feasible, but inducing secondary mitral regurgitation such as annulus dilatation on healthy porcine hearts is not possible. Patients with secondary mitral regurgitation are associated with extremely high morbidity and consequently with high potential for TEER (Layoun et al., 2023). However, their pathologies cannot be trained with the TEER simulator of Gollmann-Tepeköylü et al. (2018).

If planning interventions is a potential goal of a simulator, then personalized mitral valves, as displayed in Figure 1.30, have to be included. This approach was used by Boone et al. (2019), Ginty et al. (2018), Ginty et al. (2019), Fischer et al. (2023), and Engelhardt et al. (2019). Fischer et al. (2023) could show that patient-specific planning leads to better preparation of the intervention, reduces the time of initial inspection of the mitral valve, increases the understanding of pathomorphological features, and reduces the number of sizing attempts.

Interventions

MIMVS and TEER are the major treatments for mitral regurgitation. Consequently, these therapies are the ones mainly addressed by developed simulators. MIMVS requires a right lateral minithoracotomy-like access to the mitral valve as visible in Figure 1.31. Furthermore, MIMVS is performed at the arrested simulator. These conditions are provided by the simulators of Sardari Nia et al. (2019), Fischer et al. (2023), and Engelhardt et al. (2019). In contrast, TEER requires transseptal catheter access at a beating heart, as well as the integration of TEE or other imaging modalities as provided by Gollmann-Tepeköylü et al. (2018) and Zimmer-

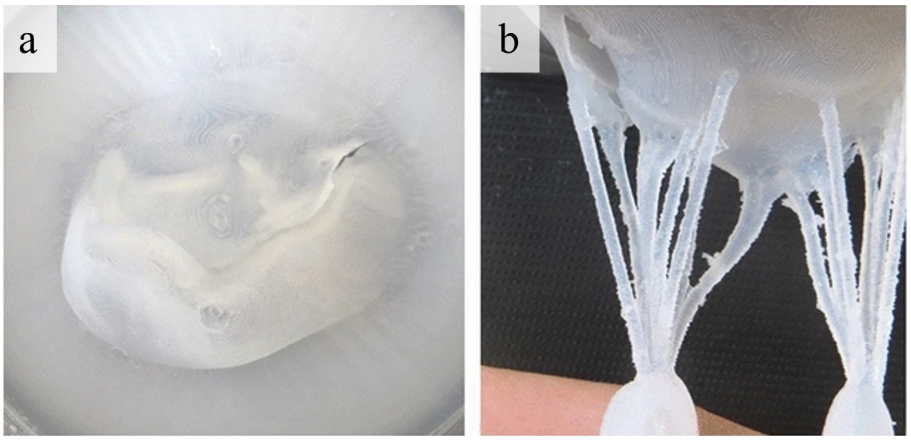

Figure 1.30: Patient-specific mitral valve out of silicone including the mitral annulus and leaflets (a), as well as the chordae tendineae and papillary muscles (b). This figure was originally published in Engelhardt et al. (2019), adapted and reused with permission.

mann et al. (2021). A simulator capable of providing the environment for both procedures and consequently allowing for the comparison of both procedures has not been introduced so far.

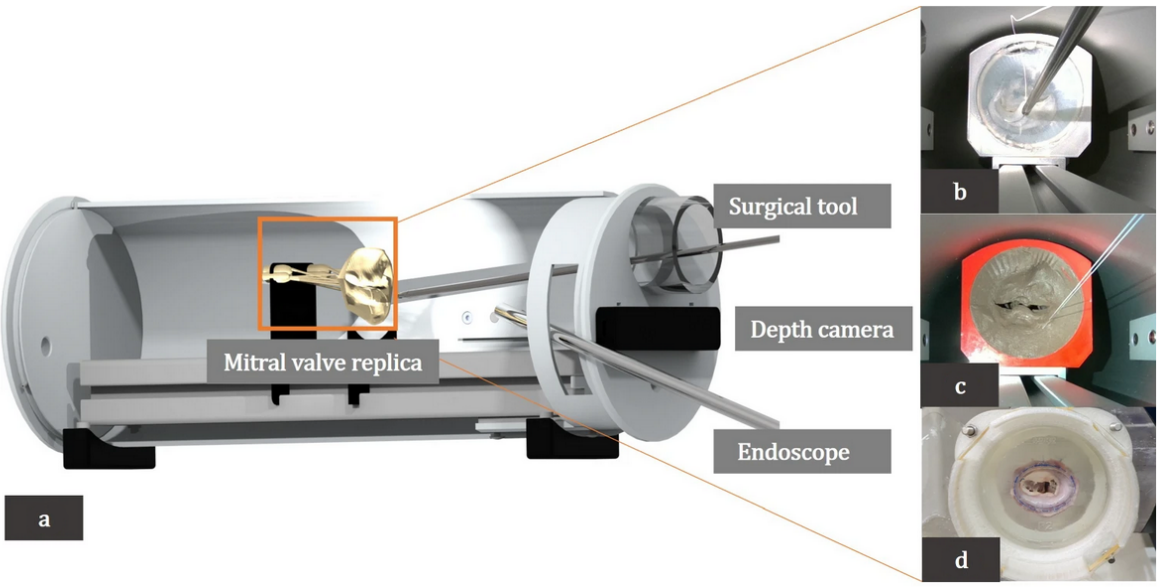

Figure 1.31: Right lateral minithoracotomy like access of a static simulator (a) with different mitral valves installed (b-d). This figure was originally published in Burger et al. (2023), adapted and reused under the CC BY 4.0 - Licence.

1.4.2 Assessment of the flow convergence method

Accurate assessment of mitral regurgitation is crucial to define the best treatment (Thavendiranathan et al., 2012). With the flow convergence method (echocardiography), also known as PISA method, cardiac catheterization (angiography), and cardiac magnetic resonance imaging, three techniques for grading mitral regurgitation are available. However, each of these techniques has its own advantages and disadvantages. Despite being the gold standard for

assessing mitral regurgitation, the flow convergence method is known for potentially underestimating the mitral regurgitation (Apostolakis and Baikoussis, 2009). This underestimation might consequently lead to insufficient therapy. To evaluate the accuracy of the flow convergence method several studies have been performed as displayed in Table 1.6. The major differences between studies were the environment of the assessment, which was either *in-vivo* or *in-vitro*, and the method the flow convergence method was compared with, which was either a medical imaging technology, such as cardiac catheterization, or a non-medical, such as PIV.

Environment to assess the flow convergence method

Assessing the flow convergence method was either done in an *in-vivo* environment on patients with mitral regurgitation or in an artificial *in-vitro* environment. Leśniak-Sobelga et al. (2002), Dujardin et al. (1997), and Iwakura et al. (2006) chose an *in-vivo* environment for their studies. The advantage of the *in-vivo* method is that the testing environment corresponds to the actual application environment, thus avoiding the occurrence of additional undesirable effects, such as unrealistic hemodynamics, or ultrasound artifacts.

One disadvantage of the *in-vivo* approach is the temporal offset between the examination of mitral regurgitation using the flow convergence method and the subsequent validation method. For example Dujardin et al. (1997) stated that cardiac catheterization and the flow convergence method were performed within a time frame of three months. During these three months, the hemodynamic situation within the patient might have changed. Even if, for example, the same severity grade of mitral regurgitation was diagnosed with a temporal offset between both methods, a) it does not mean that the same grade would have been diagnosed with both methods if the methods had been performed simultaneously, and b) the classification of a severity grade is still so broad that it does not allow us to infer whether the condition of the mitral regurgitation has changed. Therefore, to compare or even calibrate the flow convergence method the hemodynamics should be equal. Consequently, heartbeat, pressure, and flow should be identical.

Sonntag et al. (2014) and Coisne et al. (2002) used an *in-vitro* approach to overcome this obstacle. A flow-loop as shown in Figure 1.32a consisting of a pump, reservoir, and regurgitant model, was used. While in an *in-vivo* environment a realistic flow, even if variable, is ensured, in an *in-vitro* approach it has to be artificially created. Sonntag et al. (2014) however, used continuous flow and consequently did not produce a realistic pulsatile environment. The continuous flow caused the absence of a distinct pulsatile regurgitation jet. Without a pulsatile jet measuring of the regurgitation volume, and consequently the assessment of the flow convergence method is impossible. In contrast Coisne et al. (2002) presented a pulsatile *in-vitro* environment as displayed in Figure 1.32a. However, the authors report a period of 1620 ms for the pump cycle, which corresponds to a frequency of 37 bpm and lies without the physiological range of 60 - 80 bpm. In addition, no pressure measurements are reported.

Table 1.6: Approaches introduced in the literature to assess the flow-convergence method to quantify the severity of mitral regurgitation. The inter-observation effect assesses whether the validation method used for the flow convergence technique could influence the regurgitation itself.[1] = variation in relation to the observer (human), [2] = effect on hemodynamics between observation methods, [3] = the mitral regurgitation might be different due to a temporal offset between assessments. [4] = the method used has a low spatial, temporal, and vertical resolution. [5] = the hemodynamic environment is not physiological in terms of pressure or flow.

Publication	Environment	Validation	Nature of results	Observer variation[1]	Inter-observation effect[2]	Limitations
Leśniak-Sobelga et al. (2002)	*in-vivo*	angiography	quantitative	none	yes	reproducibility[3]
Dujardin et al. (1997)	*in-vivo*	angiography	quantitative	none	yes	reproducibility[3]
Iwakura et al. (2006)	*in-vivo*	3D-doppler echocardiography	quantitative	inter, intra	no	reproducibility[3]
Sonntag et al. (2014)	*in-vitro*	particle image velocimetry	qualitative	none	no	continuous flow
Coisne et al. (2002)	*in-vitro*	ultrasound	quantitative	none	no	low resolution[4], non-physiological flow[5]

Consequently, a statement whether the regurgitation corresponds with known *in-vivo* conditions in terms of temporal and spatial measures, could not be made.

Another obstacle of *in-vitro* approaches is the orifice shape. While the orifice shape in human mitral valves is rather elliptical or complex, Sonntag et al. (2014) and Coisne et al. (2002) used either circular, rectangular, or y-shaped orifices as displayed in Figure 1.32b,c,d (Lancellotti et al., 2010). The combination of non-physiological hemodynamics and orifice shapes raises the question if the flow convergence method can be assessed successfully with the absence of a realistic mitral regurgitation.

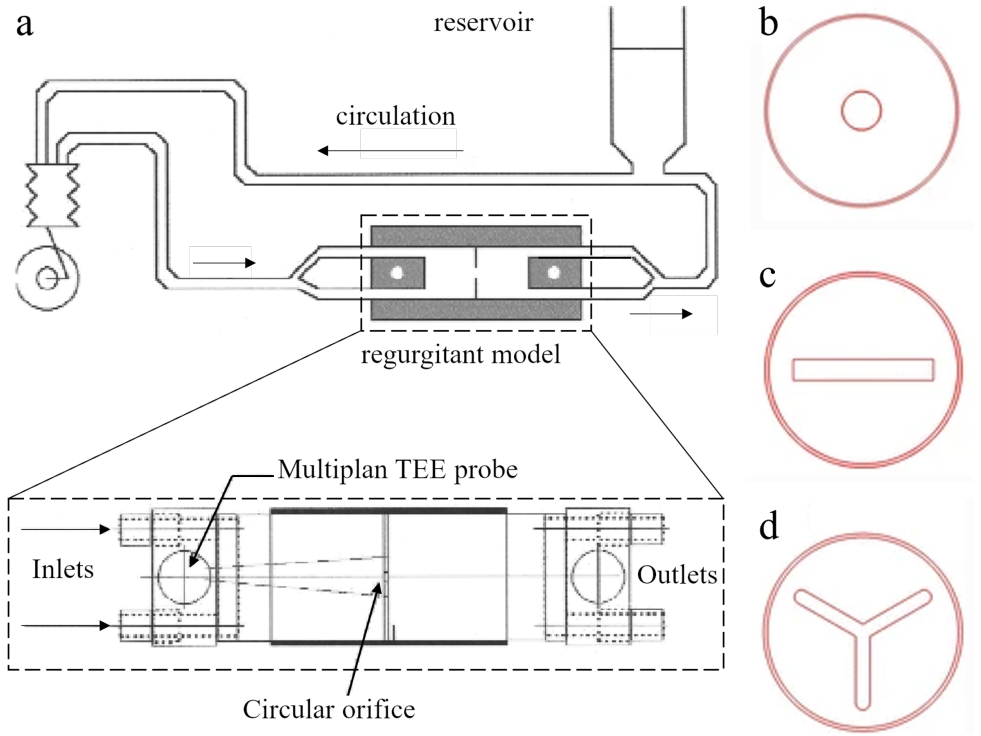

Figure 1.32: State of the art flow-loop (a) and orifice shapes (c-d) to evaluate the flow convergence method. This figure was originally published in a) Coisne et al. (2002) and b-d) Sonntag et al. (2014), adapted and reused with permission.

Validation methods to assess the flow convergence method

There are two major approaches to assess the flow convergence method: one involves medical imaging technologies, including cardiac catheterization, echocardiography, and cardiac magnetic resonance imaging; the other involves non-medical technologies, such as PIV. In their work Leśniak-Sobelga et al. (2002) and Dujardin et al. (1997) used cardiac catheterization and the flow convergence method to assess mitral regurgitation. They compared cardiac catheterization and the flow convergence method in terms of EROa and regurgitation volume. This use of two different imaging modalities has the advantage that limitations of for instance ultrasound do not impact the other technology. However, cardiac catheterization as a validation modality has its limitations. One of these, limitations is that cardiac catheter-

ization, as an invasive method, affects the hemodynamics of the patient. Consequently the results and comparability of cardiac catheterization and the flow convergence method are affected by an inter-observation effect (Apostolakis and Baikoussis, 2009). Moreover, the utilization of two different imaging modalities, which cannot be employed simultaneously, resulted in a temporal offset between assessments. This temporal offset as mentioned above, might affect the reproducibility of the hemodynamic situation inside the patient.

Iwakura et al. (2006) avoided the temporal offset and inter-observation effects by using different ultrasound modalities and compared them with each other. In essence Iwakura et al. (2006) compared the regurgitation orifice, manually acquired by using 3d ultrasound mode, and automatically acquired while performing the flow convergence method. This allowed the authors to perform both methods within one examination of the patient, minimizing the change of the hemodynamics. Furthermore, no inter-observation effect did influence the hemodynamics in different ways. However, limitations such as spatial, or temporal resolution of ultrasound which might result in inaccurate measurements, cannot be avoided. Furthermore, only one metric, the regurgitation orifice, of the flow convergence method could be assessed.

Coisne et al. (2002) also used ultrasound to assess the flow convergence method. In their setup, the raw data was used to calculate quantitative metrics separately. A major limitation of this approach was the low sampling rate of 10 fps and long sweep time of 30 ms. A systole only lasts for fractions of a second, so usually, less than five frames cover one systole. Furthermore, it took 30 ms to scan the entire field of view. Within this time frame the flow situation might change drastically, which might lead to shifts within the images. While this approach may seem promising in the present day with higher sampling rates, in the past, ultrasound technology was not sufficiently advanced.

Besides using medical imaging technologies, Sonntag et al. (2014) provided an approach to assess the flow convergence method using PIV. For *in-vivo* usage PIV is not feasible, due to the non-transparent properties of blood and the missing optical access to the heart. However, it is a non-invasive approach to assess flows and therefore there is no inter-observation effect between ultrasound and PIV. PIV is capable of determining quantities such as regurgitation volume and it allows for high sampling rates in a phase-resolved setup, where the pump and the PIV setup communicate.

Apart from the imaging method itself, the user plays a decisive role in the quality of the information obtained, especially with the flow convergence method (Apostolakis and Baikoussis, 2009). This represents a problem since a patient should get a diagnosis and therapy of equal quality independent of the physician. Consequently, the flow convergence method should be robust to lead to the same diagnosis independent of the physician. To assess the robustness the inter- and intra-observer variability has to be taken into account. However, this is only reported by Iwakura et al. (2006).

1.4.3 Aortic simulators

Numerous aortic flow-loops and phantoms have been created to perform pre-interventional assessments or to examine flow patterns in specific pathological conditions. The approaches employed encompass a range of options, including phantoms designed purely for visual assessments, flow-loops designed to simulate complete TEVAR procedures, models that span from abstract representations to patient-specific anatomical structures, and those that focus on only one segment of the aorta, such as the abdominal region, as well as those that encompass the entire aortic anatomy. A comprehensive overview is presented in Table 1.7.

Hemodynamics

The simplest approach for gathering information and becoming acquainted with a patient's pathology involves 3D printing a segmented aorta and visually examining the resulting phantom. This concept was pursued by researchers such as Rynio et al. (2019), Schmauss et al. (2014), Tong et al. (2020), and Little et al. (2022). They produced patient-specific aortic phantoms of the thoracic or abdominal regions, as depicted in Figure 1.33. Schmauss et al. (2014) employed 3D printing to create replicas of the aorta before (Figure 1.33a) and after (Figure 1.33b) intervention. These models proved useful for planning and assessing the outcomes of interventions. However, further investigations were conducted by Rynio et al. (2019) and Tong et al. (2020), who respectively evaluated the placement of stent-grafts in their thoracic and abdominal aortic phantoms (Figure 1.33c,d).

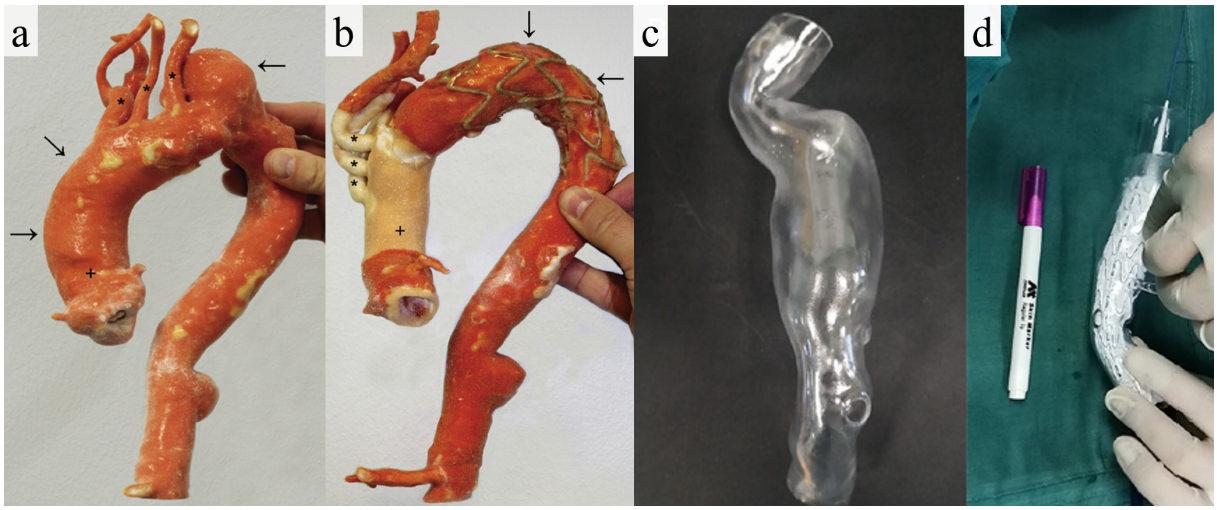

Figure 1.33: Aortic phantoms for static visual assessment. Thoracic phantom printed before (a) and after (b) frozen elephant trunk intervention. Abdominal aorta (c) to test stent-graft placement (d). This figure was originally published in (a,b) Schmauss et al. (2014) and (c,d) Tong et al. (2020), adapted and reused with permission.

To realistically plan the placement of a stent-graft or to evaluate the effects of stents on aortic dissections as well as aortic branches, a hemodynamic environment is necessary. Chung et al. (2000a) developed a flow-loop as presented in Figure 1.34 with a pulsatile pump, an

Table 1.7: Comparison of hemodynamic aortic simulators proposed in literature. AA = abdominal aorta, AAA = abdominal aortic aneurysm, CT = computed tomography, DSA = digital substraction angiography, EVAR = Endovascular aortic repair, FEVAR = fenestrated endovascular aortic repair, MRI = magnetic resonance imaging, TA = thoracic aorta, TAAA = thoracoabdominal aortic aneurysm, TAAD = type A aortic dissection, TBAD = type B aortic dissection, US = ultrasound.

Publication	Environment	Patient-specific	Therapy	Structure	Pathology	Imaging
Chung et al. (2000a)	hemodynamic	no	-	TA, AA	TBAD	-
Chung et al. (2000b)	hemodynamic	no	stent-graft	TA, AA	TBAD	-
Cloonan et al. (2014)	hemodynamic	no	-	AA	AAA	-
Mix et al. (2018)	hemodynamic	no	-	AA	AAA	US
Meess et al. (2017)	hemodynamic	yes	FEVAR	AA	AAA	DSA
Rudenick et al. (2013)	hemodynamic	no	-	TA	TBAD	US
Rynio et al. (2019)	static	yes	TEVAR	TA	TAAA	-
Schmauss et al. (2014)	static	yes	-	TA	TAAA	-
Sommer et al. (2018)	hemodynamic	yes	-	AA	-	-
Tong et al. (2020)	static	yes	stent-graft	AA	TAAA	-
Little et al. (2022)	static	yes	EVAR	AA	AAA	US, CT
Urbina et al. (2016)	hemodynamic	no	-	TA	-	MRI
Arakawa et al. (2022)	hemodynamic	yes	TEVAR	TA	TAAD	-
Ramella et al. (2022)	hemodynamic	no	TEVAR	TA	-	CT
Torres and de Luccia (2017)	hemodynamic	yes	EVAR	AA	AAA	-

aortic phantom, including the entire aorta, major aortic branches, as well as a dissection membrane (intimal flap), and reservoirs. This setup allowed for frequencies between 30 - 120 bpm, flows of up to 6.75 l/min, and systolic pressures of 120 - 152 mmHg. While this setup provided lifelike hemodynamics, an opportunity to train interventions, such as femoral access for TEVAR, was not included. This improvement was made by Meess et al. (2017),

Arakawa et al. (2022), and Ramella et al. (2022). While allowing for endovascular repair within their flow-loops, their aortic phantoms represented only the abdominal, or thoracic aorta. This approach was feasible for Meess et al. (2017) due to a pathology within the abdominal aorta. In contrast, conditions involving the thoracic aorta, such as TBAD, necessitate an aortic phantom spanning the entire length of the aorta to comprehensively assess all hemodynamic effects on aortic branches.

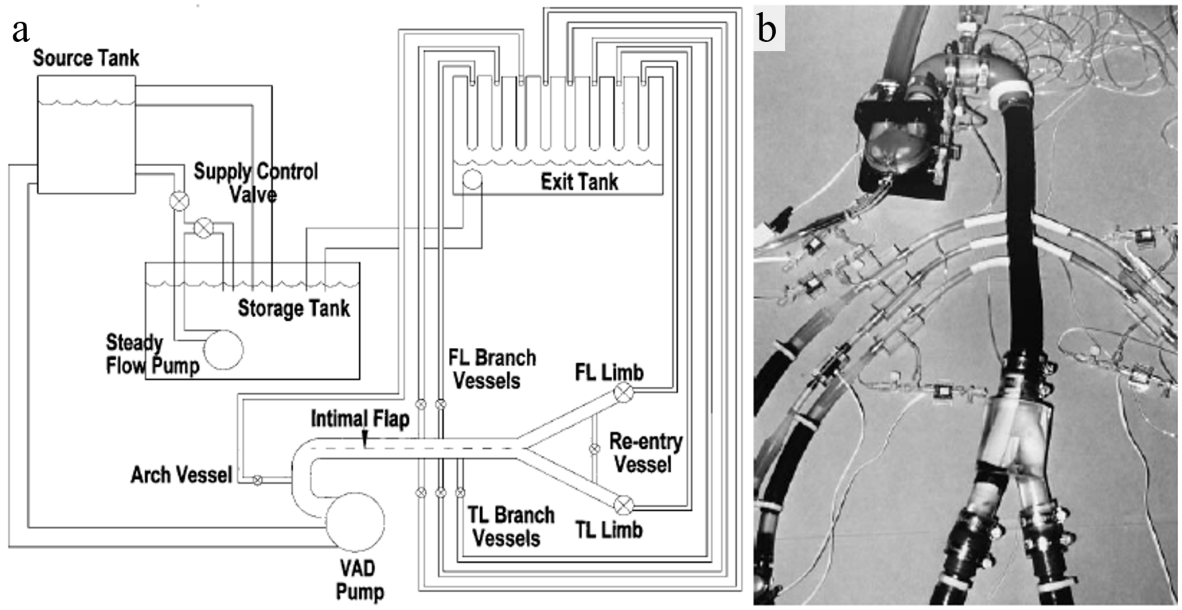

Figure 1.34: Aortic flow-loop (a) including an aortic phantom (b) with an aortic dissection pathology. FL = false lumen, TL = true lumen, VAD = ventricular assist device. This figure was originally published in Chung et al. (2000a), adapted and reused with permission.

Personalization

Pathologies, interventions, and their hemodynamic effects, are highly individual. The entry and course of dissection and aorta differ from patient to patient. A stent-graft placement that fits one patient, might not fit the other due to anatomical peculiarities. While for basic research non-personalized models, such as those used by Chung et al. (2000a) (Figure 1.34), Cloonan et al. (2014), Mix et al. (2018), Rudenick et al. (2013), Ramella et al. (2022), might be useful to understand flow and hemodynamics. For training and intervention planning patient-specific aortic phantoms with realistic hemodynamics are required.

Rynio et al. (2019) developed such a patient-specific phantom to train the treatment of a thoracoabdominal aortic aneurysm by TEVAR. Torres and de Luccia (2017) and Meess et al. (2017) developed patient-specific hemodynamic simulators to train endovascular aortic repair and fenestrated endovascular aortic repair to treat abdominal aortic aneurysms. TAAD dissections can be trained with the simulator of Arakawa et al. (2022). However, the access for stent-grafts in this simulator is trans-apical, which does not correspond to a realistic clinical scenario. As of now, a simulator designed to address TBAD within a hemodynamic patient-specific environment has not been developed. The prospect of utilizing a patient-specific

aortic phantom, spanning the complete length of the aorta, within a hemodynamic context and incorporating femoral access, holds potential for simulating endovascular aortic repair procedures to address TAAD, TBAD, and abdominal aortic aneurysms.

Medical imaging

The diagnosis and planning of interventions for aortic pathologies like TBAD by vascular surgeons heavily relies on medical imaging, particularly CTA. During procedures such as TEVAR, DSA becomes necessary to guide catheter devices through the aorta and evaluate the placement of stent-grafts. To accurately simulate this process, the flow-loop must be compatible with the imaging techniques used in CTA and DSA.
The compatibility with DSA has been successfully demonstrated by Meess et al. (2017), and CT scans were conducted as reported in the works of Ramella et al. (2022) and Little et al. (2022). However, the CT scans were performed without the application of a contrast agent. Furthermore, their phantoms were not connected to the flow-loop during the CT scans. The utilization of a contrast agent has the potential to enhance the visibility of the aorta. To ensure proper distribution of the contrast agent, a flow would be necessary, introducing increased complexity to the setup, particularly within the confined space of a CT scanner. This advancement is an area that is yet to be explored and developed.

2 Materials and Methods

This chapter covers the materials and methods for the development and validation of the mitral valve simulator in Section 2.1, the quantification of mitral regurgitation in Section 2.2, and the development and validation of the aortic valve simulator in Section 2.3.

2.1 Mitral valve simulator

Parts described in this chapter are published (Karl et al., 2024). The text has been rewritten for this thesis.

Objective I of this thesis was to create and verify a left heart simulator capable of serving training and personalized planning purposes related to mitral regurgitation and its treatment interventions. Besides training and planning one aim of the simulator was to answer research questions related to the mitral valve, its pathologies, and treatments. One of these questions relates to the accuracy of TEE and the flow convergence method to quantitatively grade mitral regurgitation. This was investigated by comparing it to an additional flow observation method called PIV and is covered in Sections 2.2, 3.2, and 4.2.

2.1.1 Requirements

Mitral valve simulator design was focused on the requirements (MVS-R) set to train and plan MIMVS and TEER as they are the most common examples of surgical and percutaneous interventions, respectively.

MVS-R1 - Integration of entire mitral valve anatomy: The mitral valve is a complex system, in which each part of the apparatus plays a crucial role in its function. Mitral regurgitation might be caused by failures of any part of the mitral valve apparatus and repair may consequently also affect any part of the mitral valve apparatus. Therefore, the whole mitral valve apparatus, including the mitral annulus, leaflets, chordae tendineae, and papillary muscles, should be functionally included in the simulator.

MVS-R2 - Realistic hemodynamics: The closing of the mitral valve during systole and its opening during diastole is highly dependent on the flow and pressure in the left atrium and left ventricle. Therefore, a hemodynamic environment providing physiological flow and pressure across the mitral valve and consequently within the left heart should be provided.

MVS-R3 - Right lateral minithoracotomy: As MIMVS is typically performed on the arresting heart, a simulator should provide a function to stop the hemodynamics and create a right lateral minithoracotomy-like environment. Due to the strict time schedule of physicians, the transition from hemodynamic (MVS-R2) to thoracotomylike environment and reverse should only require minutes in order to maximize the time available for training, planning, and evaluation.

MVS-R4 - Trans-septal access: During TEER the catheter devices enter the left atrium transseptal. Therefore, trans-septal access is required in order to simulate TEER procedures at the simulator.

MVS-R5 - TEE integration: TEE is used to diagnose and grade mitral regurgitation as well as to evaluate the state of the mitral valve before, during, and after intervention. Especially for TEER TEE is crucial for navigation. Hence, a TEE probe should be integrated to ensure proper evaluation of the pathological and repaired mitral valves, and guiding during TEER. The integration of the TEE probe should result in a realistic orientation.

MVS-R6 - Precise live monitoring: While TEE is the most common medical imaging technology used during mitral valve repair, it requires human and hardware resources which are often tied to clinical routine. Live monitoring of the hemodynamics however, can also be facilitated by commercially available pressure and flow sensors as well as high-speed cameras, which can easily be used without special experience.

2.1.2 Simulator design

The design of the simulator (Figure 2.1a-c) took inspiration from the heart's anatomy to establish a lifelike hemodynamic environment (MVS-R2). The simulator is comprised of a reservoir, a left atrium, a left ventricle, a mitral valve, and an aortic valve. A modular design of the simulator allows for future developments and extensions. Each part can be exchanged by a modified version separately. The blood-mimicking fluid flows from the reservoir, into the attached left atrium (Figure 2.1b). The left atrium is separated from the left ventricle by the mitral valve. From the left ventricle, the blood-mimicking fluid flows through the aortic valve back into the reservoir.

The simulator is driven by a pulsatile cardiac piston pump, SuperPump, in combination with the viscoelastic impedance adapter (both ViVitro Labs, Inc., Victoria, BC, Canada) which are connected to the left ventricle. The displacement of the piston mimics the contraction and relaxation of the left ventricle by reducing and increasing the volume of the left ventricle, respectively. The pump allows for a variety of preset and customized waveforms (Figure 2.2), the adjustment of stroke volume (0 - 180 ml), and frequency (3 - 200 bpm), to mimic different pathologies and conditions of the heart.

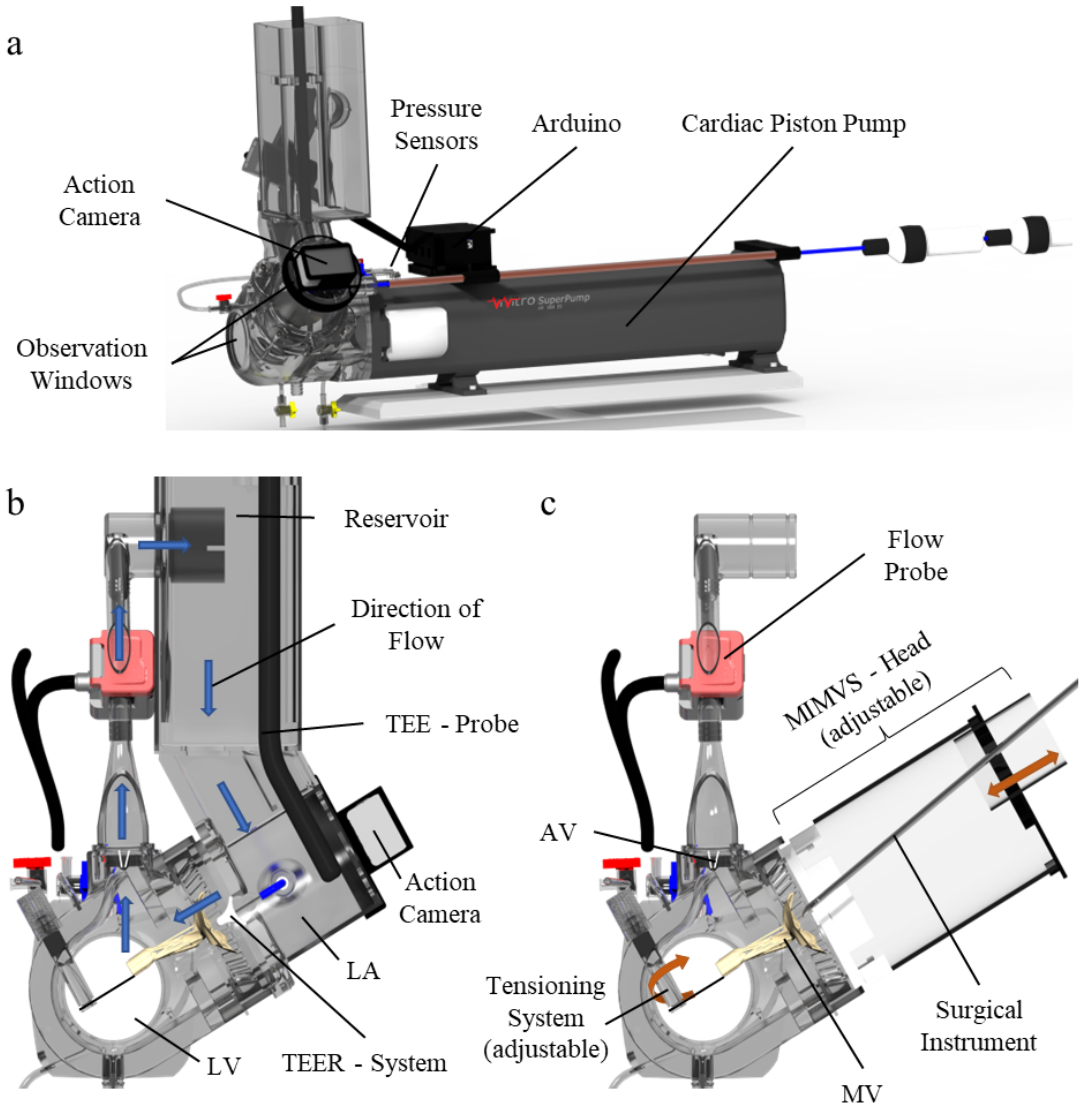

Figure 2.1: Mitral valve simulator in hemodynamic configuration for observation and TEER in total view (a), side-cross-section view (b), and in right lateral minithoracotomy-configuration for MIMVS in side-cross-section view (c). AV = aortic valve, LA = left atrium, LV = left ventricle, MIMVS = minimally invasive mitral valve surgery, MV = mitral valve, TEE = transesophageal echocardiography, TEER = transcatheter edge-to-edge repair. This figure was originally published in Karl et al. (2024), adapted and reused under the CC BY 4.0 - Licence.

The viscoelastic impedance adapter incorporates two compliance chambers. The volumes of the compliance chambers can be adjusted continuously and hold a total volume of 200 ml. The viscoelastic impedance adapter mimics the windkessel effect of the aorta. This windkessel effect is the ability to absorb fluid pressure peaks. Arteries such as the aorta achieve this by stretching their elastic walls. Within the simulator, this effect is created by the compression of gas (air) inside the compliance chambers of the viscoelastic impedance adapter. The more the compliance chambers are filled with gas, the bigger the absorbing effect.

The simulator was designed by using the computer-aided design software Creo Parametric 9.0 (PTC Inc., Boston, Massachusetts, United States). The left atrium, left ventricle, reservoir,

and chordae tensioning system were printed out of Clear V4 resin on a Form 3B 3D printer (both formlabs, Somerville, Massachusetts, United States) with stereolithography technology.

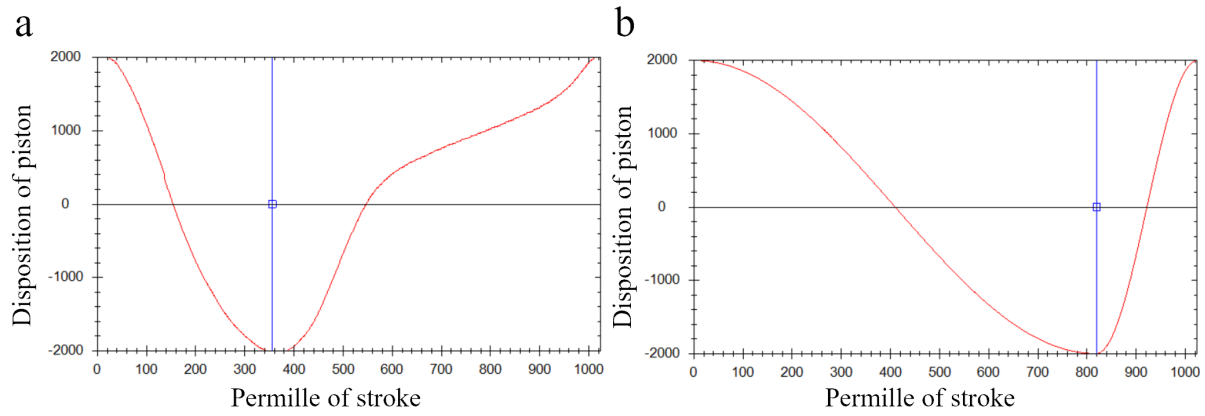

Figure 2.2: Pre-installed so-called physio (a) and sine 80 % (b) waveforms of the pulsatile cardiac piston pump. The disposition of the piston and the time of one stroke are in relation to the selected stroke volume and frequency respectively.

A 27 mm mechanical prosthetic valve (27 AHPJ-505, Abbott Laboratories, Illinois, USA) serves as the aortic valve. The mitral valve is placed in a rigid frame that is clamped between the left atrium and left ventricle by four screws. This allows for rapid exchange of the mitral valve. The papillary muscles of the mitral valve are connected to the tensioning system sitting at the apex of the ventricle. The tensioning system operates akin to a winch, enabling a continuous adjustment of both force and length. This ensures the functional integration of the whole mitral valve apparatus (MVS-R1).

To enable MIMVS a right lateral minithoracotomy-like access (MVS-R3) was required. This requirement was met by replacing the left atrium with an MIMVS-head (Figure 2.1c), which enables narrow access with an opening diameter of 50 mm and an adjustable distance of 150 - 155 mm between the opening and the annulus plane. The exchange of the left atrium and MIMVS-head is done via the four screws mentioned above and takes a few seconds.

To enable the performance of TEER (MVS-R4) a transseptal port (Figure 2.1b) was integrated into the left atrium with a distance of 45 mm to the annulus plane. To allow the use of TEE, access through the reservoir into the left atrium was integrated (Figure 2.1b). In the human body, the TEE probe does not sit inside the left atrium, but inside the esophagus. The integration of a TEE probe into the left atrium, and consequently the enlargement of the left atrium, is a simplification that allows for a similar to *in-vivo* orientation of the TEE probe without adding structure to the simulator.

Windows at the left atrium and left ventricle (Figure 2.1a) allow for visual observation of the flow, mitral valve, or treatments. Live video guidance during TEER is enabled by an action camera, attached to the window at the left atrium. In clinical routine, fluoroscopy is used in combination with TEE for guidance. In this setup, video guidance was used instead to avoid radiation, increase flexibility, and ease access. Flow sensors (Sonoflow CO.55 V2.0, SONOTEC GmbH, Halle (Saale), Germany) located between the aortic valve and the reservoir and pressure sensors (ABPDRRT005PG2A5, Honeywell International Inc., North Carolina, USA) at the left ventricle and left atrium enable precise quantification of the hemodynamic situation (MVS-R6).

2.1.3 Blood-mimicking fluid

The blood-mimicking fluid plays a crucial role in the hemodynamic environment (MVS-R2). Lifelike hemodynamics require the blood-mimicking fluid to behave similar to blood to enable realistic flow. Human blood is a non-Newtonian fluid, which means that the relation of shear stress and shear rate is not linear, or in essence the viscosity is not constant; however, in large blood vessels, blood can be considered a Newtonian fluid, such as water, of high shear rate (Pedley, 2012), with a viscosity of 3 - 6 mPa/s (Samavat and Evans, 2006; Nader et al., 2019). A fluid mixture of 30 % glycerol and 70 % water (Leibuss et al., 2022) was used during the experiments. The mixture has a viscosity of 3 mPa/s at room temperature (~20 °C) (Westbrook, 2018).

Ultrasound measurements commonly employed in clinical practice, such as TEE, rely on the sound backscatter properties of erythrocytes in human blood. The backscatter properties of blood are defined by the size of erythrocytes, 6 - 8 μm (Ward et al., 2018, p. 372). Cornstarch, with a particle size of 5 - 10 μm, corresponds well to erythrocytes and the corresponding backscatter (Leibuss et al., 2022). Therefore, 1 % cornstarch was added to the blood-mimicking fluid for all experiments with ultrasound measurements.

2.1.4 Sensors

Ultrasound data

The two ultrasound systems that were most available in the department of cardiac surgery and cardiology of the university hospital of Heidelberg were used. The department of cardiac surgery predominantly used the ultrasound system by Koninklijke Philips N.V., Amsterdam, Netherlands, while the department of cardiology used the system by General Electric Company, Massachusetts, USA. Both systems require the recordings to be exported and subsequently processed on a computer with a Digital Imaging and Communications in Medicine (DICOM)-reader. The ultrasound hard- and software used in this thesis are shown in Table 2.1.

Table 2.1: Data acquisition of ultrasound systems. DICOM = Digital Imaging and Communications in Medicine, MITK = Medical Imaging Interaction Toolkit by German Cancer Research Center, Heidelberg, Germany, TEE = transesophageal echocardiography, US = ultrasound.

Company	US system	3D TEE probe	File format	DICOM reader
Koninklijke Philips N.V.	EPIQ CVx	X8-2T	VOLDicom	Q-Lab
General Electric Company	Vivid E9	6VT-D	VOLDicom	MITK

Pressure and flow data

The pressure and flow data was transferred via the inter-integrated circuit digital communication system from the sensors to an Arduino clone (ATmega328 Microcontroller Board by AZ-Delivery Vertriebs GmbH, Germany) (Figure 2.3). The script on the ATmega328, called Arduino Sketch, measured the analog current signal of the flow sensors and converted it into ml/s. Furthermore, it converted the digital signal of the pressure sensors into mmHg and transferred all values via a universal serial bus, also known as USB, to the computer. The Python script on the computer enabled live monitoring of all measured values, as shown in Figure 2.4, and saved them as a CSV file. In addition, it calculated the stroke volume (ml/Stroke) and cardiac output (l/min) over the last five seconds in real time for live monitoring. Each recording covered a period of 30 s.

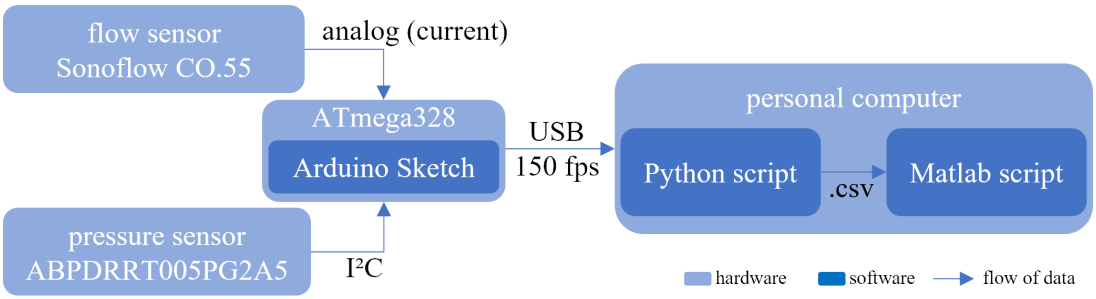

Figure 2.3: Data processing of pressure and flow. .csv = comma-separated values - text file, fps = frames per second - data speed, I^2C = Inter-integrated circuit - protocol to transfer data, USB = universal serial bus - physical interface and protocol to transfer data .

A Matlab script was used to process and visualize the data as it can be seen in the results section. Besides more precise calculations of stroke volume and cardiac output, the transmitral gradient, average systolic pressure, regurgitation volume, and regurgitation fraction were determined. According to the continuity equation (Figure 2.5), the regurgitation volume (RVol) is calculated out of the set displacement of the piston (SV_{pump}), the calculated compliance volume compression (CVC), and the measured stroke volume of the left ventricle (SV_{LV}) (Equation 2.1).

$$RVol = SV_{pump} - SV_{LV} - CVC \tag{2.1}$$

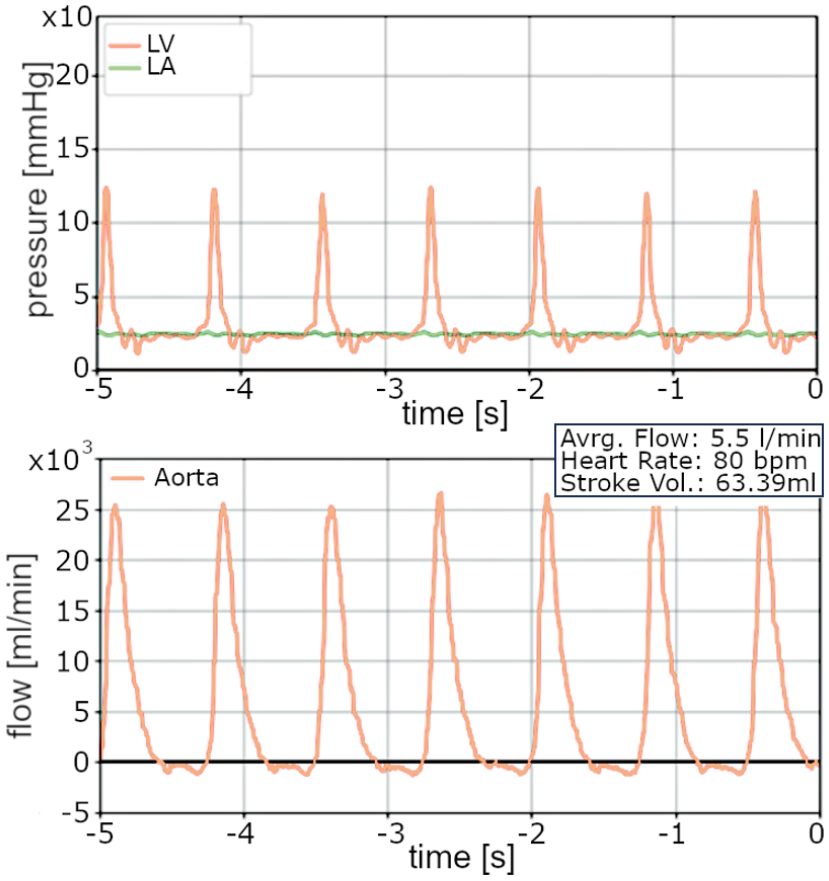

Figure 2.4: Live monitoring of pressure and flow visualizing the last five seconds and a calculation of the cardiac output and stroke volume over the last five seconds. Avrg. = average, LA = left atrium, LV = left ventricle, Vol. = volume

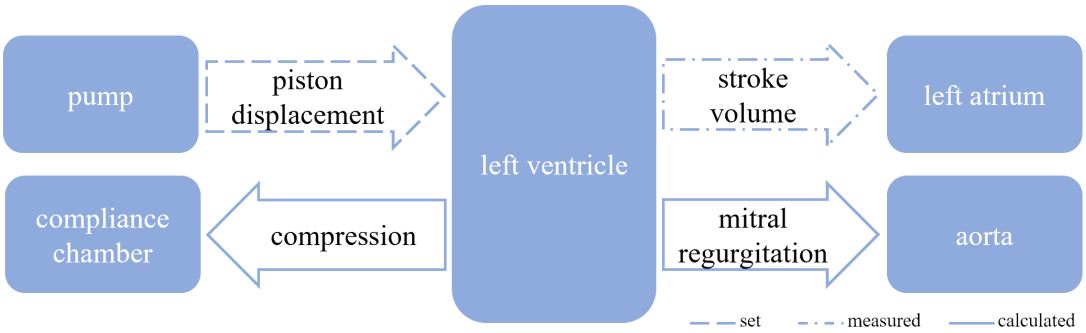

Figure 2.5: Visualisation of the continuity equation for the mitral valve simulator. All flows from and to the left ventricle are taken into account.

The regurgitation fraction (RF) is the regurgitation volume (RVol) divided by the flow from the left atrium to the left ventricle as visible in Equation 2.2. The flow from the left atrium to the left ventricle is calculated as the difference between the SV_{pump} and CVC.

$$RF = \frac{RVol}{SV_{pump} - CVC} \tag{2.2}$$

The CVC IS calculated according to the ideal gas law, from the measured absolute pressure of the left ventricle during end-diastole (P_{LVED}) and during mid-systole (P_{LVMS}) (Equation 2.3).

$$CVC = 1 - \frac{P_{LVED}}{P_{LVMS}} \tag{2.3}$$

Classification of mitral regurgitation

The mitral valves assessed during the experiments were classified. This allowed for the evaluation of experiments by comparing the grade of severity e.g. before and after implementing therapy.

Dujardin et al. (1997) established a classification of mitral regurgitation severity based on regurgitation volume and regurgitation fraction. They designated mitral regurgitation with a regurgitation volume < 30 ml and a regurgitation fraction < 30 % as grade 1. Mitral regurgitation with a regurgitation volume of 30 - 44 ml and a regurgitation fraction of 30 - 39 % was categorized as grade 2, while mitral regurgitation with a regurgitation volume of 45 - 59 ml and a regurgitation fraction of 40 - 49 % was classified as grade 3. Mitral regurgitation with even larger regurgitation volume and regurgitation fraction were categorized as grade 4. In this study, the grading system was extended by introducing grade 0, defined as mitral regurgitation with a regurgitation volume < 12 ml and a regurgitation fraction < 19 %. Although some overlap between grades can be expected, this classification scheme offers additional categorization.

Mitral valves were classified as physiological if they elicited a systolic blood pressure of 90 - 120 mmHg, a cardiac output of 4.5 - 5 l/min, and if their mitral regurgitation was classified as grade 0. Mitral valves with a grade above 0 were considered pathological. Successful repair was defined as MIMVS or TEER resulting in a reduction of mitral regurgitation grade.

2.1.5 Experiments

To validate the simulator in regard to the requirements, several mitral valve models were installed in the simulator and evaluated as described in the following. Figure 2.6 provides an overview of the experiments conducted and the requirements evaluated with each mitral valve. The waveform displayed in Figure 2.2a was used for all experiments. A video of all experiments can be found here (Karl et al., 2024). Ethical approval was obtained from the Ethics Committee of the Faculty of Medicine of Ruprecht-Karls-University Heidelberg, Germany (S777/2019).

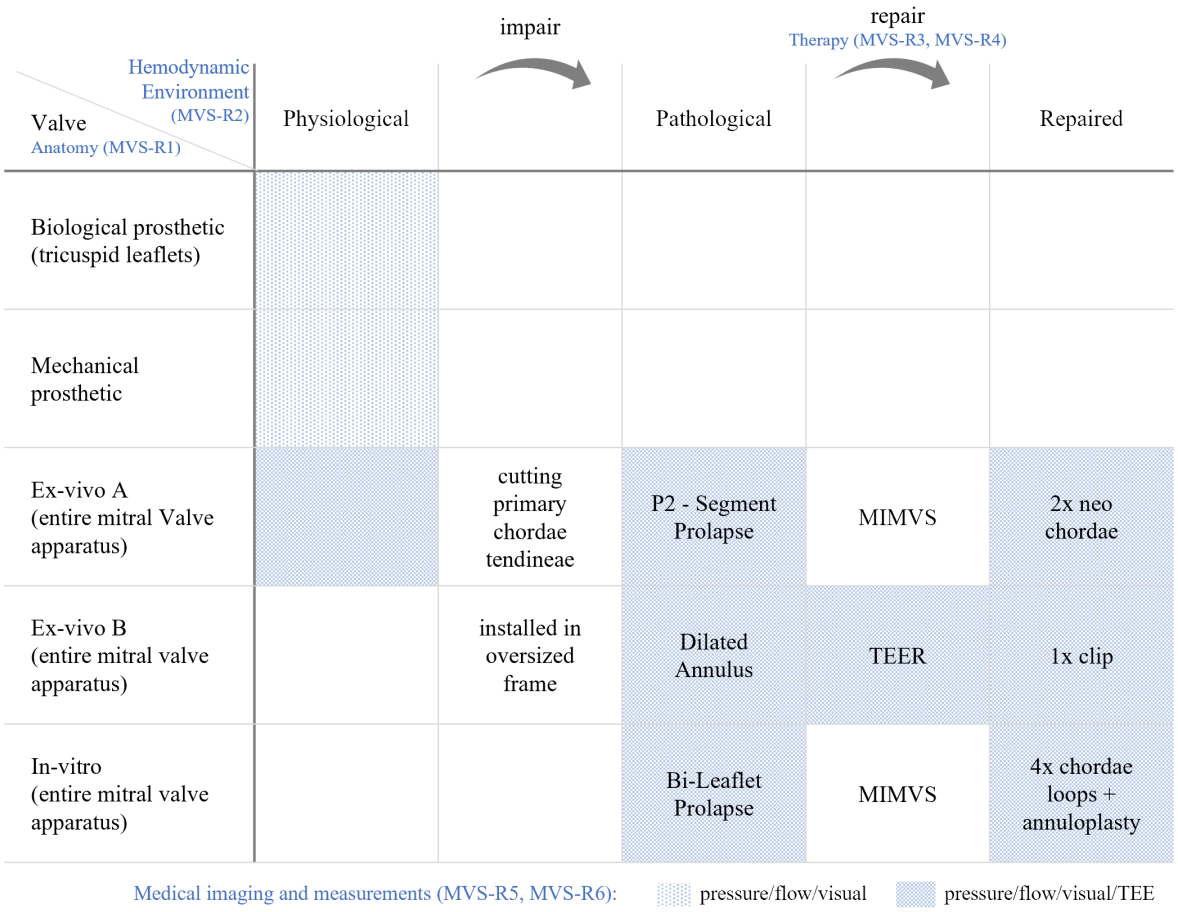

Figure 2.6: Overview of mitral valve experiments. Blue text = requirements to validate. MIMVS = minimally invasive mitral valve surgery, PIV = particle image velocimetry, TEE = transesophageal echocardiography, TEER = transcatheter edge-to-edge repair. This figure was originally published in Karl et al. (2024), adapted and reused under the CC BY 4.0 - Licence.

Prosthetic mitral valves

To validate the hemodynamic environment (MVS-R2), the simplest setting was to install a **Biological prosthetic valve** (T510C31, Medtronic plc, Dublin, Ireland) and afterwards a **Mechanical prosthetic valve** (21 MHPJ-505, Abbott Laboratories, Illinois, USA) in the simulator at 80 bpm, adjust the compliance volume to reach a systolic pressure of roughly 120 mmHg and measure pressure and flow (MVS-R6).

Porcine mitral valves

The next step was to install excised mitral valves from healthy porcine, referred to as Ex-vivo valves A and B. **Ex-vivo valve A**, sewn into an anatomically well-sized elliptical frame (40 mm long and 30 mm wide) was installed in the simulator at 80 bpm. The chordae tensioners were adjusted to facilitate normal leaflet motion, and compliance volume was set to reach a systolic pressure of 120 mmHg to create a realistic hemodynamic environment (MVS-R2). This was the first valve to include the whole anatomy of the mitral valve (MVS-R1). The first step was to perform TEE (MVS-R5) and measurements of pressure and flow

(MVS-R6). To validate for known *in-vivo* conditions of mitral valves in a pathological state, primary chordae tendineae were cut to induce a primary, Carpentier Type II, mitral regurgitation. Subsequently, imaging and measurements were repeated. To prove the feasibility of therapy at the simulator, the left atrium was exchanged by the MIMVS-head, and MIMVS was performed (MVS-R3). After replacing the MIMVS-head with the left atrium again, the measurements were repeated a third time.

Ex-vivo valve B was sewn into an oversized circular frame with a diameter of 50 mm to induce a dilated annulus and therefore a secondary, Carpentier Type I, mitral regurgitation. Installed in the simulator at 80 bpm the chordae tensioners were adjusted to create normal leaflet motion and the compliance volume was set to 40 ml air, which was a value known from the preliminary experiments. The reason for this was, that by adjusting the compliance volume to reach 120 mmHg directly, the systolic pressure of the repaired valve would exceed physiological values. TEE and measurements were conducted. To prove the feasibility of TEER (MVS-R4), a Pascal system (Edwards Lifesciences Corporation, California, USA) was inserted via transseptal access. TEER was performed under TEE and video guidance. Medical imaging and measurements were obtained afterwards.

Patient-specific mitral valves

To show the integration of patient-specific valves, an **In-vitro valve**, cast from silicon after the method introduced by Engelhardt et al. (2019), was installed in the simulator. To enforce the valve a mesh was added to the leaflets, and sutures were added to the chordae tendineae during the casting process. The pathology was a bi-leaflet prolapse, and classified as a primary, Carpentier Type II, mitral regurgitation. After adjusting the chordae tensioner and compliance volume analog to the valves before, medical imaging and pressure and flow measurements were obtained. As done with Ex-vivo valve A, the left atrium was exchanged by the MIMVS-head before MIMVS. The MIMVS consisted of a 20 mm chordae loop (CV-4 needle) at the anterolateral papillary muscles with the four loops attached to the segments A1, A2, A3, and P1 with Cardionyl® 4/0 (Peters Surgical, Boulogne-Billancourt, France). Additionally, an annuloplasty was carried out, implanting a 36 mm Mitral Annuloplasty Memo 4D Ring (LivaNova PLC, London, UK). After surgery, the left atrium was installed again to repeat medical imaging and measurements.

2.2 Quantification of mitral regurgitation

Parts described in this section are submitted for publication (Leister et al., 2024). The text has been rewritten for this thesis.

To evaluate the flow convergence method and meet Objective II, a successful approach involved reproducible and realistic hemodynamics and a second non-invasive imaging technology. A simulator creating a realistic *in-vitro* hemodynamic environment was introduced

in Section 2.1. PIV, as shown by Sonntag et al. (2014), serves as a second non-invasive imaging modality to assess the flow convergence method.

2.2.1 Simulator and regurgitation orifice design

The hemodynamics were generated using the simulator that has been introduced in Section 2.1 and validated in Section 3.1. The simulator's modular design facilitated the incorporation of PIV by modifying the left atrium. For PIV, a laser beam must traverse the left atrium perpendicular to the annulus plane of the mitral valve. This arrangement allows the laser to illuminate particles suspended in the fluid within the left atrium. This was already possible through the atrial window. Additionally, a camera positioned perpendicular to the laser beam was required to capture the illuminated particles across the entire left atrium. To facilitate this, a second window was incorporated into the left atrium, situated on the opposite side of the septum. The entire setup, including the simulator, TEE probe, camera, and light sheet optics is displayed in Figure 2.7. For this setup, the same blood-mimicking fluid as described in Chapter 2.1.3 was used.

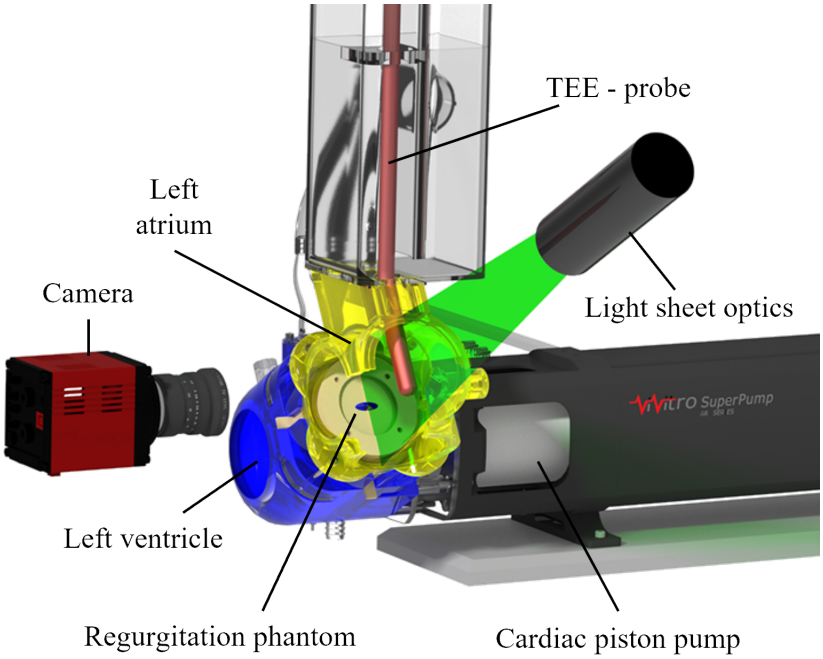

Figure 2.7: Simulator configuration for particle image velocimetry and transesophageal echocardiography. TEE = transesophageal echocardiography.

Regurgitation jets were induced by exchanging the mitral valve by a so-called regurgitation phantom. The regurgitation phantom is a 0.5 mm thick film made out of polyvinylchlorid (PVC), containing a laser-cut orifice. This orifice replicated the orifice of the mitral valve during systole. While the flow convergence method is based on the estimation of a circular orifice, the pathological orifice in humans is rather elliptical or complex (Lancellotti et al., 2010). Therefore, three different orifice shapes were used for this study: a circle, a pointed

oval, and a drop (Figure 2.8). Furthermore, the regurgitation phantoms of each orifice shape were manufactured in three different sizes to replicate different severities of mitral regurgitation. After manufacturing, the dimensions of regurgitation phantom orifices were measured using background-illuminated imaging (Table 2.2).

While the regurgitation phantoms mimic the mitral valve during systole, they are not capable of opening during diastole. Removing the aortic valve from the simulator allowed for filling of the left ventricle during diastole.

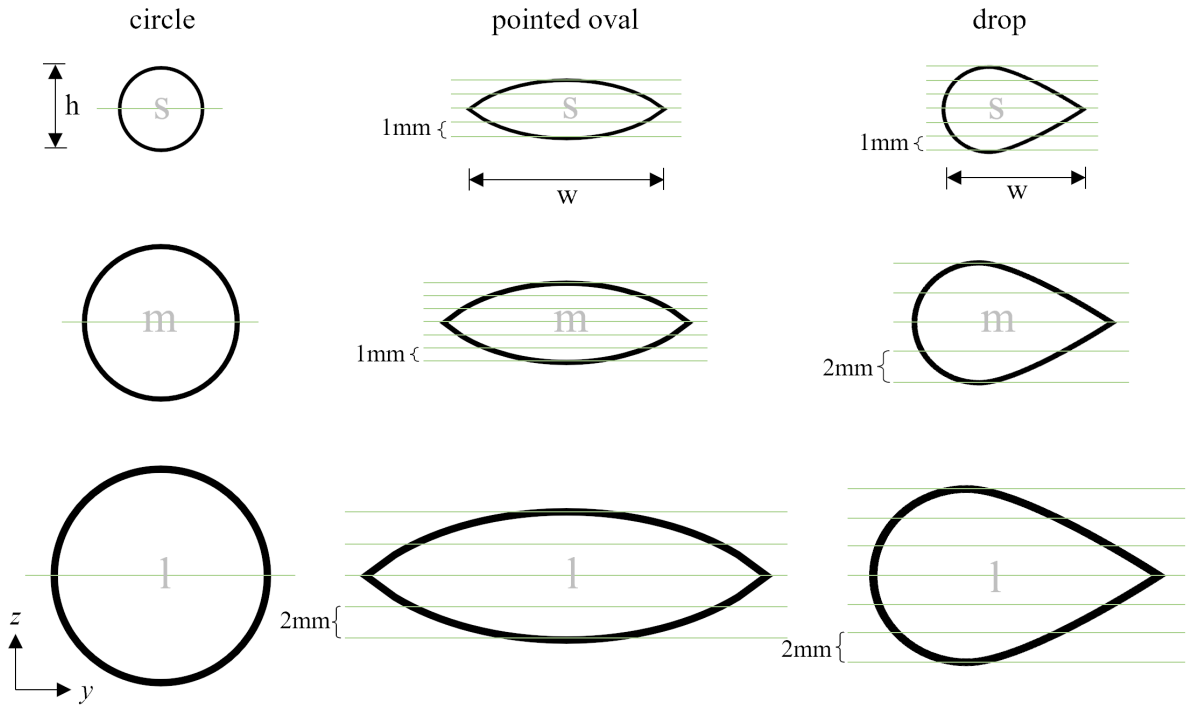

Figure 2.8: Shapes of regurgitation phantom orifices with z-planes (green) where particle image velocimetry measurements were obtained. h = height, l = large, m = middle, s = small, w = width.

Table 2.2: Measured dimensions of the regurgitation phantom orifices.

	circle			pointed oval			drop		
	s	m	l	s	m	l	s	m	l
height [mm]	4.7	8.7	12.2	3.3	4.5	7.3	4.3	6.5	9.0
width [ml]	-	-	-	11.1	14.0	22.9	9.7	13.7	19.8
area [mm^2]	17.1	58.8	116.7	27.0	44.8	115.1	27.1	52.1	108.4

2.2.2 Experiments

The induced regurgitation jets of each regurgitation phantom were quantified by PIV and and the flow convergence method. During these experiments, the "physio-waveform" (Fig-

ure 2.2a) was used with a frequency of 80 bpm. The compliance volume was adjusted for each regurgitation phantom to reach systolic pressures of 120 mmHg inside the left ventricle.

Flow convergence method

The flow convergence method was performed as described in Section 1.3.3. Briefly, the physicians measured the PISA radius in color-doppler mode and the VTI in cw-doppler mode. Residual values such as EROa and regurgitation volume were calculated by the ultrasound machine based on the measured data. The ultrasound systems used by the physicians are displayed in Table 2.3. Each physician was asked to assess the mitral regurgitation of each regurgitation phantom using the flow convergence method as done in the clinical routine.

Table 2.3: Ultrasound configurations to perform the flow convergence method.

Operator	Ultrasound machine	TEE-probe	Company
Physician 1	EPIQ Cvxi	X8-2T	Koninklijke Philips N.V.
Physician 2	EPIQ 7C	X8-2T	Koninklijke Philips N.V.
Physician 3	iE33	X7-2T	Koninklijke Philips N.V.

Particle imaging velocimetry

Obtaining comprehensive quantitative flow information, including velocities and their derivatives, for flows simulating human heart blood flow is challenging. This difficulty arises from the limited optical access and the necessity to adhere to geometrical and functional constraints. Generally, PIV serves as a robust and well-established imaging technique for particle-based flow measurements (Raffel et al., 2018; Adrian and Westerweel, 2011).

The setup used for the 2D2C-PIV experiments is depicted in Figure 2.7. Two atrial windows were utilized to facilitate optical access for both the camera and the laser sheet. In order to analyze the flow, an ILA.PIV.sCMOS camera (with a 16 bit dynamic range and pixel size of 6.5 µm) was combined with a 50 mm Zeiss Makro Planar lens. The achieved magnification was expressed as $M = 0.2$ (yielding a reproduction scale of $s^{xy} = 33.3$ µm/px; field of view size: 85 × 72 mm^2). The illumination was provided by a double-pulsed Quantel Evergreen Nd:YAG laser (with 210 mJ energy and $\lambda = 532$ nm wavelength).

For each geometry and z-plane (Figure 2.8), 1,000 double images were captured at a frequency of 15 Hz, covering various phases of the cardiac cycle. To calculate the regurgitation volume, only positive velocity values at the outlet were used. Using the phantom "drop m" as an example, the step-by-step process for determining the regurgitation volume from the recorded velocity data is explained. For "drop m", five z-planes were defined, resulting in a total of 5,000 raw double images. Each double image was analyzed with the PIV software

PIVview (PIVTEC GmbH, Göttingen, Germany) and saved as an nc-file. This file was loaded into MATLAB for further post-processing. The vector field was rotated by 29° so that the main flow direction aligned with the x-axis. To determine the regurgitation volume, the flow velocity was examined as close as possible to the opening of the phantom. The limiting factors here were light reflections from the phantom, which could lead to an underestimation of the regurgitation volume if the observation point was too close to the opening, and entrained fluid, which could lead to an overestimation if the point was too far from the opening. Figure 2.9 shows a representative instantaneous flow field from "drop m" with the integration boundaries in the y-direction and the x-position of the velocity extraction. This position is approximately 1.1 mm away from the phantom opening. For the determination of the regurgitation volume, only positive values were considered, as these represent the values during systole.

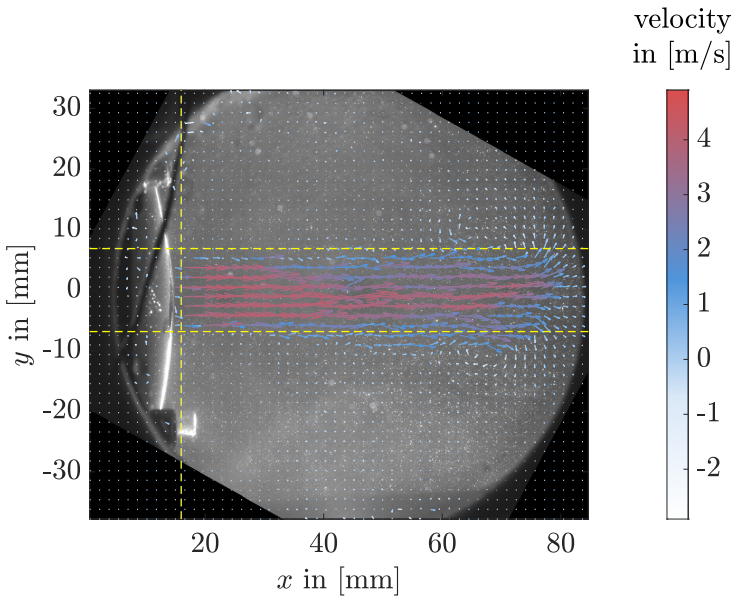

Figure 2.9: Instantaneous flow field for "drop-m" as colored vector plot overlayed with the raw data image. The integration limits and the x-position of the regurgitation volume extraction are indicated with yellow lines.

2.3 Aortic simulator

Parts described in this section are published (Mohl et al., 2024). The text has been rewritten for this thesis.

This section outlines the requirements, materials, and methods for designing and validating an aortic flow-loop in compliance with objective III.

2.3.1 Requirements

While several solutions such as patient-specific aortic phantoms or hemodynamic simulators exist as described in Section 1.4.3, none of them create a realistic environment to train

or plan TEVAR. To solve this problem and consequently meet objective III of this thesis the following requirements for the aortic simulator (AS-R) and aortic phantom have been identified to allow for realistic TEVAR simulation to treat TBAD:

AS-R1 - Integration of entire aortic anatomy: During a TEVAR procedure a pigtail catheter is guided through the true lumen of the entire aorta starting at the arteria iliaca communis and ending at the aortic valve, therefore the simulator should include an aortic phantom comprising the ascending and descending aorta from the aortic root to the arteria iliaca communis. Furthermore, TBAD and TEVAR may affect any aortic branch. Therefore, the inclusion of the aortic branches in the phantom is necessary as well.

AS-R2 - Modelling of aortic features: To allow for comparison of the procedure and procedural or pathological effects, the aortic phantom should realistically replicate dimensions, material properties, and pathology of the patient.

AS-R3 - CTA and DSA compatibility: Before, during, and after the TEVAR procedure the patient is subject to several medical imaging technologies, such as CTA and DSA. To allow for pre-, inter-, and post-interventional analysis of the aortic phantom, the phantom and simulator should be compatible with CTA and DSA scanners, as well as the use of contrast agent.

AS-R4 - Femoral access: The stent-grafts used for TEVAR to treat TBAD enter the human body through femoral access. Consequently, this femoral access needs to be included into the flow-loop respecting anatomical distances.

AS-R5 - Realistic hemodynamics: To train and study the effects of TEVAR on TBAD on a patient-specific aortic phantom, a realistic hemodynamic environment is necessary. Therefore systolic pressures of 120 - 130 mmHg, a pulsatile flow of 4.5 - 5 l/min, and frequencies of 60 - 80 bpm should be achievable.

A solution addressing the specified requirements is presented through the collaborative efforts of Mr. Lukas Mohl within his yet-unpublished thesis, titled "Manufacturing and Evaluation of Patient-Specific 3D-Printed Aortic Arches with Dissection Membranes," and the work presented herein. Mr. Lukas Mohl's work encompasses the manufacturing process (AS-R1, AS-R2) and the evaluation of the aortic phantom. This work encompasses the comprehensive development and assessment of the overarching simulator, including its associated hemodynamic conditions (AS-R4, AS-R5), as well as the compatibility assessment of both the simulator and phantom with medical imaging technologies such as CTA and DSA (AS-R3). Collaborative efforts extended to pressure, flow, DSA, and TEVAR experiments, aimed at evaluating, for instance, the simulator's ability to replicate a realistic hemodynamic environment and the aortic phantom's resilience under pulsatile physiological pressures. The following sections provide insights into Mr. Lukas Mohl's aortic phantom manufacturing process, enhancing the understanding of the overall concept. Subsequently, the design process of the simulator, imaging

modalities, and data acquisition are described. The experiments section outlines the methodologies employed to assess the simulator against the specified requirements.

2.3.2 3D printed patient-specific aortic replicas

The patient-specific aorta phantom was developed, manufactured, and evaluated by Mr. Lukas Mohl.

To allow for personalized training and planning, a patient-specific aortic phantom was manufactured. The initial step was to segment the aorta from a CTA data set of a patient with TBAD (AS-R1, AS-R2). Segmentation was done using the MITK software (German Cancer Research Center, Heidelberg, Germany).

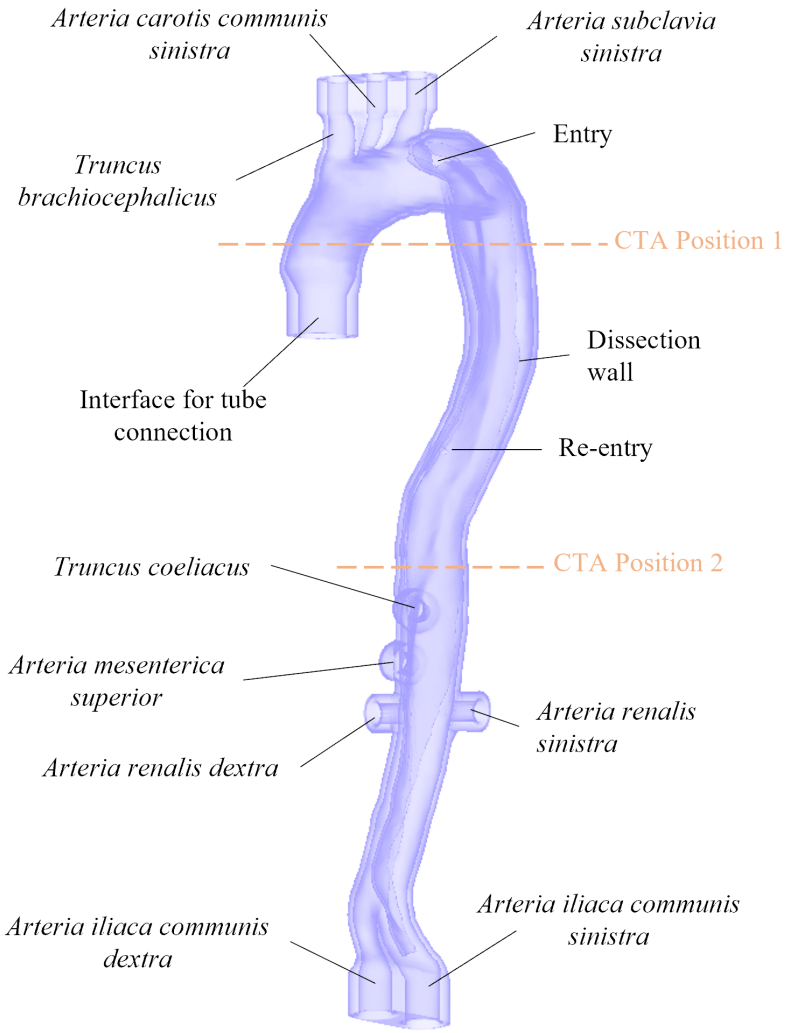

Figure 2.10: Post-processed model of the dissected aorta. Showing all branches in italic letters. Dotted lines indicate axial CTA views displayed in the results. The model shows the interfaces to connect tubes, entry and re-entry of the false lumen, and the dissection wall. CTA = computed tomography angiography. *The figure was generated based on the 3d-model of Mr. Lukas Mohl.*

After segmentation, the model was processed in Blender (software by Blender Foundation, Amsterdam, Netherlands). The aortic wall thickness was adjusted to 2.1 mm and the dissection membrane to 1.1 mm. The model was smoothed and interfaces were added to all aortic entries and exits to allow for the connection of tubes to integrate the aortic phantom into the flow-loop (Figure 2.10). The aortic phantom was then printed out of TangoPlus FLX930 and support material SUP706 B, using an Objet 500 Connex 3 3D printer with multi-jet modeling technology (materials and printer: Stratasys Inc., Rechovot, Israel). TangoPlus was selected because its material properties closely resemble the elastic behavior of an *in-vivo* aorta (AS-R2) (Cloonan et al., 2014; Gallarello et al., 2019). Given the complex and hollow geometry of the aorta, the use of support material was imperative during the printing process. After printing, the support material was washed out and the aortic phantom was installed in a box of acrylic glass and integrated into the flow-loop. The acrylic glass box was filled with water to simulate the extra-vascular pressure.

2.3.3 Flow-loop design

The aortic flow-loop, visible in Figure 2.11 consists of a pump unit, the aortic phantom, femoral access for stent-grafting, reservoir, and tubes to interconnect the parts. The pump unit is comprised of a pulsatile cardiac piston pump, SuperPump, in combination with the viscoelastic impedance adapter (both ViVitro Labs, Inc., Victoria, BC, Canada) introduced in Section 2.1.2 and a self-designed pump head with two 13 mm check valves out of polyvinyl chloride (Van de Lande B.V., Raamsdonksveer, Nederland). The pump head, combined with the check valves, directs the fluid flow from the reservoir to the aortic root of the aortic phantom. Each aortic branch is connected to the reservoir. This setup enables a hemodynamic environment for the aortic phantom and the TEVAR procedure (AS-R5). To allow for measurement of pressure, a luer-lock port was included at each aortic branch. A 24 Fr DrySeal Flex Introducer Sheath (W. L. Gore & Associates, Inc, Newark, Delaware, United States) was advanced into the arteria iliaca communis dextra in order to allow for stent-grafting (AS-R4). The DrySeal access was only installed during stent-grafting, but not during CTA scans or flow and pressure measurements.

2.3.4 Sensors

The data acquisition for the aortic simulator covers pressure and flow measurements as well as the medical imaging modalities ultrasound, CTA, and DSA. Figure 2.12 provides an overview of all acquired and processed data.

Flow

The flow data was recorded with the Sonoflow C^3 software (hard- and software by Sonotec GmbH, Halle (Saale), Germany) and exported in an HTML file. A Matlab script was written to process and visualize data. The data was recorded for 30 s with a sampling rate of 60 Hz.

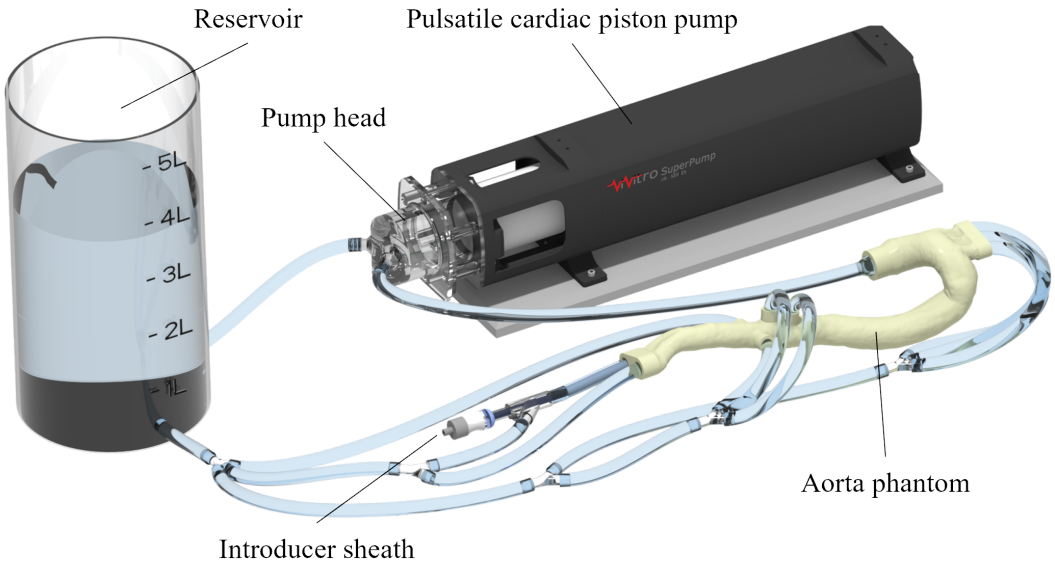

Figure 2.11: The aortic flow-loop consists of a pump unit, aorta phantom, an introducer sheath used for stent-grafting, a reservoir, and tubes to interconnect all parts. This figure was originally published in Mohl et al. (2024), adapted and reused under the CC BY 4.0 - Licence.

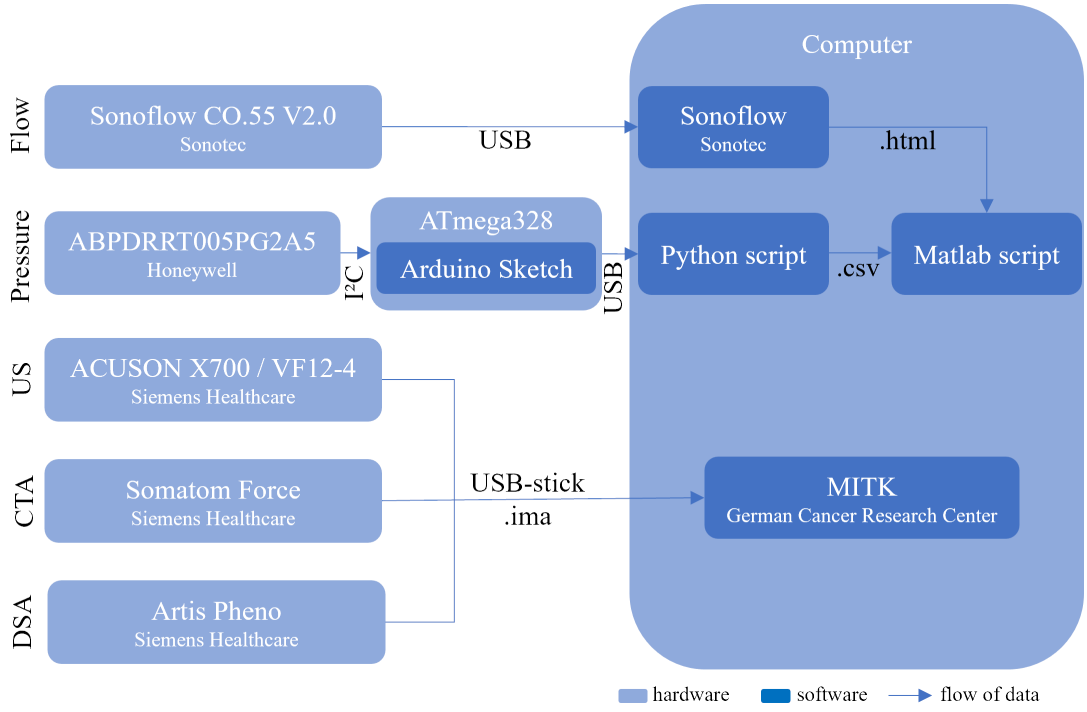

Figure 2.12: Data flow of the aortic simulator. .csv = comma-separated values - text file, CT = computed tomography, DSA = digital subtraction angiography, .ima = image file, I^2C = inter-integrated circuit - protocol to transfer data, US = ultrasound, USB = universal serial bus - physical interface and protocol to transfer data.

The mean flow was calculated over 30 s and divided by the frequency of the pump to calculate the stroke volume. To ensure the comparability between experiments the flow data was normalized by equalizing the flow leaving the pump.

Pressure

Similar to the pressure measured in the MV simulator, the pressure of the aortic root was measured with ABPDRRT005PG2A5 pressure sensors (Honeywell International Inc., North Carolina, US). The sensors are connected to an Arduino clone (AT-mega328 Microcontroller Board by AZ-Delivery Vertriebs GmbH, Germany) via inter-integrated circuit (I^2C). An Arduino sketch converts the data into mmHg and sends them via USB to the computer. A script in Python language on the computer allows for live monitoring and recording of the pressure data. Via a CSV file, the recordings are transferred to a Matlab script, in which the data is processed and visualized.

Computed tomography angiography and digital subtraction angiography

CTA scans were conducted using a Somatom Force scanner (Siemens Healthcare GmbH, Erlangen, Germany). DSA scans were performed employing an Artis Pheno robotic imaging system (Siemens Healthcare GmbH, Erlangen, Germany). The exported images were transferred to a computer via a USB hard drive. The used file format is ima by Siemens and is compatible with most DICOM readers. For this study, the data was analyzed using the MITK software (German Cancer Research Center, Heidelberg, Germany). MITK facilitates navigation through the coronal, axial, and sagital slices of the data sets. Moreover, it allows for window adjustment. In most instances, a narrow window with a width of 360 HU and a level of 220 HU was employed. This corresponds to a typical window setting for soft tissue.

2.3.5 Experiments

To validate the flow-loop and the aortic phantom, different medical imaging modalities and flow and pressure measurements were performed before, during, and after TEVAR. During all experiments, the pump was set to a stroke volume of 70 ml and a frequency of 80 bpm. blood-mimicking fluid was used as described in Section 2.1.3. Ethical approval was obtained from the Ethics Committee of the Faculty of Medicine of Ruprecht-Karls-University Heidelberg, Germany (S-158/2015).

Flow, pressure, and computed tomography angiography

Firstly, the flow and pressure at the aortic root were measured to evaluate the hemodynamic environment the simulator provides (AS-R5). Subsequently, the flow of each aortic branch was measured to allow for pre- and post-TEVAR comparison. The aortic branches include the truncus brachiocephalicus, arteria carotis communis sinistra, arteria subclavia sinistra, truncus coeliacus, arteria mesenterica superior, arteria renalis sinistra, arteria renalis dextra, arteria iliaca communis sinistra, and arteria iliaca communis dextra. The Flow was measured with Sonoflow CO.55 V2.0 ultrasound probes (Sonotec GmbH, Halle (Saale), Germany).

To assess the aorta and the TEVAR outcome pre- and postintervention CTA scans are obtained in clinical routine (AS-R3). To evaluate the compatibility of the flow-loop with CT

scanners, X-ray radiation, and contrast agent, CTA scans were performed with a Somatom Force scanner (Siemens Healthcare GmbH, Erlangen, Germany) before and after the TEVAR experiment. Possible issues may include challenging positioning of the flow-loop in the CT scanner, artifacts caused by the aortic phantom, or difficulty distinguishing between blood-mimicking fluid, aortic phantom, and extravascular medium. Furthermore, effects between the contrast agent and the flow-loop could disrupt the simulator, or other unforeseen problems could occur.

In a first attempt, the aortic phantom was placed in the CT scanner without a connection to the flow-loop, with Laponite-XLG XR (BYK-Chemie GmbH, Wesel, Germany) as an extravascular medium, and without adding contrast agent. In a second attempt contrast agent is added to increase the visibility of the blood-mimicking fluid inside the phantom. An iodine concentration of 6 mg/ml was provided by adding 0.67 % by volume of ACCUPAQUE^{TM} 300 (GE Healthcare Buchler GmbH & Co.KG, Braunschweig, Germany) to the blood-mimicking fluid. In a third experiment, the aortic phantom was connected to the flow-loop to increase the distribution of contrast agent. To ensure a fit in the CT scanner and to ease the setup, only the aortic root and the arteriae iliacae communes were connected to the flow-loop, but not the remaining aortic branches. For the fourth experiment, the Laponite was exchanged by water to prevent the encapsulation of air.

Thoracic endovascular repair

To validate the system with regard to cardiovascular interventions, stent-grafting was performed. For this, the introducer sheath, as described in Section 2.3.3, was installed in the arteria iliaca communis dextra. The aortic phantom was placed on the operating table. The flow-loop was degassed and positioned in compliance with the interventional angiography system. A pigtail catheter was introduced via the introducer sheath into the true lumen. DSA was performed multiple times, by manually adding contrast agent, to guide the catheter through the true lumen into the aorta ascendens. The soft wire within the pigtail catheter was replaced by a stiff wire before retracting the pigtail catheter in order to leave the stiff wire solely within the aorta. Subsequently, the stent-graft (E-vita thoracic 3G, with a 230 mm length and a 33 mm diameter from JOTEC GmbH, Hechingen, Germany) was guided by the stiff wire through the true lumen towards its final position covering the proximal entry of the false lumen. DSA was performed again to ensure proper positioning. Then, the stent-graft was carefully released. Finally, DSA was repeated via a new pigtail catheter to evaluate the sealing of the proximal entry.

3 Results

This chapter comprises the results of the evaluation of the mitral valve simulator in Section 3.1, the different methods to assess mitral regurgitation in Section 3.2, and the aortic simulator in Section 2.3.

3.1 Evaluation of the mitral valve simulator

The following section covers the results of the experiments executed on the mitral valve simulator and described in Section 2.1. Aiming to validate the simulator two prosthetic valves, two porcine valves, and one patient-specific silicone valve were installed. MIMVS and TEER were performed. Pressure and flow were measured and TEE was obtained.

3.1.1 Providing a realistic hemodynamic environment

To evaluate the hemodynamic environment (MVS-R2) a biological and a mechanical prosthetic mitral valve were observed after another in the simulator.

Biological prosthetic mitral valve

The biological prosthetic mitral valve was installed in the simulator (Figure 3.1a). The settings of the pump, and the parameters measured and calculated are displayed in Table 3.1. Pressure and flow are visualized in Figure 3.1b,c. These parameters reflect a physiological state (MVS-R2) with known *in-vivo* parameters of 118 mmHg systolic blood pressure and 4.88 l/min cardiac output.

Table 3.1: Biological prosthetic valve: selected set, measured, and calculated values. CV = compliance volume, HR = heart rate, MR = mitral regurgitation, RF = regurgitation fraction, RVol = regurgitation volume, SBP = systolic blood pressure, SV_{Pump} = stroke volume of pump, SV_{LV} = stroke volume of LV = left ventricle.

Pump settings			Measurements			Calculations		
HR	SV_{Pump}	CV	SBP	SV_{LV}	CO	RVol	RF	MR
[bpm]	[ml]	[ml]	[mmHg]	[ml]	[l/min]	[ml]	[%]	Grade
80	70	130	118	61	4.88	3	5	0

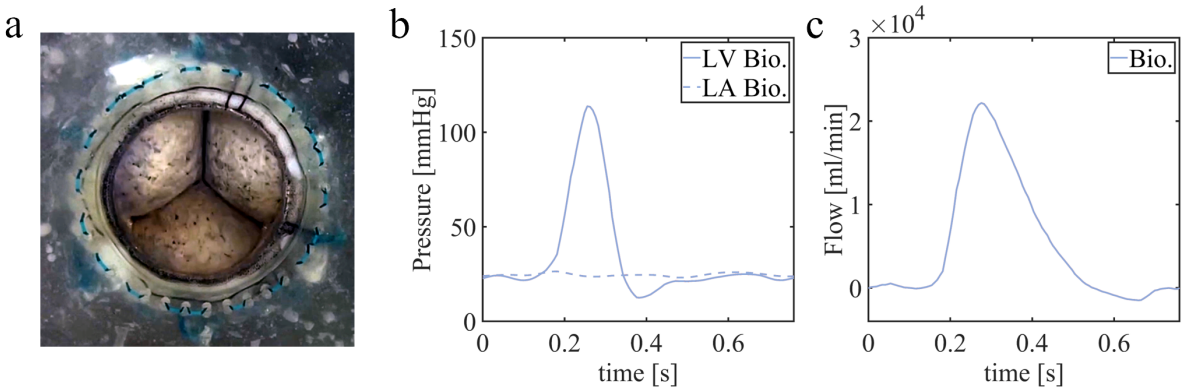

Figure 3.1: Biological prosthetic valve installed in the simulator (a), with corresponding pressure (b), and flow (c) over one cardiac cycle. Bio. = biological prosthetic valve, LA = left atrium, LV = left ventricle. This figure was originally published in Karl et al. (2024), adapted and reused under the CC BY 4.0 - Licence.

Mechanical prosthetic mitral valve

Analog to the biological, the mechanical prosthetic valve was installed in the simulator (Figure 3.2a) with the pump settings and recordings visible in Table 3.2 and pressure and flow visualized in Figure 3.2b,c. These measurements and calculations resemble a physiological state (MVS-R2) with known *in-vivo* parameters of 120 mmHg systolic blood pressure and 4.9 l/min cardiac output.

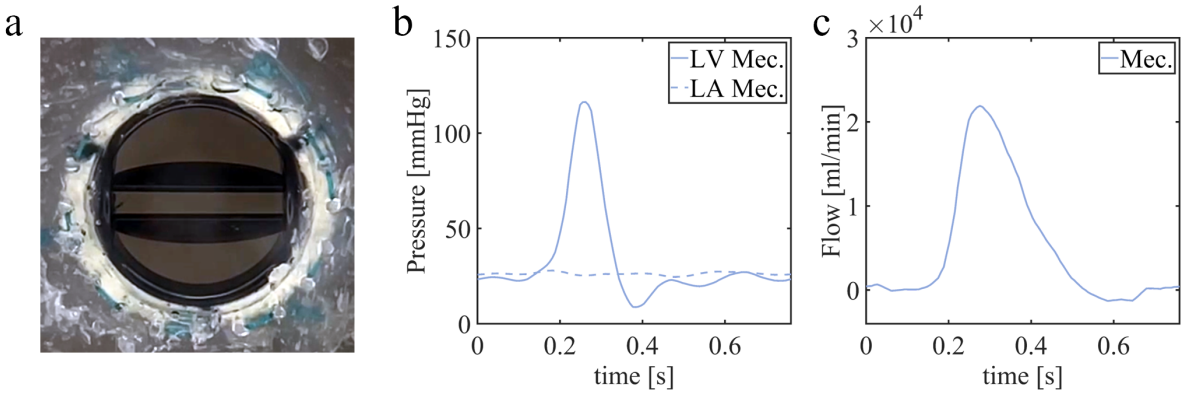

Figure 3.2: Mechanical prosthetic valve installed in the simulator (a), with corresponding pressure (b), and flow (c) over one cardiac cycle. Mec. = mechanical prosthetic valve, LA = left atrium, LV = left ventricle. This figure was originally published in Karl et al. (2024), adapted and reused under the CC BY 4.0 - Licence.

Table 3.2: Mechanical prosthetic valve: selected set, measured, and calculated values. CV = compliance volume, HR = heart rate, MR = mitral regurgitation, RF = regurgitation fraction, RVol = regurgitation volume, SBP = systolic blood pressure, SV_{Pump} = stroke volume of pump, SV_{LV} = stroke volume of LV = left ventricle.

Pump settings			Measurements			Calculations		
HR	SV_{Pump}	CV	SBP	SV_{LV}	CO	RVol	RF	MR
[bpm]	[ml]	[ml]	[mmHg]	[ml]	[l/min]	[ml]	[%]	Grade
80	70	130	119	61	4.9	4	6	0

3.1.2 Integrating the entire mitral valve apparatus

The integration of the entire mitral valve anatomy (MVS-R1) in a hemodynamic environment (MVS-R2) was evaluated by using two excised porcine valves (Ev-vivo A and B). Furthermore, Ex-vivo valves A and B were repaired by MIMVS (MVS-R3) and TEER (MVS-R4), respectively.

Ex-vivo valve A

Ex-vivo valve A, incorporating the entire valve anatomy (MVS-R1), was installed in a healthy physiological state in the simulator as seen in Figure 3.3a, with the pump settings, measurements, and calculated values displayed in Table 3.3, resulting in a physiological behavior (MVS-R2) with a systolic blood pressure of 120 mmHg and a cardiac output of 4.55 l/min. Primary chordae tendineae were cut to impair the valve and induce a chordae rupture pathology, which is visible in Figure 3.3b, and caused a regurgitation jet clearly visible in 3D-color-doppler ultrasound (Figure 3.3c). Impairing the valve resulted in an increase of mitral regurgitation from grade 0 to grade 2 and a regurgitation fraction of 35 %. After evaluation, the left atrium was replaced by the MIMVS-surgery head and a cardiac surgeon (Figure 3.4), with six years experience in cardiac surgery and around 85 assisted MIMVSs, performed MIMVS including neo-chordae insertion. After repair (Figure 3.3d) the left atrium was replaced by the MIMVS-head, and measurements and TEE were obtained again. TEE was performed by a cardio-anesthetist with the experience of two years in cardio-anesthesia and 25 MIMVS. Flow and pressure of Ex-vivo valve A are visualized in Figure 3.5. MIMVS restored the mitral valve to be competent again with a systolic blood pressure of 117 mmHg, cardiac output = 4.67 l/min, and a mitral regurgitation severity of grade 0.

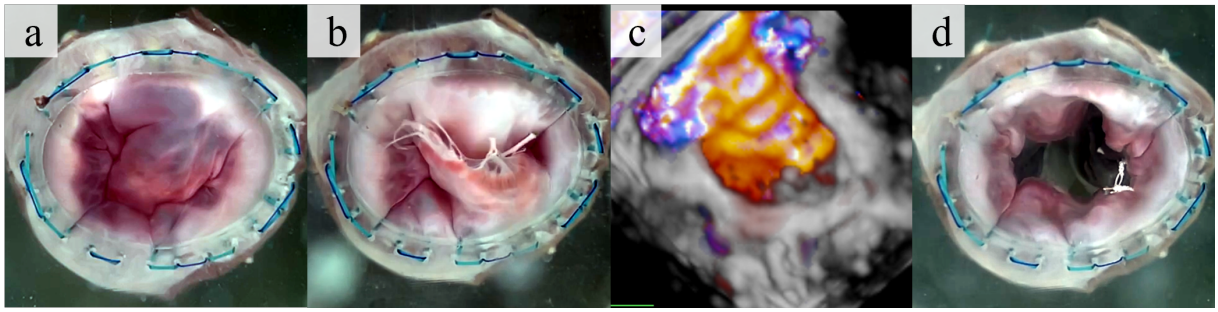

Figure 3.3: Ex-vivo valve A in healthy state (a), after inducing chordae rupture pathological condition (b), displaying a regurgitation jet in 3D color-doppler (c) and after performing minimally invasive mitral valve surgery in repaired condition (d). This figure was originally published in Karl et al. (2024), adapted and reused under the CC BY 4.0 - Licence.

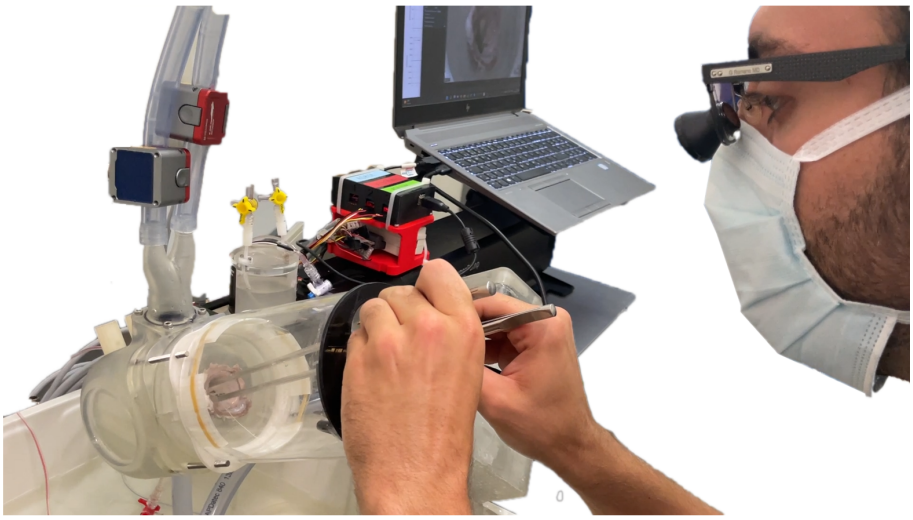

Figure 3.4: Cardiac surgeon performing minimally invasive mitral valve surgery at the simulator with the minimally invasive mitral valve surgery head installed instead of the left atrium. This figure was originally published in Karl et al. (2024), adapted and reused under the CC BY 4.0 - Licence.

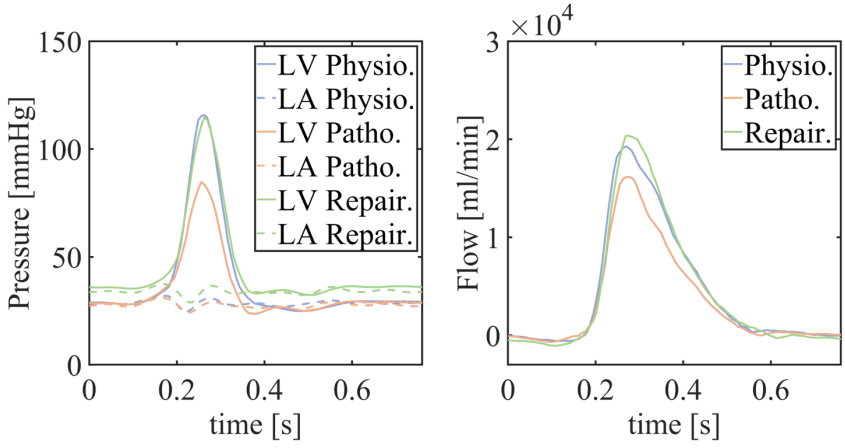

Figure 3.5: Ex-vivo valve A: Pressure and flow over one cardiac cycle in pathological and repaired condition. LA = left atrium, LV = left ventricle, Patho. = pathological, Physio. = physiological, Repair. = repaired. This figure was originally published in Karl et al. (2024), adapted and reused under the CC BY 4.0 - Licence.

Table 3.3: Ex-vivo valve A in a physiological, pathological, and repaired state with selected set, measured, and calculated values. CV = compliance volume, HR = heart rate, MR = mitral regurgitation, RF = regurgitation fraction, RVol = regurgitation volume, SBP = systolic blood pressure, SV_{Pump} = stroke volume of pump, SV_{LV} = stroke volume of LV = left ventricle.

	Pump settings			Measurements			Calculations		
Valve condition	HR [bpm]	SV_{Pump} [ml]	CV [ml]	SBP [mmHg]	SV_{LV} [ml]	CO [l/min]	RVol [ml]	RF [%]	MR Grade
physiological	80	70	100	120	57	4.55	9	14	0
pathological	80	70	100	85	44	3.49	24	35	2
repaired	80	70	100	117	58	4.67	8	12	0

Ex-vivo valve B

Ex-vivo valve B, which was sewed into an oversized frame to induce annulus dilatation, was installed in the simulator as visible in Figure 3.6a. After medical imaging and measuring flow and pressure, the valve was segmented and visualized after Lichtenberg et al. (2020) in 3D and 2D-unfolded view during systole and diastole (Figure 3.7), showing an enlarged annulus. The mitral regurgitation of the pathological mitral valve corresponds to a severity of grade 2 with a regurgitation fraction of 35 %. TEER was performed by two cardiologists with ten and 16 years of experience in cardiology and around 300 TEERs each. While the more experienced cardiologist was steering the TEER device, the other was guiding him by using TEE. Additional guidance was supplied by live video vision. The repair was performed by inserting the steerable catheter and the implant catheter through the guide sheath into the left atrium. After aligning the clip perpendicular to the annulus plane and in the center of the jet, visible in TEE color-Doppler. The clip was then advanced through the mitral valve into the left ventricle, and the paddles were opened (Figure 3.6b,c). After verifying the correct position first the anterior leaflet (A2) and then the posterior leaflet (P2) were grasped (Figure 3.6d). Measurements were obtained again and are visualized in Figure 3.9. An overview of set, measured, and calculated values is given in Table 3.4, showing that the mitral regurgitation could be reduced from grade 2 to grade 1 with a remaining regurgitation volume of 15 ml and regurgitation fraction of 22 %.

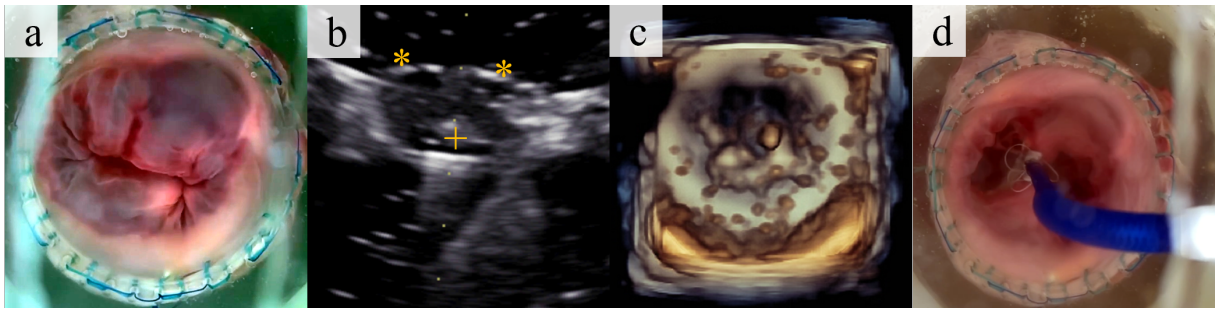

Figure 3.6: Ex-vivo valve B with dilated annulus pathology (a) and after transcatheter edge-to-edge repair in ultrasound B-mode (b), ultrasound 3D-view (c), and visual (d).* = leaflets, + = clip. This figure was originally published in Karl et al. (2024), adapted and reused under the CC BY 4.0 - Licence.

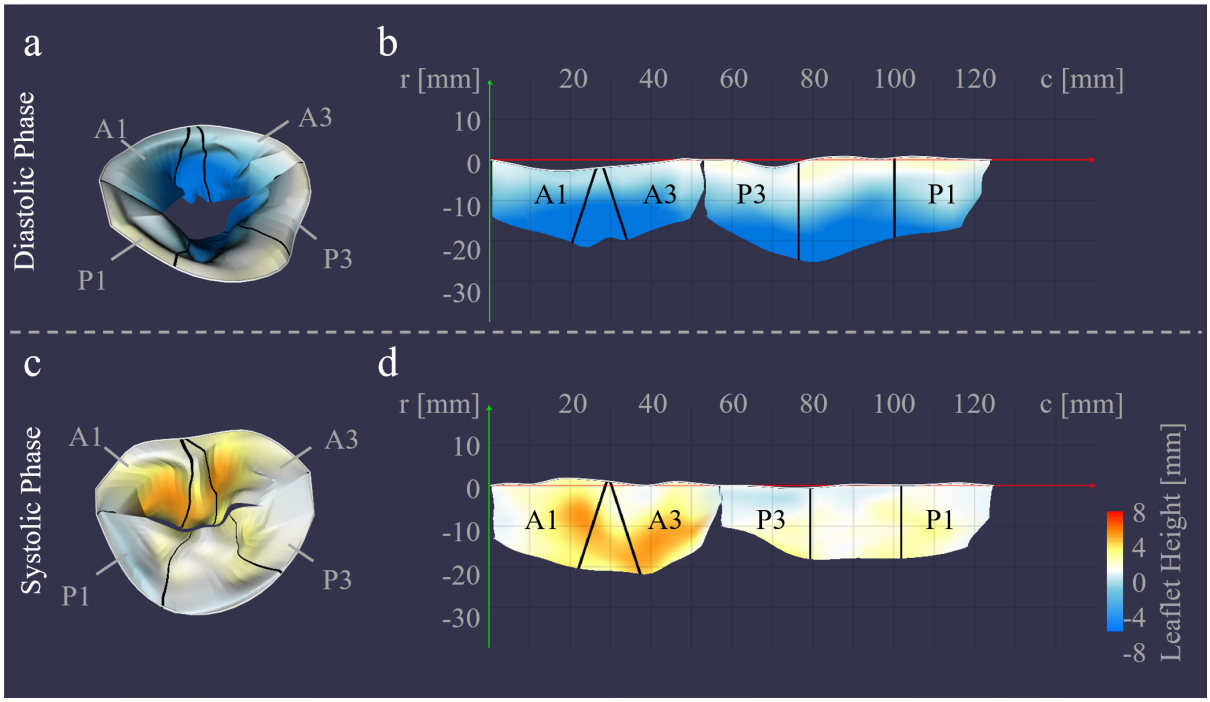

Figure 3.7: Ex-vivo valve B segmented in 3D (a) and unfolded 2D view (b) during diastole and in 3D (c) and unfolded 2D view (d) during systole. A1 - A3 = anterior leaflet segments, c = annulus circumference, P1 - P3 = posterior leaflet segments, r = radial distance to the annulus. This figure was originally published in Karl et al. (2024), adapted and reused under the CC BY 4.0 - Licence.

Figure 3.8: Cardiologists performing transcatheter edge-to-edge repair with one cardiologist (front) steering the device and one (back) guiding by using transesophageal echocardiography. This figure was originally published in Karl et al. (2024), adapted and reused under the CC BY 4.0 - Licence.

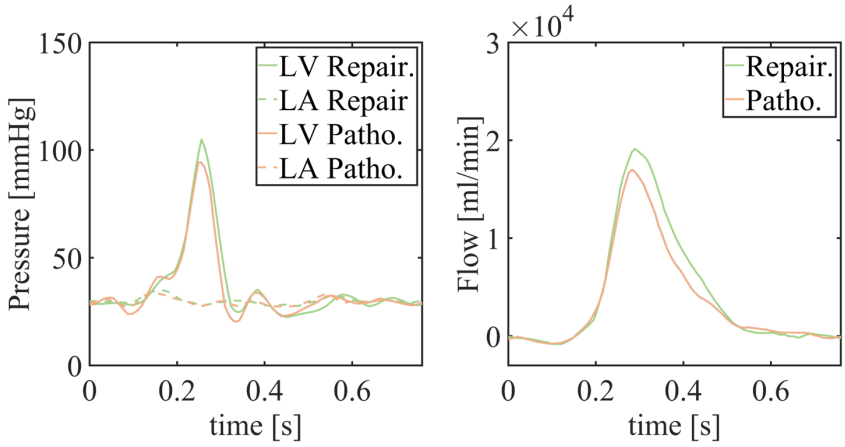

Figure 3.9: Ex-vivo valve B: Pressure and flow over one cardiac cycle in pathological and repaired condition. LA = left atrium, LV = left ventricle, Patho. = pathological, Repair. = repaired. This figure was originally published in Karl et al. (2024), adapted and reused under the CC BY 4.0 - Licence.

Table 3.4: Ex-vivo valve B in pathological and repaired state with selected set, measured, and calculated values. CV = compliance volume, HR = heart rate, MR = mitral regurgitation, RF = regurgitation fraction, RVol = regurgitation volume, SBP = systolic blood pressure, SV_{Pump} = stroke volume of pump, SV_{LV} = stroke volume of LV = left ventricle.

	Pump settings			Measurements			Calculations		
Valve	HR	SV_{Pump}	CV	SBP	SV_{LV}	CO	RVol	RF	MR
condition	[bpm]	[ml]	[ml]	[mmHg]	[ml]	[l/min]	[ml]	[%]	Grade
pathological	80	70	40	99	45	3.56	24	35	2
repaired	80	70	40	106	54	4.3	15	22	1

3.1.3 Individualizing with patient-specific mitral valves

One future goal is personalized planning of mitral valve repair, therefore the next logical step was to include a patient-specific mitral valve. The mitral valve had a bi-leaflet pathology and was manufactured out of mesh-enforced silicone. Installed in the simulator (Figure 3.10a) the patient-specific valve was assessed by TEE (Figure 3.10b,c) and pressure and flow were measured (Figure 3.11 and Table 3.5), showing a clear regurgitation jet and a regurgitation volume of 32 ml, respectively. Analog to the Ex-vivo valve A the left atrium was replaced by the MIMVS-head and the cardiac surgeon repaired the mitral valve by MIMVS. The MIMVS consisted of an annuloplasty and four chordae loops at the segments A1, A2, A3, and P1. The MIMVS-head was replaced by the left atrium again, and measurements and medical imaging were repeated. The MIMVS reduced the mitral regurgitation grade from 2/3 to 1 and the regurgitation fraction from 47 to 32 %.

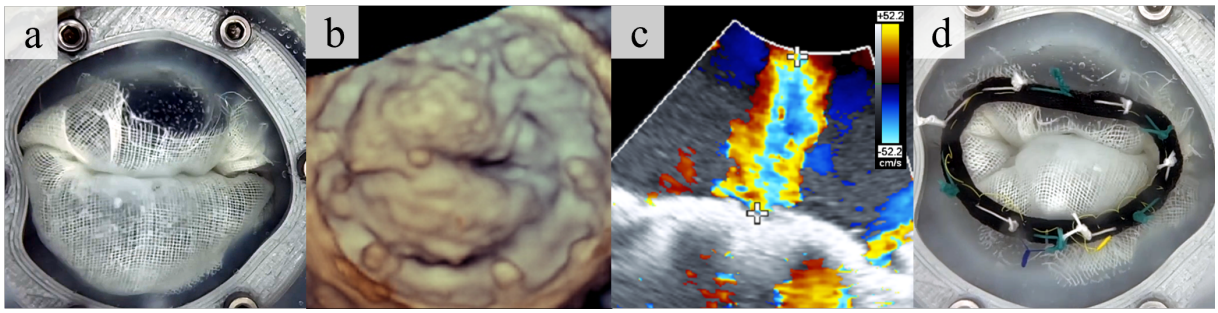

Figure 3.10: In-vitro valve with bi-leaflet pathology (a) in 3D-ultrasound view (b), with a clear regurgitation jet in 2D-color-doppler mode (c) and after minimally invasive mitral valve surgery. ++ = regurgitation jet. This figure was originally published in Karl et al. (2024), adapted and reused under the CC BY 4.0 - Licence.

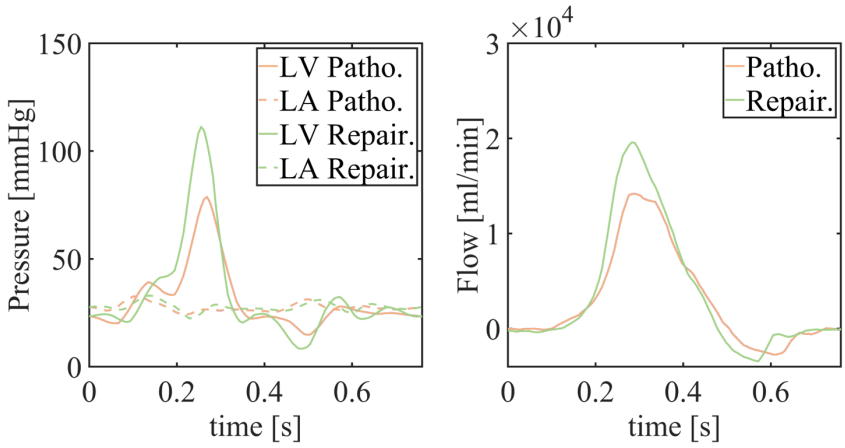

Figure 3.11: In-vitro valve: Pressure and flow over one cardiac cycle in pathological and repaired condition. LA = left atrium, LV = left ventricle, Patho. = pathological, Repair. = repaired. This figure was originally published in Karl et al. (2024), adapted and reused under the CC BY 4.0 - Licence.

Table 3.5: In-vitro valve in a pathological and repaired state with selected set, measured, and calculated values. CV = compliance volume, HR = heart rate, MR = mitral regurgitation, RF = regurgitation fraction, RVol = regurgitation volume, SBP = systolic blood pressure, SV_{Pump} = stroke volume of pump, SV_{LV} = stroke volume of LV = left ventricle.

	Pump settings			Measurements			Calculations		
Valve condition	HR [bpm]	SV_{Pump} [ml]	CV [ml]	SBP [mmHg]	SV_{LV} [ml]	CO [l/min]	RVol [ml]	RF [%]	MR Grade
pathological	80	70	0	79	37	2.98	32	47	2, 3
repaired	80	70	0	115	48	3.83	22	32	1

3.2 Evaluation of different methods to assess mitral regurgitation

To quantitatively determine the accuracy of the flow convergence method, nine regurgitation phantoms were installed in the simulator. The simulator was adjusted to a frequency of 80 bpm and a ventricular pressure of 120 mmHg. The mitral regurgitation induced by the regurgitation phantoms was quantitatively assessed with PIV and the flow convergence

method by echocardiography. Echocardiography was performed by three experienced physicians. PIV and the flow convergence method were compared to assess the accuracy of the flow convergence method.

3.2.1 Flow convergence method

In the first step the PISA radius was measured in color-doppler mode as visible in Figure 3.12. The ultrasound machine calculated the flow rate out of the PISA radius and the set aliasing speed. The next step was to change to cw-doppler-mode as visible in Figure 3.13. The VTI, maximum speed, EROa, and regurgitation volume were calculated. This was repeated by all three physicians and for each regurgitation phantom. All adjusted, measured, and calculated values can be found in Table 3.6.

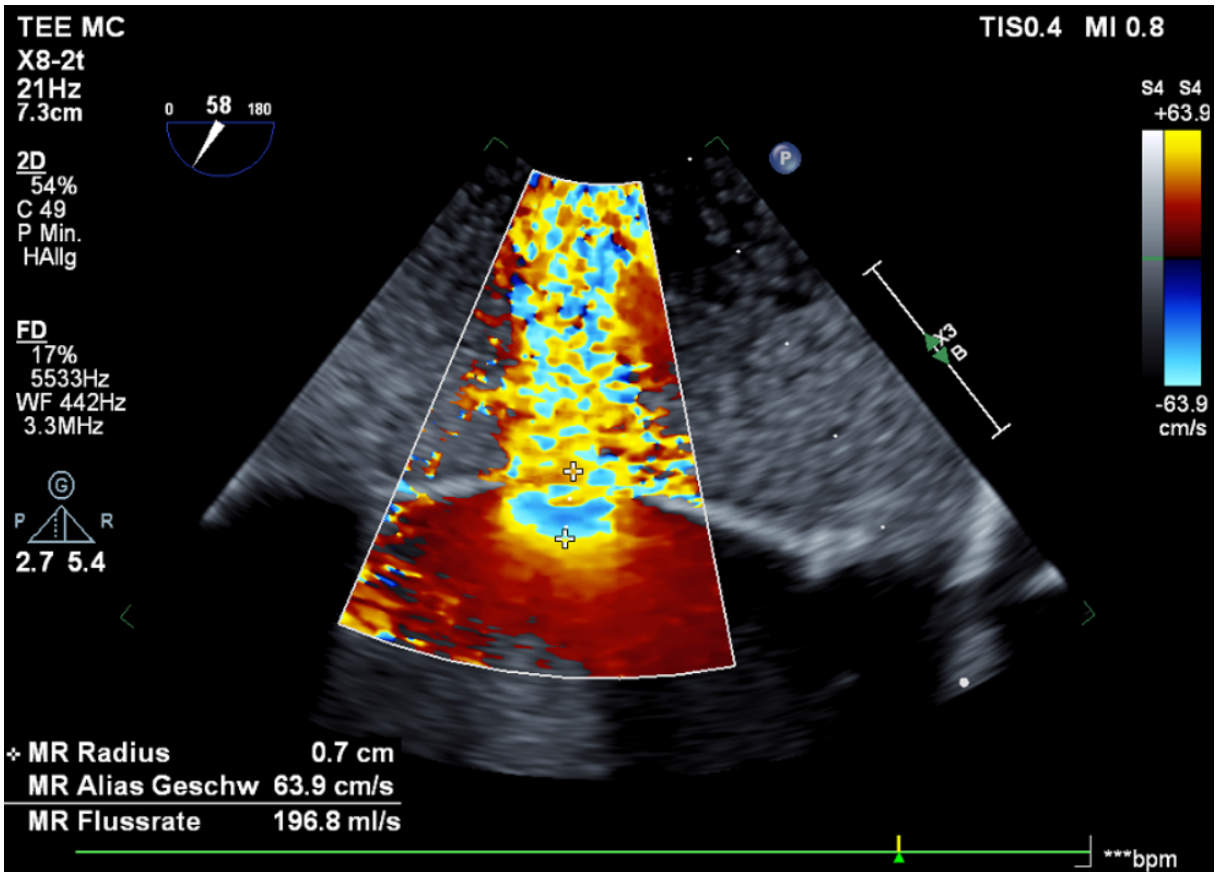

Figure 3.12: Measuring the PISA-radius in the color-doppler mode for pointed oval l.The PISA radius (proximal isovelocity surface area) is measured between the "+ +". A regurgitation flow of 196.8 ml/s is calculated by the ultrasound machine with the measured PISA radius of 0.7 cm and a aliasing speed of 63.9 cm/s.

3.2.2 Particle image velocimetry

The PIV technique allows for direct measurement of the regurgitation jet and is therefore not dependent on auxiliary models like the PISA radius. Figure 3.14 illustrates the phase-averaged velocity distribution at the orifice with a diameter of d = 13 mm (*circle l*). The

Table 3.6: Ultrasound Measurements and corresponding PIV measurement. US = Ultrasound, TEE = Transesophageal echocardiography, MROP = Mitral regurgitation orifice phantom, Freq. = Frequency, V_a = Aliasing velocity, RFlow = Regurgitation flow, V_{max} = Maximal velocity, EROa = Effective regurgitation orifice area, VTI = Velocity time integral, RVol = Regurgitation volume, PIV = Particle image velocimetry.

Physician	US-system	TEE-Probe	MROP	Freq. [Hz]	V_a [cm/s]	Radius [cm]	RFlow [ml/s]	V_{max} [cm/s]	EROa [cm^2]	VTI [cm]	RVol [ml]	$RVol_{PIV}$ [ml]
1	EPIQ Cvxi	X8-2T	circle s	23	38.5	0.4	38.9	500	0.08	66.2	5	4.6
1	EPIQ Cvxi	X8-2T	circle m	22	38.5	0.8	154.8	360	0.43	44.9	19	20.0
1	EPIQ Cvxi	X8-2T	circle l	19	38.5	0.9	196.0	334	0.59	40.0	24	35.1
1	EPIQ Cvxi	X8-2T	pointed oval s	19	38.5	0.5	60.4	399	0.15	50.7	8	9.1
1	EPIQ Cvxi	X8-2T	pointed oval m	22	38.5	0.5	60.4	340	0.18	49.0	9	15.2
1	EPIQ Cvxi	X8-2T	pointed oval l	22	38.5	0.9	196.0	362	0.54	53.5	29	44.9
1	EPIQ Cvxi	X8-2T	drop s	34	38.5	0.4	38.9	369	0.11	50.2	6	10.0
1	EPIQ Cvxi	X8-2T	drop m	24	38.5	0.6	87.0	366	0.24	47.5	11	18.1
1	EPIQ Cvxi	X8-2T	drop l	21	63.9	0.7	196.8	365	0.54	53.7	29	35.6
2	EPIQ 7C	X8-2T	circle s	17	42.8	0.4	43.2	447	0.10	68.9	7	4.6
2	EPIQ 7C	X8-2T	circle m	18	47.0	0.6	106.2	461	0.23	72.5	17	20.0
2	EPIQ 7C	X8-2T	circle l	17	47.5	0.7	146.3	689	0.21	106.0	22	35.1
2	EPIQ 7C	X8-2T	pointed oval s	17	12.1	0.7	37.3	413	0.09	56.3	5	9.1
2	EPIQ 7C	X8-2T	pointed oval m	22	46.2	0.5	72.5	343	0.21	47.5	10	15.2
2	EPIQ 7C	X8-2T	pointed oval l	15	41.5	0.8	166.8	451	0.37	67.2	25	44.9
2	EPIQ 7C	X8-2T	drop s	20	46.2	0.5	72.5	354	0.20	55.7	11	10.0
2	EPIQ 7C	X8-2T	drop m	18	43.4	0.6	98.1	372	0.26	54.1	14	18.1
2	EPIQ 7C	X8-2T	drop l	22	47.2	0.7	145.4	381	0.38	65.9	25	35.6
3	iE33	X7-2t	circle s	16	31.2	0.5	49.0	384	0.13	50.1	6	4.6
3	iE33	X7-2t	circle m	20	31.2	0.7	96.0	394	0.24	58.1	14	20.0
3	iE33	X7-2t	circle l	17	31.2	0.8	125.4	336	0.37	49.2	18	35.1
3	iE33	X7-2t	pointed oval s	19	31.2	0.5	49.0	286	0.17	40.7	7	9.1
3	iE33	X7-2t	pointed oval m	20	31.2	0.7	96.0	294	0.33	36.1	12	15.2
3	iE33	X7-2t	pointed oval l	19	31.2	0.7	96.0	279	0.34	33.0	11	44.9
3	iE33	X7-2t	drop s	24	31.2	0.6	70.5	270	0.26	38.4	10	10.0
3	iE33	X7-2t	drop m	31	31.2	0.7	96.0	317	0.30	43.4	13	18.1
3	iE33	X7-2t	drop l	21	31.2	0.8	125.4	300	0.42	43.2	18	35.6

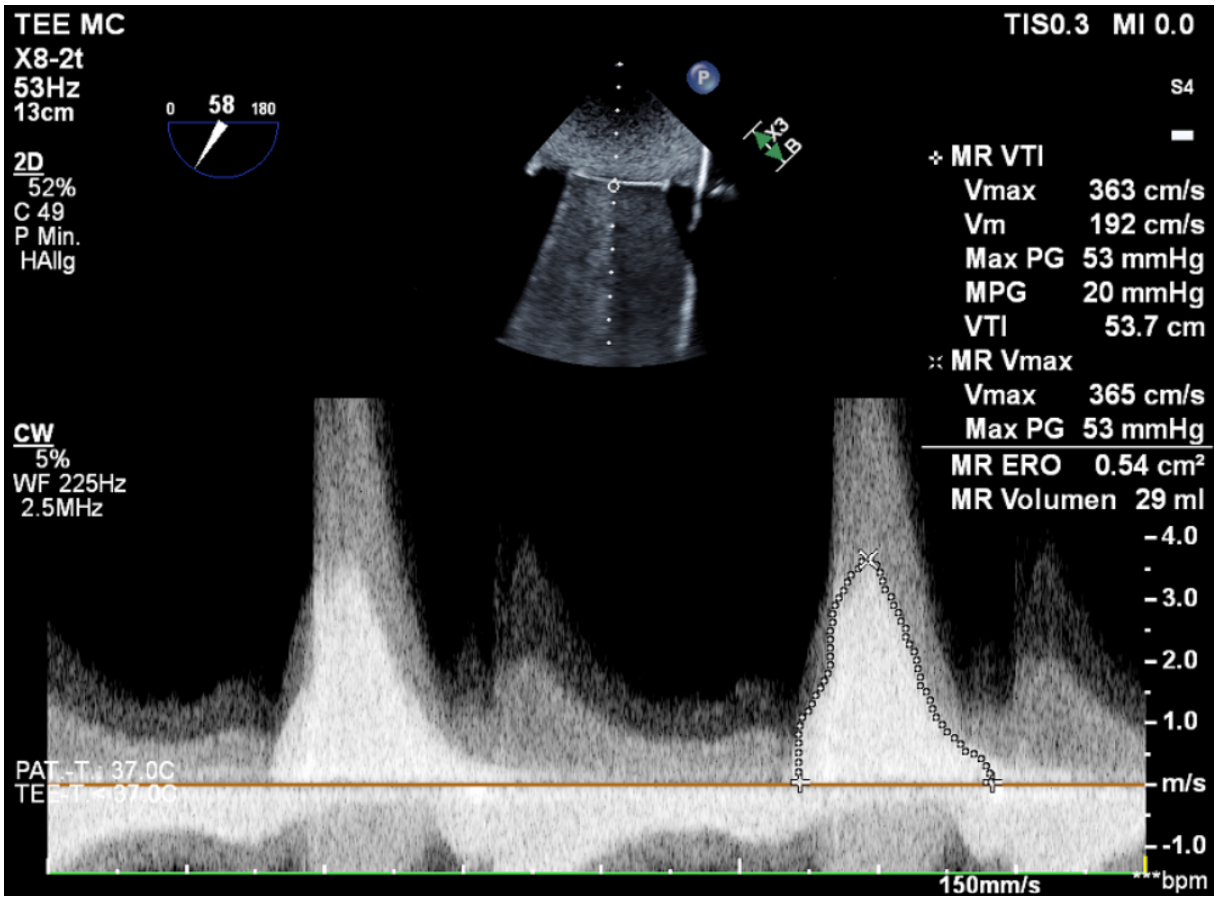

Figure 3.13: Determination of VTI in CW-mode for pointed oval l. The velocity time integral(VTI) of 53.7 cm is determined under the dotted line with the maximal regurgitation speed (MR Vmax) of 365cm/s. Resulting in an effective regurgitant orifice (MR ERO) of 0.54 cm ^{2} and consequently a regurgitation volume (MR Volumen) of 29 ml.

dashed line indicates the area where the regurgitation volume is extracted using PIV. This procedure is executed for all geometries to quantify the regurgitation volume using phase-averaged PIV images, as explained in Section 3.2.2. Table 3.6 shows in the last column the corresponding regurgitation volume of each phantom determined by PIV.

3.2.3 Comparison of the flow convergence method and particle image velocimetry

The outcomes from both PIV and flow convergence measurements are presented in Figure 3.15 and Table 3.7. The results demonstrate that the average regurgitation volume calculated with the flow convergence method was smaller for eight out of nine regurgitation phantoms in comparison to PIV measurements. Across all shapes, the regurgitation volume increased proportionally to the size, both for PIV and ultrasound measurements.

In addition, mild regurgitation volumes measured by PIV deviated by 1.0 to 5.4 ml and 10 to 32.0 % from the mean flow convergence regurgitation volumes and were still classified as mild regurgitation volumes by ultrasound standards. The regurgitation induced with the three large regurgitation phantoms would be categorized as moderate mitral regurgitation

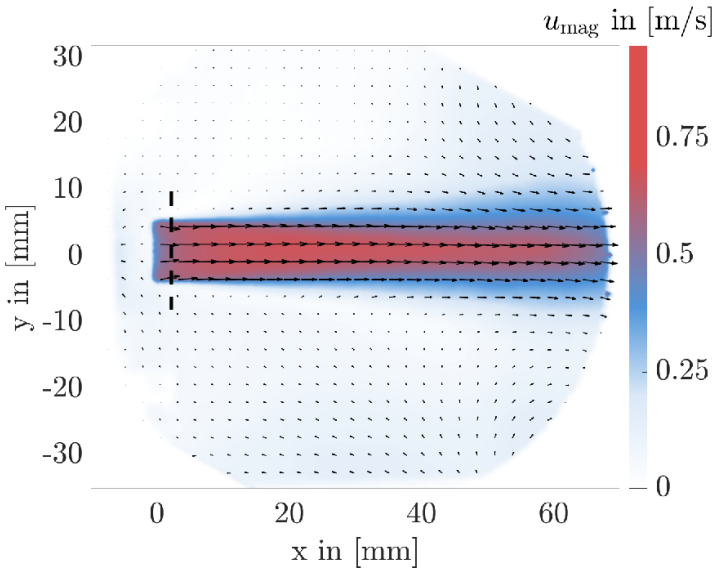

Figure 3.14: Phase-averaged velocity distribution along the atrium to extract the regurgitation volume. The x-value, where the volume is calculated is marked with a dashed line (- -). The vena contracta – although less pronounced than for smaller orifices – can be identified using an inward-tending velocity component. (Only every fifth vector is shown for clarity.)

via PIV assessment, but as mild mitral regurgitation through flow convergence evaluation. The differences in regurgitation volume measurements between the two methods for this case were between 11.6 to 23.2 ml and 32.6 to 51.7 %.

Table 3.7: Comparison of the regurgitation volumes (RVol) measured by using particle image velocimetry (PIV) and the flow convergence method averaged (FCMa) over all physicians. s = small, m = medium, l = large.

	circle			pointed oval			drop		
	s	m	l	s	m	l	s	m	l
RVol_{PIV} [ml]	4.6	20.0	35.1	9.1	15.2	44.9	10.0	18.1	35.6
RVol_{FCMa} [ml]	6	16.7	21.3	6.7	10.3	21.7	9.0	17.7	24.0
deviation [ml]	1.4	3.3	13.8	2.4	4.9	23.2	1.0	5.4	11.6
deviation [%]	23.3	16.7	39.2	26.7	32.0	51.7	10.0	30.0	32.6

Furthermore, the variation between the readings of physicians using the "pointed oval l" and "drop l" regurgitation phantoms is more pronounced than with the other regurgitation phantoms. Figure 3.16 illustrates that the shape of the orifice influences the regurgitation volume. In particular, for the large orifice shapes there was a visible difference in regurgitation volumes measured by using PIV. Even though the orifice area was for all three similar (108.4 - 116.7 mm^2), the regurgitation volume differed visibly. For example, the regurgitation volume of "circle l" (35.1 ml), which had the largest orifice area, was the smallest and the regurgitation volume of "pointed oval l" (44.9 ml) was the largest.

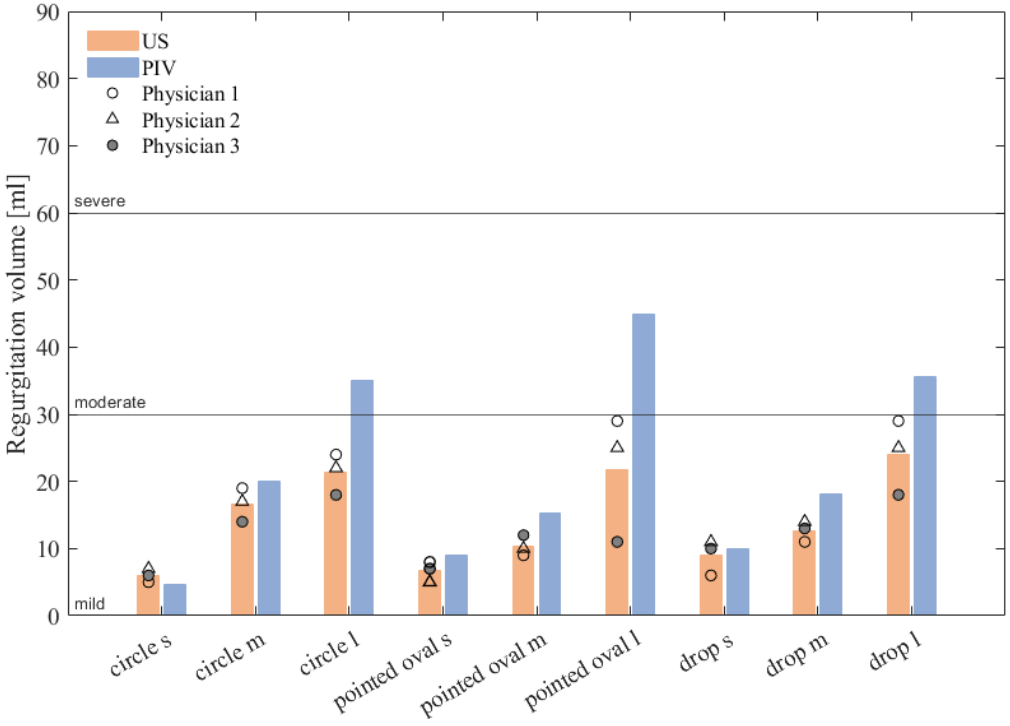

Figure 3.15: Regurgitation volume measured by TEE and PIV for each regurgitation phantom. Transesophageal echocardiography (TEE) bars show the mean regurgitation volume and the three individual measurements obtained by the physicians. Horizontal lines indicate mild, moderate, or severe mitral regurgitation. PIV = particle image velocimetry.

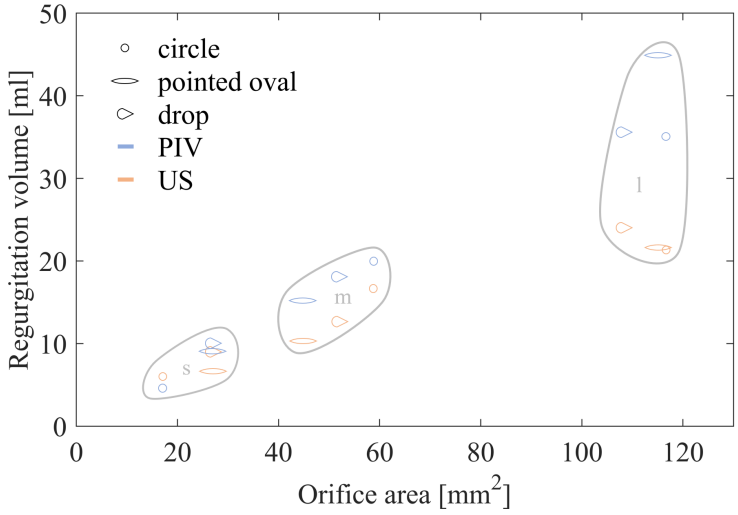

Figure 3.16: The regurgitation volume over orifice area determined by ultrasound (US) and particle image velocimetry (PIV) for each regurgitation phantom. All regurgitation phantoms of one shape are encircled in grey, and labeled with s, m, and l to indicate the size. Ultrasound values represent the mean of the measurements obtained by all three physicians.

3.3 Evaluation of the aortic simulator

This section comprises the results to provide a realistic hemodynamic environment, including the influences of TEVAR on the flow, the compatibility of the simulator with CT scanners, and the feasibility of performing TEVAR and DSA.

3.3.1 Providing realistic hemodynamics

The flow and pressure data was acquired in collaboration with Mr. Lukas Mohl.

Evaluation of flow and pressure ensures a physiological hemodynamic environment and allows for studying the effects of TEVAR on each aortic branch individually. Therefore, the flow and pressure were measured at the aortic root as shown in Figure 3.17 and additionally the flow of each aortic branch was measured before and after TEVAR. A summary of the measurements is shown in Figure 3.18. The systolic pressure at the aortic root was 132 mmHg

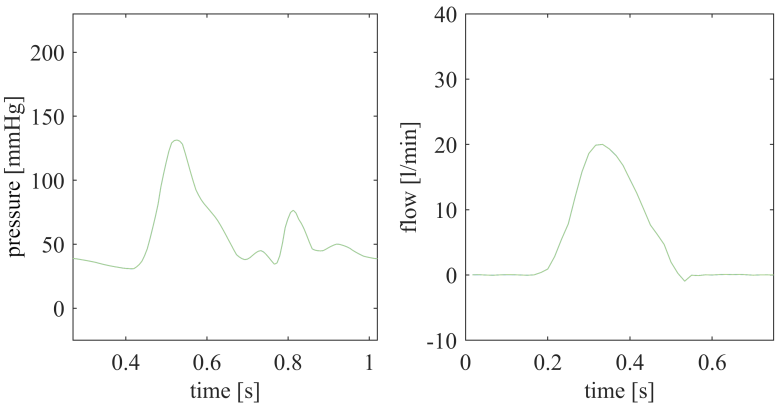

Figure 3.17: Pressure (left) and flow (right) of the aortic simulator for one heart cycle. *The pressure and flow data was acquired in collaboration with Mr. Lukas Mohl.*

with a flow of 4.7 l/min, which corresponds to a stroke volume of 59 ml. With a frequency of 80 bpm, these values display a physiological hemodynamic environment. During diastole, the pressure decreased to 30 mmHg, which can be explained by missing peripheral resistance. This value is clearly below a physiological value of 80 mmHg, however this plays a subordinate role for the simulator. Furthermore, a second pressure peak is observed (Figure 3.17, left at 0.55 s). This pressure peak is induced due to the closure of the aortic valve and starts precisely after the period of negative flow (Figure 3.17, right). In the human body this peak would be entirely absorbed by the so-called windkessel function of the aorta.
The TEVAR procedure affected the flow through each aortic branch. The flow of the truncus brachiocephalicus increased from 0.47 l/min by 0.08 l/min (17.0 %) to 0.55 l/min. The flow of the arteria carotis communis sinistra decreased from 0.43 l/min by 0.01 l/min (2.3 %) to 0.42 l/min. The flow of the arteria subclavia sinistra decreased from 0.53 l/min by 0.06 l/min (11.3 %) to 0.47 l/min. The flow through the truncus coeliacus increased from 0.34 l/min by 0.05 l/min (14.7 %) to 0.39 l/min. The flow of the arteria suprarenalis media decreased from

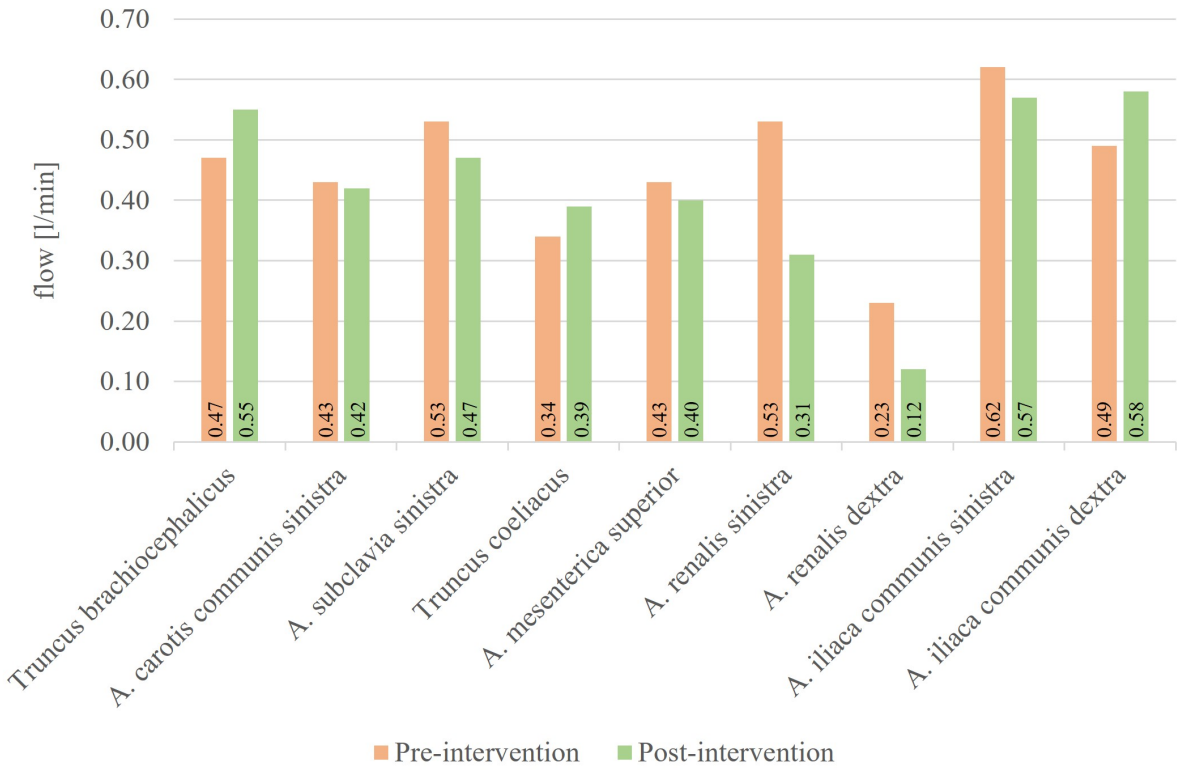

Figure 3.18: Flow through the aortic branches prior and after thoracic endovascular aortic repair. *The flow data was acquired in collaboration with Lukas Mohl.*

0.43 l/min by 0.03 l/min (7 %) to 0.40 l/min. The flow of the arteria renalis sinistra decreased from 0.53 l/min by 0.22 l/min (41.5 %) to 0.31 l/min. The flow through the arteria renalis dextra decreased from 0.23 l/min by 0.11 l/min (43.5 %) to 0.12 l/min. The flow of the arteria iliaca communis sinistra decreased from 0.62 l/min by 0.05 l/min (8.1 %) to 0.57 l/min and the flow of the arteria iliaca communis dextra increased from 0.49 l/min by 0.09 l/min (18.4 %) to 0.58 l/min.

3.3.2 Compatibility with computed tomography angiography

Evaluating a feasible setup of the simulator and possible settings for the CT scanner involved conducting four different CTA scans of the aortic phantom. Table 3.8 shows the setup of the simulator and the scanner settings for each experiment. The first scan was obtained with Laponite as an extravascular medium, no contrast agent added to the blood-mimicking fluid, and the aortic phantom not connected to the flow-loop. It can be seen, that air was encapsulated by the Laponite (Figure 3.19a). The aortic and dissection walls are visible. The blood-mimicking fluid and the extravascular medium appear similar, possibly due to the high content of H_2O in both mediums. The positions one and two are indicated in Figure 2.10.

A contrast agent was added via the aortic root to increase the contrast between blood-mimicking fluid and the extravascular medium. Due to the absence of flow, the contrast agent did not

Table 3.8: Computed tomography angiography settings used with the aortic phantom. Exp. = experiment, CA = contrast agent, SL = slice thickness in mm, P = pitch.

Exp.	Flow	CA	extra vascular medium	mAs	kV	SL	P
a)	no	no	Laponite gel	26	90	3	3
b)	no	yes	Laponite gel	24	90	3	3
c)	yes	yes	Laponite gel	12	90	1	1
d)	yes	yes	H_2O	116	90	1	0.6

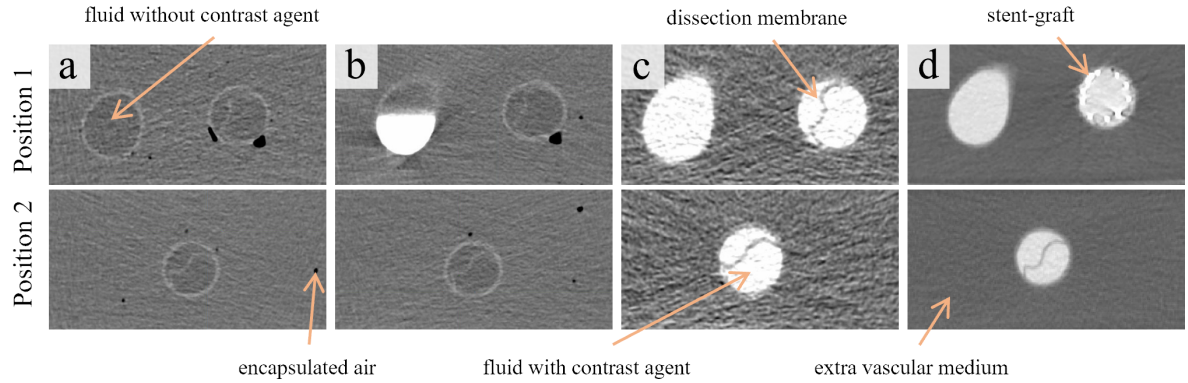

Figure 3.19: Axial view of computed tomography angiography scans of the aortic phantom with different setups. Position 1 represents an axial layer distal to the aortic arch, Position 2 represents an axial layer proximal to the truncus coeliacus. a) without flow and the use of contrast agent and Laponite gel as the extravascular medium, b) without flow, with contrast agent applied from the aortic root, and Laponite gel as the extravascular medium, c) with flow, contrast agent, and Laponite gel as extravascular medium, d) with the flow, contrast agent, and water as the extravascular medium. Orange arrows indicate the dissection membrane, stent-graft, and the proximal entry of the false lumen.

distribute through the aorta but stayed within the aorta ascendens. This can be seen by the bright region in Figure 3.19b, Position 1, left. If the contrast agent would have distributed equally all lumen in Position 1 and 2 would appear bright. The contrast agent separated from the blood-mimicking fluid because of its higher density. This is indicated by the aggregation at the bottom of the lumen (Figure 3.19b, Position 1, left).

The aortic phantom was integrated into the flow-loop to enable equal distribution of the contrast agent. The pump and reservoir were positioned next to the scanner and motorized table, and the phantom was placed on top of the table as visible in Figure 3.20.
No parts of the flow-loop must interfere with the motorized table of the scanner. Free movement of the table into and out of the scanner has to be ensured, therefore the connecting tubes have to be long enough and positioned without possible entanglement. To ease the setup only the aortic root and the arteriae iliacae communes dextra and sinistra were connected to the flow-loop. The repeated CTA-scan in Figure 3.19c shows the equal distribution of contrast agent within the aortic phantom. This led to an improved visibility of the dissection membrane. Compared to Figure 3.19a, b, Figure 3.19c showed an increase in noise, which can be explained by the reduction of radiation from 24 and 26 mAs to 12 mAs. Fur-

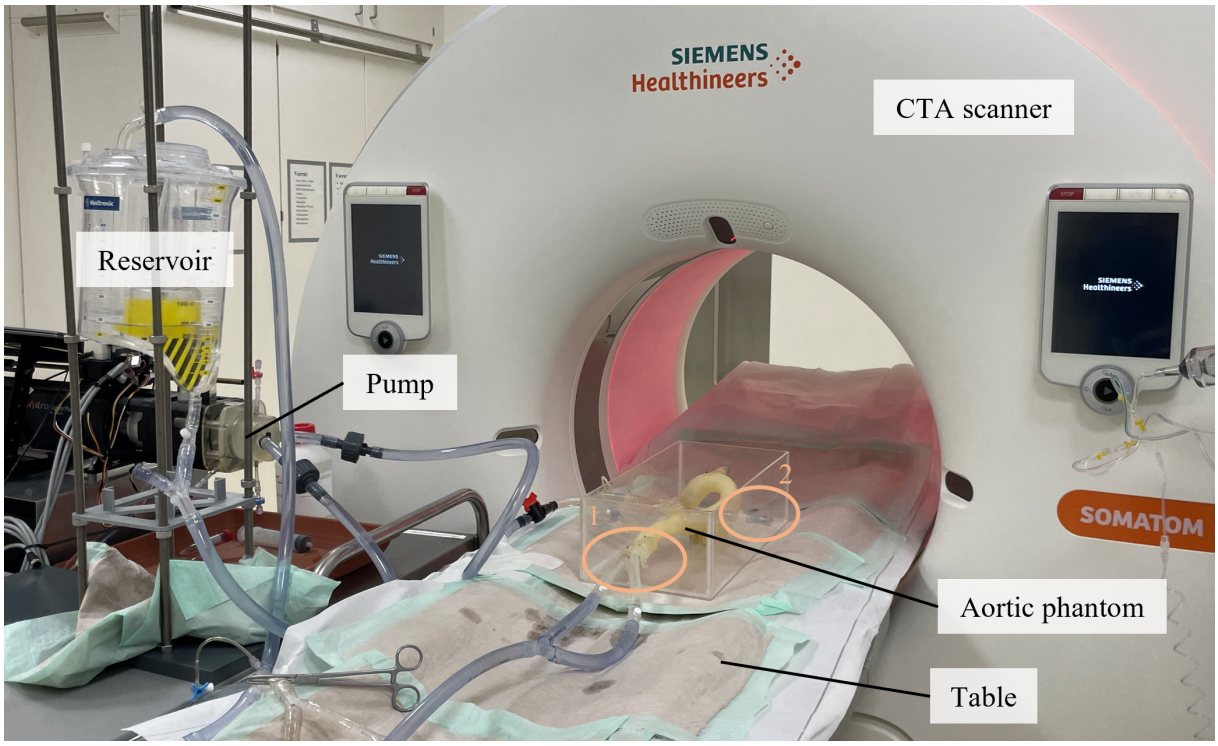

Figure 3.20: Aortic phantom inside the CT scanner. The pump and reservoir are positioned aside from the motorized table of the CT scanner. The aortic phantom is placed on top of the table. The aortic root and the arteria iliaca communis dextra and sinistra (circle one) are connected to the flow-loop. The other aortic branches such as the arteria renalis sinistra (circle two) are not connected to the flow-loop to ensure a fit inside the CT scanner.

thermore, the first three attempts showed the encapsulation of air, visible by the black areas in Figure 3.19a-c, inside the extravascular medium.

The Laponite was exchanged by water to avoid the encapsulation of air. Additionally, the fourth CTA scan was done with increased radiation of 116 mAs to assess the effects of different radiation. As seen in Figure 3.19d the use of water as the extravascular medium and the increase of radiation led to the elimination of air bubbles and noise, respectively. With these settings, the dissection membrane was visible in Position 2. The absence of the dissection membrane in Position 1 is due to an implanted stent-graft in the descending thoracic aorta, which was not implanted during the first three attempts.

Figure 3.21 shows two different coronal layers of the aortic phantom pre- and post-interventional. The first layer (Figure 3.21a, c) shows a cross-sectional view of the aortic arch, with a visible entry pre-interventional (Figure 3.21a) and a remodeled aortic arch by the stent-graft (Figure 3.21c). The second layer (Figure 3.21b, d) shows the course of the dissection wall through the thoracic aorta pre- and post-interventional. As mentioned before, also in the coronal view the encapsulated air in the Laponite gel and the noise due to low radiation is visible (Figure 3.21a, b). However, air bubbles are trapped between the stent-graft and the aortic wall (Figure 3.21c, d). The coronal CTA scans show the anatomy of the aortic phantom and the position of the stent-graft.

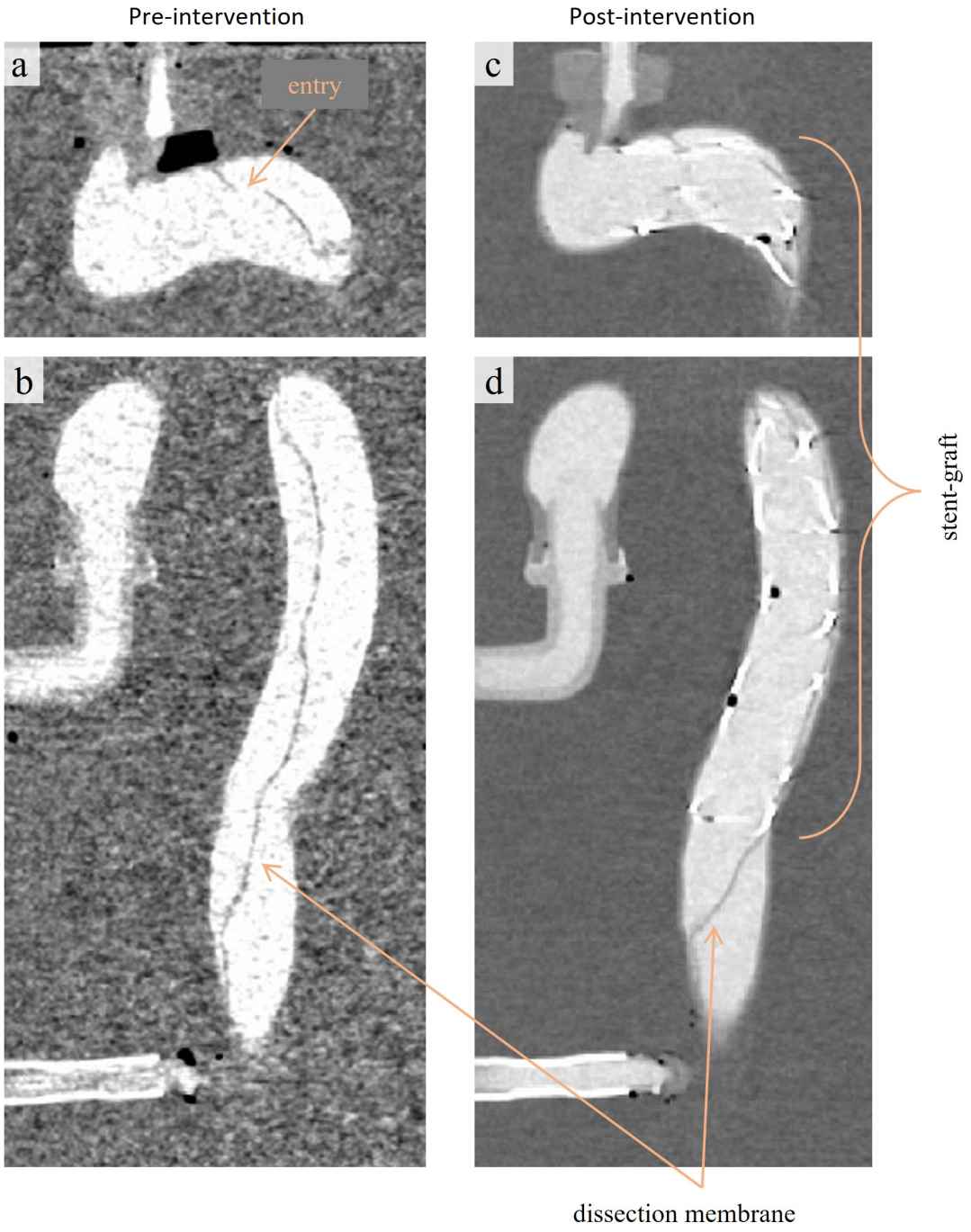

Figure 3.21: Pre- (left) and post- (right) interventional computed tomography angiography scan at two different coronal layers. a) showing the proximal entry and b) the dissection membrane separating the true and false lumen, c) showing the sealed proximal entry, d) the remodeling of the true lumen in the area of the stent-graft.

3.3.3 Feasability of thoracic endovascular aortic repair

The TEVAR experiment was performed in collaboration with Mr. Lukas Mohl.

TEVAR was performed by two vascular surgeons in a hybrid operation room (Figure 3.22) of the university hospital of Heidelberg. A pigtail catheter was introduced via an introducer

sheath into the arteria iliaca communis dextra. The catheter was guided through the true lumen of the abdominal aorta, thoracic aorta descendens, and aortic arch, into the aorta ascendens. DSA was performed multiple times as shown in Fig. 3.23 to ensure correct navigation. Contrast agent was applied manually. Figure 3.23a shows the progress of the pigtail

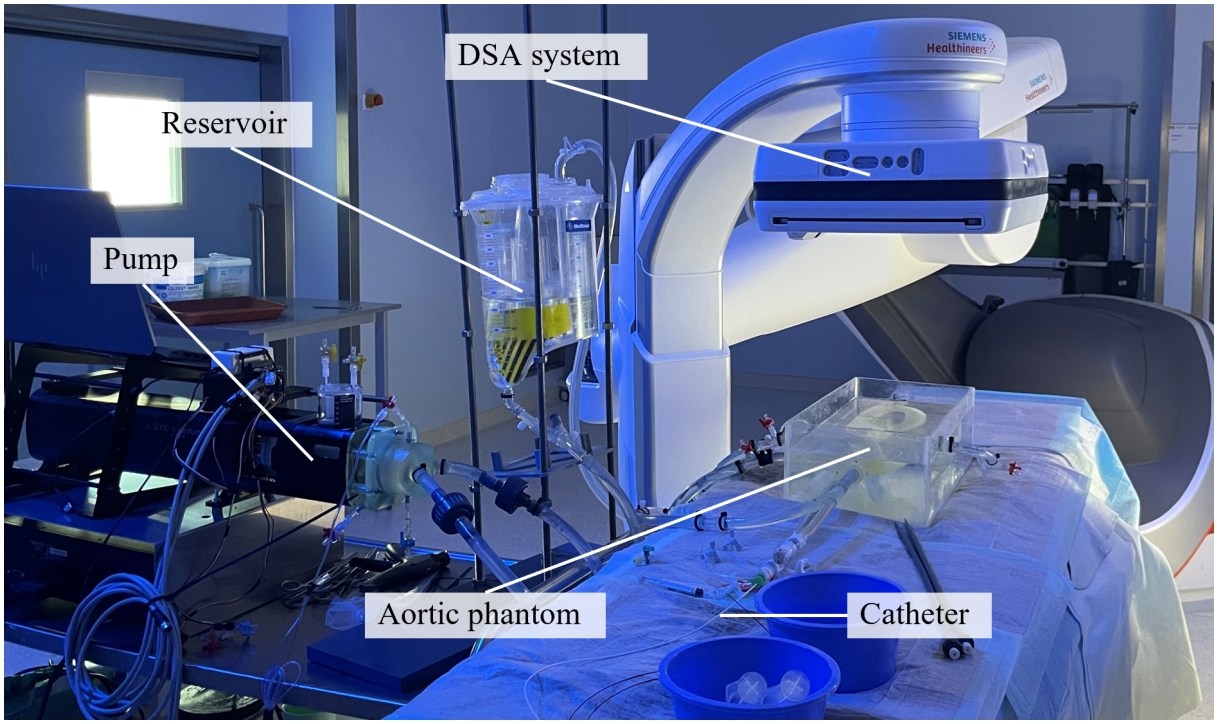

Figure 3.22: Aortic phantom in a hybrid operation room. The pump and reservoir are placed next to the operation table. The aortic phantom is placed on the operation table aligned to the DSA scanner. A pigtail catheter is approached through the introducer sheath into the true lumen. This figure was originally published in Mohl et al. (2024), adapted and reused under the CC BY 4.0 - Licence.

catheter in the abdominal aorta, with contrast agent flow in the distal abdominal aorta, truncus coeliacus, arteria mesenterica superior, arteria renalis dextra, and through a re-entry. After reaching the aortic arch, a second scan of the abdominal aorta (Figure 3.23b) showed a clear separation of the contrast agent-filled true lumen (dark), and the non-contrast agent-filled false lumen (bright). The DSA scan of the thoracic aorta (Figure 3.23c) showed a contrast agent flowing through the entry into the false lumen. Finally, the catheter was advanced into the aorta ascendens (Figure 3.23d). DSA showed an equal distribution of contrast agent between the true and false lumen. Furthermore, a sharp turn of the catheter was visible near the entry.

After steering the pigtail catheter into the aorta ascendens, it was replaced by a stiff wire to guide the TEVAR device into the aortic arch as displayed in Figure 3.24and 3.25a.

It was not possible to maneuver the device through the aforementioned sharp turn by conventional methods. This might have been caused by the increased stiffness of the device, roughness of the aortic phantom material, anatomy of the aorta, or the position of the entry. It was therefore necessary to bend the aortic phantom by hand. After finalizing the posi-

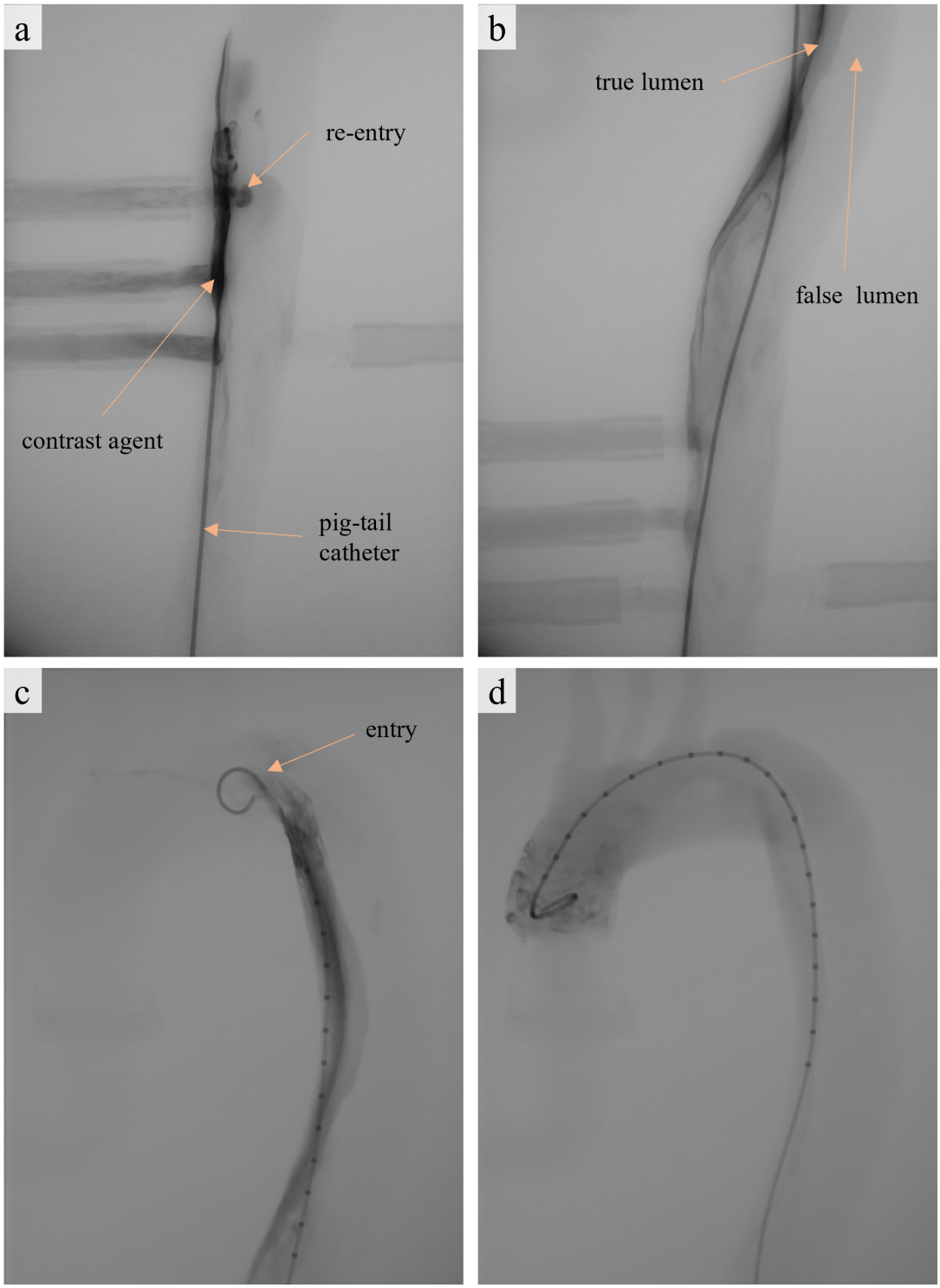

Figure 3.23: Guiding the pigtail catheter through the aortic phantom under digital subtraction angiography. a) showing the catheter inside the true lumen of the abdominal aorta, with contrast agent (dark fluid) flowing mainly through the true lumen and aortic branches, but also entering the false lumen via a re-entry, b) showing the separation of the true and false lumen of the abdominal aorta by contrast agent, c) the pigtail catheter reaches the aortic arch, contrast agent mainly flows through the true lumen, but slightly enters the false lumen via the entry, d) the pigtail catheter reached the aorta ascendens, and the contrast agent equally distributes into the true and false lumen. *The DSA data was acquired in collaboration with Mr. Lukas Mohl.*

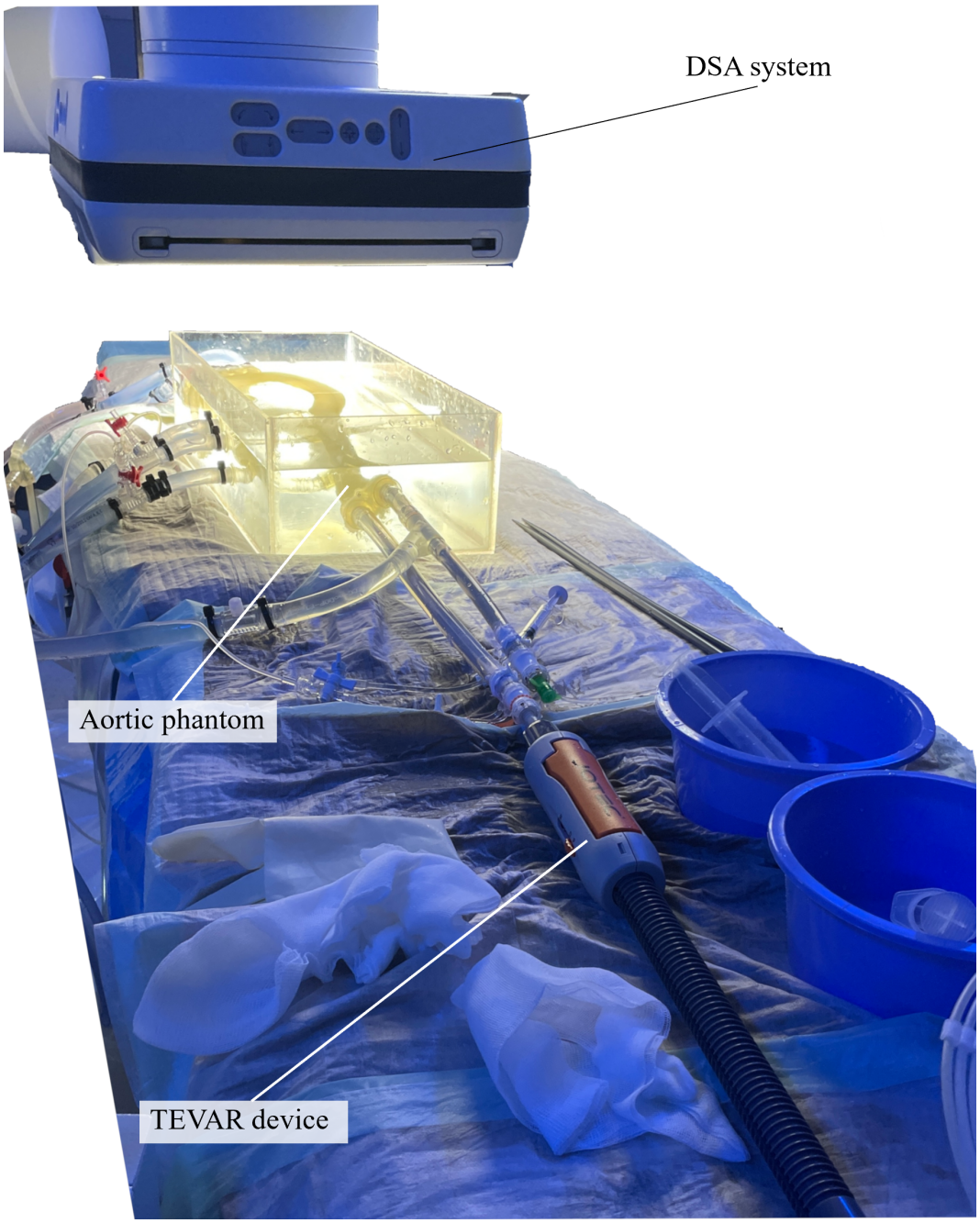

Figure 3.24: TEVAR procedure at the aortic simulator. The aortic phantom was placed on the operation table aligned to the DSA scanner. The TEVAR device was advanced into the aortic phantom. This figure was originally published in Mohl et al. (2024), adapted and reused under the CC BY 4.0 - Licence.

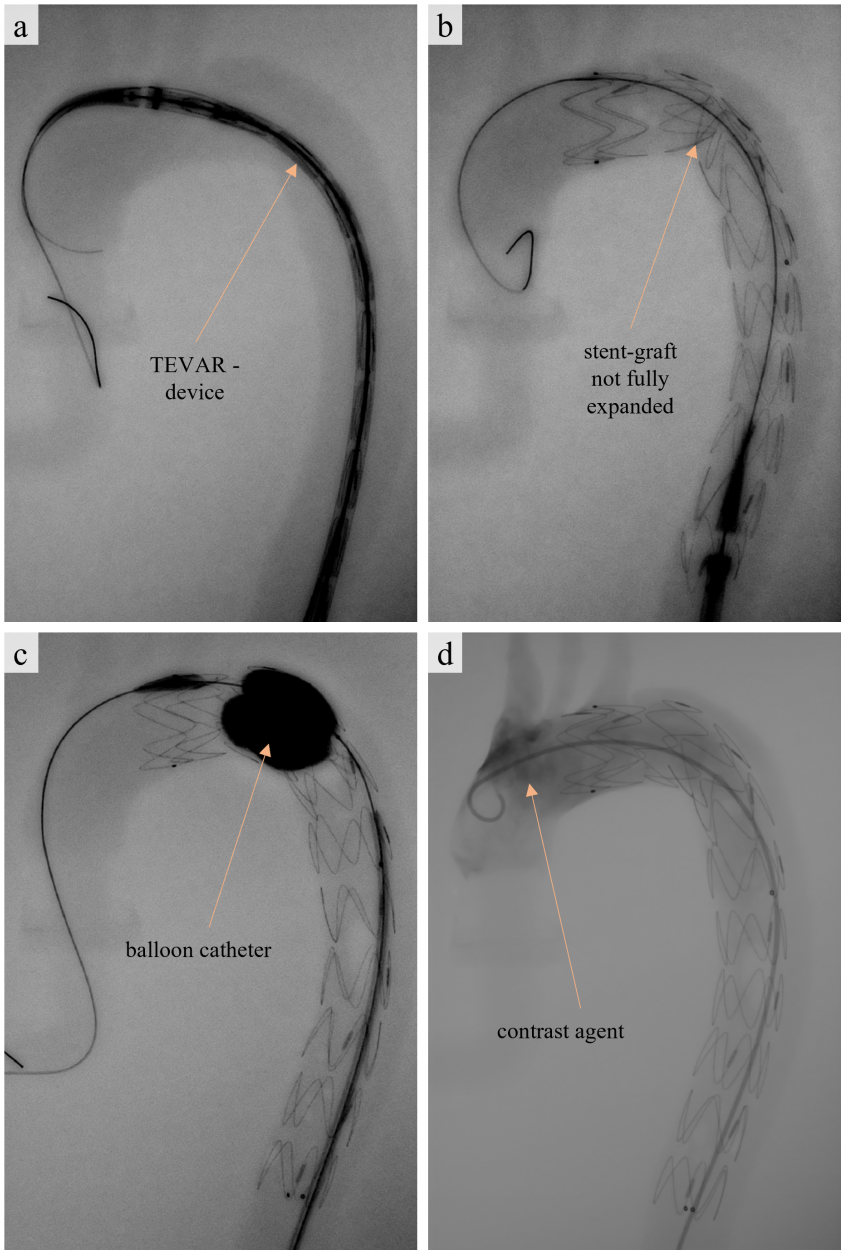

Figure 3.25: Placing the stent-graft in the aortic phantom. a) The pigtail catheter is replaced by the TEVAR-device. b) The stent-graft is deployed with an approximately 25 mm proximal landing zone covering the entry and arteria subclavia sinistra, distal to the entry. The stent-graft was unable to expand correctly. c) A balloon catheter was used to support the deployment of the stent. d) Digital subtraction angiography showing contrast agent (dark fluid) entering the false lumen, indicating incomplete sealing of the entry. TEVAR = thoracic endovascular aortic repair. This figure was originally published in Mohl et al. (2024), adapted and reused under the CC BY 4.0 - Licence.

tion with a proximal landing zone of approximately 25 mm, the stent-graft was deployed. As shown in Figure 3.25b, the stent-graft did not expand correctly in the region of the entry. To support the expansion of the stent-graft, a balloon catheter was introduced into the stent-graft and inflated (Figure 3.25c). The stent-graft consequently expanded to the full extent and the true lumen was successfully remodeled in the section of the stent-graft (Figure 3.25d and Figure 3.21c, d). DSA was performed and small amounts of contrast agents entered the

entry into the false lumen, indicating incomplete sealing of the entry. The final position of the stent-graft was evaluated in CTA scans. This can be seen in the coronal projection (Figure 3.26), cross-sectional axial view (Figure 3.19d), and coronal view (Figure 3.21c,d).

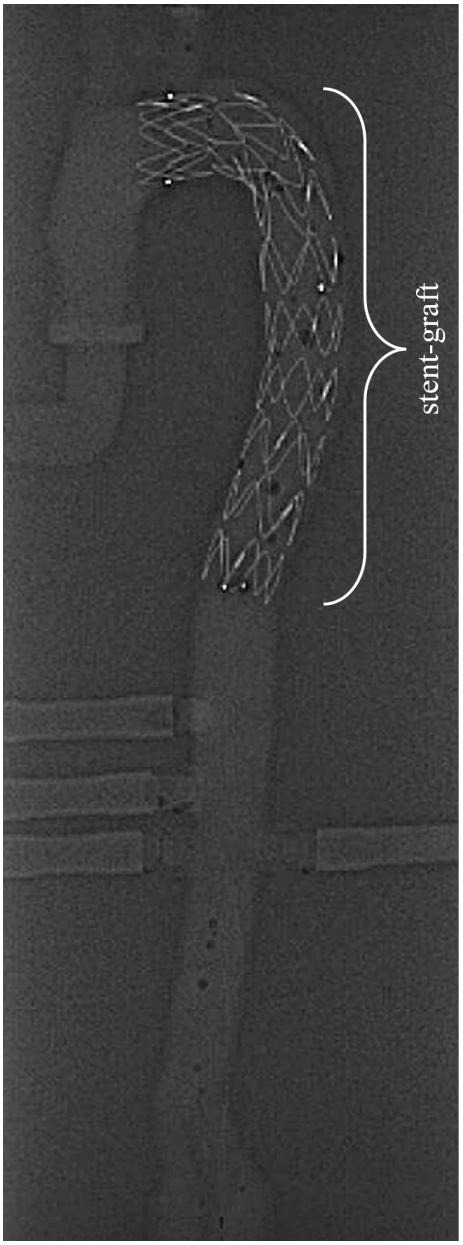

Figure 3.26: Post-interventional computed tomography angiography topographic scan of the aortic phantom showing the position and course of the stent-graft. This figure was originally published in Mohl et al. (2024), adapted and reused under the CC BY 4.0 - Licence.

4 Discussion

This chapter covers the discussion of this thesis. It includes an evaluation of how the mitral valve simulator fulfilled the requirements and how it performed in contrast to the state of the art. Additionally, the evaluation of the flow convergence method and how its shortcomings can be quantified, are discussed. Furthermore, the performance of the aortic flow-loop compared to the state of the art and the set requirements is discussed. Finally, a conclusion of this thesis is provided.

4.1 Left heart simulation to train and plan mitral valve repair

A left heart simulator was presented that can accommodate mitral valve models to evaluate and compare their dynamics as well as simulate interventions to treat mitral valve pathologies. Unlike existing simulators, the system presented here offers a unique combination of features, including the integration of the entire mitral valve apparatus (MVS-R1), realistic hemodynamics (MVS-R2), the capability to perform both surgical (MVS-R3) and cardiac (MVS-R4) interventions, as well as detailed measurement capabilities through medical imaging (MVS-R5) and industrial sensors (MVS-R6).

4.1.1 Functionally incorporating mitral valves (MVS-R1)

Functional integration of the entire mitral valve apparatus in the simulator (MVS-R1) is pivotal for modeling mitral regurgitation pathologies and their treatment. The mitral valve may be described as a "clockwork", in which every single part plays a crucial role for the overarching function as described in Section 1.3.1. Since failure of single parts may result in mitral regurgitation, every part might potentially need repair to restore mitral valve function. However, Ginty et al. (2018), Boone et al. (2019), and Zimmermann et al. (2021) did not integrate papillary muscles and the chordae tendineae were attached to static points. Therefore, surgical approaches such as chordaeplasty could not be simulated, since neo-chordae are physiologically attached to the papillary muscles. Work by Engelhardt et al. (2019) and Fischer et al. (2023) integrated the entire anatomy of the mitral valve, consequently allowing for the performance of surgical simulations; however, these simulations are limited to qualitative evaluation due to the missing hemodynamic environment, which also excludes beating heart interventions such as TEER. Gollmann-Tepeköylü et al. (2018) and Paulsen et al. (2020) included the entire mitral valve apparatus functionally in their simulators. Especially Paulsen et al. (2020) were able to mimic an *in-vivo*-like behavior of the mitral valve with their setup. While their simulator presents a solid base for research, it lacks the opportunity of training and planning of mitral valve repair.

Similar to Paulsen et al. (2020), the simulator developed in this project allows for the integration of the entire mitral valve apparatus, including the annulus, leaflets, chordae tendineae, and papillary muscles. To demonstrate functional integration of all components, pathologies such as chordae rupture and annulus dilatation were induced. Impairing the mitral valves led to compromised valve competency and mitral regurgitation with moderate severity (grade 2). Repairing chordae rupture by neo-chordae insertion and annulus dilatation by TEER, resulted in a reduced mitral regurgitation severity of grade 0 and grade 1, respectively. In conclusion, within the proposed simulator, defects of different parts of the mitral valve may be simulated and subsequently repaired, mimicking *in-vivo*-like behavior like decreased and increased mitral valve competency.

While functional mitral valve integration was successful, limitations occurred that should be addressed in future work. In the proposed simulator the papillary muscles are attached to the chordae tensioners. While these chordae tensioners allow for adjustment, repositioning has to be done manually and is only possible along one axis. During the heart cycle, however, the distance between the papillary muscles and the annulus plane is dynamic, which cannot be mimicked in the current version of the simulator. Furthermore, interventions such as TEER typically induce repositioning of the papillary muscles in relation to the annulus plane. To allow for this in the future, the simulator should enable three-dimensional repositioning of the papillary muscles. This repositioning should be possible manually on a large scale to mimic the patient's anatomy, and automatically on a small scale to reproduce dynamic and interventional effects.

4.1.2 Creating a hemodynamic environment (MVS-R2)

A simulation of mitral valve behavior of physiological or pathological mitral valves requires a realistic hemodynamic environment (MVS-R2). With competent valves, the systolic blood pressure is physiologically at approximately 120 mmHg with 5 l/min cardiac output at a frequency of 60 - 100 bpm (Brandes et al., 2019, p. 166-216). Furthermore, a quantitative evaluation of intervention simulation can only be provided in a lifelike environment. Simulators introduced by Engelhardt et al. (2019), Sardari Nia et al. (2019), Fischer et al. (2023) do not provide any dynamic environment. Consequently, only limited information can be obtained, and its dynamic behavior cannot be captured. Additionally, the effects of MIMVS on the competency of the mitral valve can only be estimated. Since TEER is performed at the beating heart, it cannot be simulated in static simulators. Gollmann-Tepeköylü et al. (2018) and Zimmermann et al. (2021) introduced dynamic environments to integrate the simulation of TEER.

Gollmann-Tepeköylü et al. (2018) used an entire porcine heart connected to a pulsatile pump. While this setup led to the opening and closing of the mitral valve, it failed to replicate authentic hemodynamic conditions across the mitral valve due to the absence of systolic pressure generated by the left ventricle. Consequently, the authors' setup enables physicians

to familiarise themselves with the TEER system, but it does not allow for quantitative evaluation of the performance or the integration of patient-specific pathologies. Zimmermann et al. (2021) introduced a simulator without any fluid but a mitral valve connected to a motor to induce the opening and closing of the valves. Without fluid, the competency of the mitral valve and consequently the success of repair cannot be evaluated. To quantitatively assess the effects of mitral valve repair, Boone et al. (2019) and Ginty et al. (2018) developed a simulator with a hemodynamic environment. Although their approaches effectively provided lifelike hemodynamic conditions, they lack the functional integration of chordae tendineae and papillary muscles, as well as the possibility of simulating repairs inside the simulator. For instance, papillary muscles were not included in these simulators, so chordaeplasty could not be simulated. Furthermore, the simulation of surgery needs to be performed outside of the simulator and does not replicate a right lateral minithoracotomy environment. Paulsen et al. (2020) used the commercially available simulator by Vivitro Labs to evaluate the forces on chordae tendineae. While their simulator reproduces lifelike hemodynamic conditions, trans-septal or minithoracotomy-like accesses were not integrated and consequently, the performance of neither TEER nor MIMVS can be simulated. However, due to its accurate replication of hemodynamics, the pulsatile piston pump by Vivitro Labs, used by Paulsen et al. (2020), is also the base for the simulator developed within this study.

To evaluate a lifelike hemodynamic environment for competent mitral valve simulations, both biological and mechanical prosthetic mitral valves were utilized. Additionally, the simulator's performance using human-like mitral valves was evaluated by incorporating *ex-vivo* porcine valves. Both prosthetic and competent porcine mitral valves accurately reproduced physiological systolic blood pressures (117 - 120 mmHg) and cardiac outputs (4.55 - 4.9 l/min). Furthermore, pathological valves induced regurgitation jets that replicated known *in-vivo* shapes and volumes (24 -32 ml).

While realistic hemodynamic conditions of the simulator were demonstrated, future work may still advance the simulator. Currently, the left atrium and reservoir are combined, resulting in a high water level that causes the pressure inside the left atrium to exceed physiological levels. Redesigning the system to separate the reservoir from the left atrium may reduce the water level and consequently facilitate more accurate physiological left atrial pressures. Furthermore, the rigid material of the left atrium and reservoir did not absorb fluid pressures as the actual tissue would. Therefore, an enclosed reservoir would have led to equal pressures within the left atrium and left ventricle since the mitral valve transfers pressures to a certain extent. To prevent this, the reservoir was designed not fully enclosed, but open to the environment. Acute mitral regurgitation, however, results in increased atrial pressure during systole in humans, which cannot be replicated at the current state. Including a windkessel would allow the left atrium to mimic the increase in pressure as induced by acute mitral regurgitation, while mimicking the absorbing effects of tissue and consequently replicate atrial pressures more lifelike.

4.1.3 Enabling minimally invasive mitral valve surgery (MVS-R3) and transcatheter edge-to-edge repair (MVS-R4)

MIMVS (MVS-R3) and TEER (MVS-R4) are common therapies to treat mitral regurgitation, performed in cardiac surgery and cardiology, respectively. Due to their complexity, a high level of experience and regular practice is required for top-level performance. While each of these therapies has their right to exist, the therapy decision is dependent on several factors and not always distinct. A realistic training and planning tool could consequently increase the level of performance and support the process of decision-making. Multiple simulators have already demonstrated the feasibility of either train surgical (Boone et al., 2019) or transcatheter repair (Gollmann-Tepeköylü et al., 2018) of mitral valves.

Surgical simulators, however, either lack the integration of the entire mitral valve anatomy and do not allow for surgery at the simulator itself (Ginty et al., 2018, 2019), or they fail to provide a hemodynamic environment (Engelhardt et al., 2019; Sardari Nia et al., 2019; Fischer et al., 2023). Gollmann-Tepeköylü et al. (2018) and Zimmermann et al. (2021) presented simulators for TEER; however, both lack realistic hemodynamic conditions and the opportunity to integrate patient-specific mitral valves. Gollmann-Tepeköylü et al. (2018) used an entire porcine heart, which does not allow to mimic patient-specific pathologies such as annulus dilatation. Zimmermann et al. (2021) did not integrate the entire mitral valve anatomy, so even if leaflets represent personalized anatomy, valvular structures such as papillary muscles were not included. The importance of realistic hemodynamics and the integration of entire mitral valve anatomy was discussed above, consequently, the lack of these features represents a major downside of the simulators mentioned.

While MIMVS involves a transthoracic approach on the arrested heart, TEER is executed on the beating heart through transseptal access. None of the proposed simulators combine the integration of both, which is necessary to compare the technologies for decision-making. In contrast, the simulator developed in this thesis, accurately simulates both types of access, enabling simulation of both interventions within one device. This thesis demonstrates the feasibility of performing MIMVS and TEER inside the simulator, resulting in a reduction of mitral regurgitation in pathological porcine and patient-specific silicone valves. In the future, the simulator holds the potential to integrate and model additional techniques. Transseptal interventions such as *Cardioband* (Edwards Lifesciences, Irvine, USA) and *Chord-Art* (CoreMedic GmbH, Radolfszell, Germany) can potentially be incorporated without design modifications. Approaches like the *HARPOON*-system (Edwards Lifesciences, Irvine, USA) or *MitralStitch* (Hangzhou Valgen Medtech Co., Ltd, Hangzhou, China) might require design adaptations. The modular construction of the simulator will facilitate their integration.

4.1.4 Integrating medical imaging (MVS-R5)

Medical imaging (MVS-R5), specifically TEE, plays a major role in the assessment of mitral regurgitation and the therapy to treat it. TEE is used to diagnose mitral regurgitation, for guidance and assessment during TEER, and evaluation of repair outcome. Paulsen et al. (2020) and Ginty et al. (2018) used TEE to assess the behavior of mitral valves in a hemodynamic environment. Gollmann-Tepeköylü et al. (2018) used TEE to guide and assess TEER. I demonstrated that TEE was successfully employed in the proposed simulator to assess the mitral valve and to provide guidance during TEER procedures. For instance, regurgitation jets were made visible, three-dimensional data were acquired to segment the mitral valves and the accurate orientation of TEER devices was enabled. However, physicians reported that navigation was sometimes more complex due to missing typical landmarks such as the aortic valve. Furthermore, high background noise within the images was observed, caused by air bubbles within the blood-mimicking fluid. An additional limitation of this approach was the absence of fluoroscopy during TEER to support navigation. In this study, fluoroscopy was replaced by an atrial live video streaming. This eased the setup and avoided radiation; however, imaging was different. Video observation provided much more information about the left atrium and the clip, but no information about the orientation of the clip once the mitral valve orifice is passed. In the future, this approach may be improved by using modalities such as electromagnetic tracking to replace fluoroscopy.

4.1.5 Assessing the hemodynamics quantitatively (MVS-R6)

The capacity to quantitatively evaluate the hemodynamic condition (MVS-R6) within the left heart is pivotal for comparing techniques or for monitoring a physician's training progress. Partially, this can be done by TEE. However, further insights into the hemodynamics were enabled by additional flow and pressure sensors. While the use of sensors does not require specialized expertise, the performance of TEE requires the presence of a skilled physician and an expensive ultrasound system. In the clinical daily routine, physicians and hardware are usually bound. Consequently, achieving independence from these factors would increase the accessibility and availability of training possibilities. Existing simulators with hemodynamic settings either lack flow and pressure data (Gollmann-Tepeköylü et al., 2018) or only provide pressure measurements without flow data (Ginty et al., 2018; Boone et al., 2019). In contrast, the here-developed simulator incorporates pressure and flow sensors which allow for recording and real-time monitoring and consequently enhance the depth of observation during simulations. Systolic pressures, cardiac output, and measurements such as regurgitation volume or regurgitation fraction were successfully determined. While at this point the regurgitation volume had to be calculated from different values, a specific flow sensor could be integrated in the future to increase the accuracy of the flow measurement through the mitral valve.

4.2 Shortcomings of the flow convergence method

Besides developing and validating the mitral valve simulator for training and planning, it was also used to assess the accuracy of the flow convergence method in a hemodynamic reproducible *in-vitro* environment. Quantitative assessment was done by juxtaposing the flow convergence method with PIV to classify mitral regurgitation by measuring the regurgitation volume produced by different mitral valve phantoms.

4.2.1 Influence of orifice shape and size

Regardless of the opening geometry and size, the regurgitation volume determined by physicians with the flow convergence methods was underestimated when compared to PIV for eight out of nine mitral valve phantoms. This finding aligns well with the findings of Lancellotti et al. (2010), Iwakura et al. (2006), and Coisne et al. (2002) that recognised underestimation of up to 44.2 %. Within this thesis, it was found that for large geometries, such as 'pointed oval l', the underestimation was as much as 51.7 %.

Due to this underestimation, the mitral regurgitation might be classified as mild instead of moderate, potentially affecting therapy decisions. The difference between the two methods was comparably small for mild mitral regurgitation and can probably be neglected. For moderate mitral regurgitation, this potentially leads to wrong diagnosis and decision-making. While for the small- and medium-sized phantoms, which induced mild mitral regurgitation, the deviation between the flow convergence method and PIV with 1.4-5.4 ml was small, the deviation for the large phantoms, which caused moderate mitral regurgitation, was between 11.6 and 23.2 ml. This leads to the assumption that a larger orifice shape leads to an increased underestimation of mitral regurgitation determined by the flow convergence method. Furthermore, it was found that the pointed oval shape produced the greatest percentage deviation. For example, for the similarly sized large phantoms, the deviation was 51.7 % for the pointed oval-shaped, 39.2 % for the circle-shaped, and 32.6 % for the drop-shaped.

Further investigation is necessary to understand the impact of size and shape on underestimation, including more mitral valve models producing moderate and severe mitral regurgitation. Additionally, it would be of potential interest to decrease the Nyquist limit for the flow convergence method. This would result in an increased PISA. An increased PISA has a rather hemispherical shape, which is necessary to determine the regurgitation volume. However, the shape of the PISA is difficult to detect during echocardiography, especially because the ultrasound shows only one-dimensional velocities. A possible approach to investigate would be to define a certain PISA radius and "measure" the required Nyquist-limit, instead of vice-versa.

4.2.2 Influence of the observer

Besides the influence of size and shape on the regurgitation volume, the correlation with the inter-observer variability was examined. For all small and medium mitral valves, the variability was negligible. For the circular orifice shapes the variability was even negligible for all sizes. For the large-sized pointed oval and drop the variability could be observed. This raises the question of how robust the flow convergence method is for elliptical or more complex orifice shapes. Weight is added to this question considering that complex orifice shapes might be predominant within the patient (Lancellotti et al., 2010). To evaluate this effect further, more mitral valve phantoms with larger pointed oval and drop orifices should be examined.

While it was shown that the inter-observer variability increases for more complex orifice shapes, drop and pointed oval, it was only demonstrated that the pointed oval shape leads to a higher underestimation of regurgitation volume by the flow convergence method compared to circular-shaped orifices. Considering the big underestimation of regurgitation volume in large orifices the inter-observer variability and influence of shape plays only a subordinate role.

The underestimation of the regurgitation volume and the inter-observer variability show the limitations of quantifying mitral regurgitation by using the flow convergence method. Consequently, these limitations must not be overlooked when making diagnoses and treatment decisions.

4.3 Simulation of thoracic endovascular aortic repair in an aortic flow-loop

In this study, a hemodynamic aortic flow-loop is developed to assess, train, and plan TEVAR interventions to treat TBAD on patient-specific phantoms. In contrast to existing simulators or aortic phantoms shown in Table 1.7, the flow-loop presented here meets all defined requirements. The aortic phantom comprises the entire aorta, namely the thoracic ascending and descending aorta, aortic arch, and abdominal aorta, including the major aortic branches truncus brachiocephalicus, arteria communis sinistra, arteria subclavia sinistra, truncus coeliacus, arteria mesenterica superior, arteria renalis sinistra and dextra, and the arteriae iliacae communes sinistra and dextra (AS-R1). Furthermore, it closely replicates a patient-specific anatomy and pathology (AS-R2).

The simulator is compatible with CTA and DSA, medical imaging technologies the patient is subjected to in clinical routine to diagnose TBAD and to treat it with TEVAR (AS-R3). The flow-loop provides anatomically correct femoral access for catheters and TEVAR devices to enter (AS-R4). Furthermore, a pulsatile pump forms the heart of the flow-loop and gener-

ates a hemodynamic environment replicating known *in-vivo* conditions for realistic training conditions (AS-R5).

4.3.1 Patient-specific phantom of the aorta at full length (AS-R1 + AS-R2)

The TEVAR procedure impacts the entire aorta, extending from the aortic arch to the arteria iliaca communis. More precisely, the TEVAR device accesses the human body through an introducer sheath through the arteria femoralis, enters the aorta via the arteria iliaca communis, and is guided through the true aortic lumen. The proximal landing zone may be located within the aortic arch. In addition, the stent-graft potentially remodels the aorta or occludes aortic branches. Therefore, an aortic phantom encompassing both the thoracic and abdominal aorta is required to perform a realistic TEVAR procedure.

Existing simulators, however, cover only parts of the aorta, for instance only the thoracic aorta (Rudenick et al., 2013; Rynio et al., 2019; Schmauss et al., 2014; Urbina et al., 2016; Ramella et al., 2022; Arakawa et al., 2022), or the abdominal aorta (Cloonan et al., 2014; Mix et al., 2018; Meess et al., 2017; Sommer et al., 2018; Tong et al., 2020; Little et al., 2022; Torres and de Luccia, 2017). While abdominal phantoms allow for the assessment and training to treat abdominal aortic aneurysms, they do not enable the training of TEVAR procedures. On the other hand, guiding a catheter or stent-graft through the aorta and observing effects on the abdominal aorta is not possible with phantoms covering solely the thoracic aorta, as done by Rynio et al. (2019), Arakawa et al. (2022), and Ramella et al. (2022).

The flow-loop presented here includes a phantom covering both the thoracic and abdominal aorta and thus allowed for successful guidance of catheters and the TEVAR device, performance of TEVAR, and the observation of flow effects in all aortic branches. Similarly, Chung et al. (2000a,b) developed an aortic simulator covering both the thoracic and abdominal aorta, including major aortic branches. However, this simulator cannot model both patient-specific anatomy and pathology. The phantom used in this study replicates patient-specific anatomy and pathology and thus enables personalized training or planning for complex cases. To the best of my knowledge, the aortic flow-loop presented here is the first to combine patient-specific anatomy (AS-R1) while modeling the aorta at its full length (AS-R2).

4.3.2 Integrating invasive medical imaging (AS-R3)

A central aim of this part of the project was to establish a setup for training and planning TEVAR interventions. An essential aspect of preparing a TEVAR procedure in clinical practice is to assess the CTA scans of the patient's aorta and determine the best approach for the therapy. Therefore, the aortic simulator must be compatible with CT scanners (AS-R3) and contrast agent. Studies by Little et al. (2022) and Ramella et al. (2022) demonstrated the compatibility of their simulators with CT scanners, but they did not use contrast agents, and their phantoms were not connected to a flow-loop. This approach simplifies the setup, as there is

no need to position a flow-loop next to the CT scanner, which could be a major obstacle due to the movement of the scanner table and the potential entanglement of tubes.

However, this work demonstrated that the use of contrast agent in combination with flow is highly beneficial for the quality of CTA images. Due to its higher density, the contrast agent tends to separate from the blood-mimicking fluid and accumulate at the bottom of the vessel, when flow is absent. Conversely, flow allows the contrast agent to remain well-distributed within the blood-mimicking fluid. Furthermore, it was observed that water serves as a feasible extra-vascular medium compared to Laponite, which encapsulated air and caused image disturbances. Additionally, the study revealed that an increase in radiation reduces the noise in the images. These findings present a setup of the simulator and settings of the CT scanner, which allow for high image quality and consequently for planning of TEVAR procedures at the simulator. While a CT-scanner-compatible flow-loop was provided, for future experiments, all connections to the aortic phantom should come from the distal end to further simplify the positioning inside the CT scanner.

The simulator not only needs to be compatible with CTA but also with DSA to allow for monitoring during TEVAR (AS-R3). While both imaging methods involve X-ray radiation passing through the phantom, they have differences. In CTA scans, the table of the scanner moves, whereas in DSA, it remains stationary. During CTA scans the contrast agent must be evenly distributed inside the phantom for the entire time. On the other hand, DSA requires the contrast agent to be confined locally and for a limited period within the phantom. To address this challenge the proposed simulator used three liters of blood-mimicking fluid held in the reservoir during the TEVAR and DSA procedures. This design allows vascular surgeons to locally administer the contrast agent to visualize flow patterns in DSA while allowing the contrast agent to dissolve in the blood-mimicking fluid over time to reduce its concentration and become invisible in the following scans.

While Meess et al. (2017) demonstrated successful DSA performance using their abdominal aorta phantom, this work stands out as the first to achieve successful DSA performance with a phantom encompassing the entire aorta and even the thoracic aorta. Moreover, no previous study has presented a combination of TEVAR and DSA, even though DSA guidance and assessment during TEVAR is essential. It was shown that guidance of the pigtail catheter was feasible and imaging is similar to interventions made on patients in the operating room. Due to the DSA, it was not only possible to guide the pigtail catheter through the true lumen of the aorta to its supposed destination, but also to identify (re-)entries to the false lumen, and to assess the flow through the (re-)entries and aortic branches.

4.3.3 Enabling access to perform thoracic endovascular aortic repair (AS-R4)

TEVAR devices enter the human body through access at a femoral artery. This access seals the blood vessel to prevent blood from leaving and allows devices such as catheters and

TEVAR devices to enter. This work showed that it was possible to install an introducer sheath in the flow-loop (AS-R4). This sheath successfully provided access for different catheters and the TEVAR device to reach their destination within the aorta. While Chung et al. (2000b), Tong et al. (2020), and Rynio et al. (2019) applied their stent-grafts with the phantom detached from the flow-loop, Meess et al. (2017), Arakawa et al. (2022), and Ramella et al. (2022) applied their stent-grafts through an introducer sheath as accomplished in this study. However, the aortic phantom of Ramella et al. (2022) covers only the thoracic aorta, is not patient-specific, and does not replicate any pathology. The abdominal access, instead of a femoral, presented in their work, does not replicate a physiological situation. Arakawa et al. (2022) chose an access from the ascending aorta, where in the human body the heart would be located. This approach cannot be compared to clinical routine. The access established by Meess et al. (2017) models an *in-vivo* situation and can be compared to the results achieved in this work, even though the target destination of the abdominal aorta is significantly closer to the arteria femoralis than the thoracic aorta. While TEVAR was feasible, a limitation persisted. In typical TEVAR procedures, the introducer sheath is usually advanced further into the aorta, even up to the renal artery. In the proposed setup, the introducer sheath was only advanced as far as the common iliac artery. Future work will aim to achieve even more realistic access to enhance the pushability of catheters and TEVAR devices.

4.3.4 Creating a realistic hemodynamic environment within the aorta (AS-R5)

A realistic hemodynamic environment is crucial to provide a simulator for personalized and realistic training, planning, and evaluation of new therapeutic approaches (AS-R5). Without this environment, it is challenging to accurately assess the effects and consequences of interventions, such as TEVAR. The proposed simulator provides physiological pressures and flows through the aorta, enabling the observation and evaluation of the treatment's impact. For instance, the simulator allows for the assessment of flow reduction through the left subclavian artery, which can be attributed to partial coverage by the stent-graft. The decrease in flow, after TEVAR, through the left renal artery originating from the false lumen might be due to reduced flow through the false lumen. Conversely, the increase in flow through the right common iliac artery is explained by the augmented flow through the true lumen due to TEVAR. Such observations empower vascular surgeons with a powerful tool to plan interventions and evaluate potential risks. However, existing simulators with a hemodynamic environment have limitations. Some do not permit personalized training (Chung et al., 2000b; Ramella et al., 2022), while others do not cover the thoracic aorta (Torres and de Luccia, 2017; Meess et al., 2017). Additionally, some simulators lack a flow-loop that adequately represents realistic access to the aorta (Arakawa et al., 2022). Moreover, except for the work by Chung et al. (2000b), no simulator has integrated the full length of the aorta, highlighting the significance of the proposed simulator's ability to measure pre- and post-interventional flows. The suggested flow-loop offered a physiological hemodynamic setting, particularly during systole. Subsequent efforts will incorporate peripheral resistance, such as a higher elevated reservoir to also generate physiological diastolic pressures of 80 mmHg. Addition-

ally, including a compliance chamber between the aortic valve and the aortic phantom is recommended to support the windkessel function and mitigate the pressure peak resulting from the closure of the aortic valve.

4.4 Conclusion

Within the scope of this thesis, a new mitral valve simulator and a novel aortic flow-loop were developed and validated. These simulators provide major advantages over existing technologies, including a reproducible hemodynamic environment across the mitral valve and along the aorta, to evaluate mitral valve insufficiency and TBAD, and to train MIMVS and TEER on patient-specific phantoms.

Cardiac surgeons have the opportunity to train and compare different techniques in MIMVS such as annuloplasty or chordaeplasty. Cardiologists may familiarize themselves with transcatheter systems such as TEER. The proposed system allows both groups of physicians to evaluate the effects of different mitral valve repair techniques on the hemodynamics within the left heart by using TEE, pressure, and flow sensors, or visual observation. Similarly, vascular surgeons can apply the aortic flow-loop to familiarize themselves with all the procedural steps of a TEVAR.

Personalized pre-interventional training is also enabled with the proposed simulators. This allows physicians to determine the best possible therapy for their patients and to familiarize themselves with the upcoming intervention.

The developed simulators provide reproducible *in-vitro* environments which pave the way for future research, such as the evaluation of flow patterns, the development of new therapy technologies, or the assessment of current diagnostic procedures such as provided in Section 1.3.3.

Besides the development and validation of the simulators, the flow convergence method, as a diagnostic procedure, was juxtaposed with PIV within the mitral valve simulator to evaluate its accuracy. I demonstrated that the flow convergence method underestimates the regurgitation volume. While the effect occurred for all orifice shapes, the effect was more pronounced with complex shapes and increased with increasing orifice size. Inter-observer variability increased with the complexity of the orifice shape and its size.

These findings demonstrate that the flow convergence method is highly limited in determining the severity of mitral regurgitation, which must be considered during diagnosis and decision-making. Therefore, more efforts are necessary to investigate the mechanisms of the flow convergence method and to increase its robustness.

In summary, the two developed simulators offer a unique opportunity for training and planning of mitral valve repair and TEVAR procedures. Additionally, these simulators serve as a tool for studying hemodynamics across the mitral valve and within the aorta using an *in-vitro* model.

5 Summary

Minimally invasive mitral valve surgery, transcatheter edge-to-edge repair, and thoracic endovascular aortic repair are highly complex procedures to treat mitral valve insufficiency and type B aortic dissection, respectively. Years of training are required to master these techniques and to maintain their performance at high level. However, modalities for training and interventional planning are limited as *in-vivo* training on animals is cost-intensive and of ethical concern, and existing *in-vitro* tools lack an *in-vivo*-like environment.

Within the scope of this thesis, novel hemodynamic simulators were developed and evaluated for their ability to model mitral valve insufficiency and type B aortic dissection. In addition, the simulators were assessed as tools for training and planning the corresponding treatment procedures.

A mitral valve simulator is presented, in which different, potentially patient-specific mitral valves can be installed. The simulator enables evaluation of the valve pathology and its subsequent treatment using either minimally invasive mitral valve surgery or transcatheter edge-to-edge repair under transesophageal echocardiography guidance. Importantly, the obtained outcomes following the interventions can each be assessed qualitatively and quantitatively, thereby allowing physicians to gain experience, plan interventions at a patient-specific level, and potentially support the treatment decision. Due to the realistic environment provided by the simulator, it may also serve as a research tool to examine and refine therapeutic procedures.

For initial research purposes, the developed mitral valve simulator was employed to investigate the accuracy of the flow convergence method. Regurgitation volumes generated by different mitral valve models were measured using the flow convergence method and particle image velocimetry. Mitral valve models encompassed different orifice shapes, including a pointed oval, drop, and circle of three different sizes. A comparison of the two techniques revealed that the flow convergence method underestimated the regurgitation volume, particularly for large orifices. Complex orifice shapes such as the pointed oval and drop led to larger inter-observer variabilities than circular orifices. While the shape affected inter-observer variability, it did not influence the underestimation of regurgitation volumes. Besides highlighting the limitations of the flow convergence method, this study demonstrates the utility of the mitral valve simulator as a research modality in the field of mitral regurgitation.

Similar to the mitral valve simulator, a flow-loop is presented, which allows for training, planning, and research of thoracic endovascular aortic repair to treat type B aortic dissection. The flow-loop was developed to incorporate entire potentially patient-specific aortic phantoms. It allows for evaluation of the phantom by computed tomography angiography, as well as the performance of thoracic endovascular aortic repair under digital subtraction angiography guidance. Moreover, flow and pressure can be assessed to evaluate potential consequences on aortic branches following the repair. The presented flow-loop enables vascular surgeons to gain experience, plan interventions, and to potentially investigate type B aortic dissections and their treatments.

Collectively, the proposed mitral valve simulator is the first to provide a realistic hemodynamic environment *in-vitro* that allows for the performance of both minimally invasive mitral valve surgery and transcatheter edge-to-edge repair within a single device. Similarly, the developed aortic simulator pioneers the integration of an entire patient-specific aorta in a hemodynamic flow-loop that enables the performance of thoracic endovascular repair while maintaining compatibility with clinically relevant medical imaging modalities. In conclusion, these distinctive features position the novel simulators as valuable tools for research as well as comprehensive training and patient-specific planning of interventions.

6 Zusammenfassung

Die minimalinvasive Mitralklappenchirurgie, die kathetergestützte Edge-to-Edge-Therapie und die thorakale endovaskuläre Aortenreparatur sind hochkomplexe Verfahren zur Behandlung der Mitralklappeninsuffizienz bzw. der Typ B Aortendissektion. Jahrelanges Training ist erforderlich, um diese Techniken zu beherrschen. Möglichkeiten diese Eingriffe zu trainieren und zu planen sind allerdings begrenzt, denn zum einen ist das Training an Tieren kostenintensiv und birgt ethische Bedenken und zum anderen mangelt es den vorhandenen *in-vitro*-Simulatoren an einer *in-vivo*-ähnlichen Umgebung.

Im Rahmen dieser Arbeit wurden neuartige hämodynamische Simulatoren entwickelt und hinsichtlich ihrer Fähigkeit zur Modellierung der Mitralklappeninsuffizienz und der Typ B Aortendissektion untersucht. Darüber hinaus wurde evaluiert, inwiefern sich die Simulatoren als Werkzeuge für Training und Planung der entsprechenden Behandlungsverfahren eignen.

In dieser Arbeit wird ein Mitralklappen-Simulator vorgestellt, in den verschiedene, potenziell patientenspezifische Mitralklappen eingebaut werden können. Der Simulator ermöglicht es, die Klappenpathologie zu analysieren, sowie deren anschließende Behandlung entweder durch minimalinvasive Mitralklappenchirurgie oder kathetergestützte Edge-to-Edge-Therapie unter transösophagealer Echokardiographie. Herauszustellen ist, dass die durch die Eingriffe erzielten Ergebnisse sowohl qualitativ als auch quantitativ bewertet werden können, was ermöglicht, dass Ärzte praktische Erfahrungen sammeln können, Eingriffe auf patientenspezifischer Ebene geplant werden können und somit möglicherweise auch die Behandlungsentscheidung unterstützt werden kann. Aufgrund des realistischen Umfelds, das der Simulator bietet, kann er auch dazu dienen, therapeutische Verfahren zu erforschen und weiterzuentwickeln.

In einer ersten Forschungsstudie wurde der entwickelte Mitralklappensimulator eingesetzt, um die Genauigkeit der Flusskonvergenzmethode zu untersuchen. Die von verschiedenen Mitralklappenmodellen erzeugten Regurgitationsvolumina wurden mithilfe der Flusskonvergenzmethode und mittels Particle Image Velocimetry gemessen. Verschiedene Öffnungsformen in drei verschiedenen Größen, darunter ein spitzes Oval, ein Tropfen und ein Kreis stellten die Mitralklappenmodelle dar. Der Vergleich beider Techniken zeigte, dass die Flusskonvergenzmethode insbesondere bei größeren Öffnungen das Regurgitationsvolumen als zu gering einschätzt. Bei komplexen Öffnungsformen wie dem spitzen Oval und dem Tropfen war die Variabilität zwischen Beobachtern größer als bei der kreisförmigen Öffnung.

Während die Form die Variabilität zwischen den Beobachtern beeinflusste, hatte sie keinen Einfluss auf die zu geringe Einschätzung des Regurgitationsvolumens. Diese Studie zeigt nicht nur die Grenzen der Flusskonvergenzmethode auf, sondern auch den Wert des Mitralklappensimulators als Forschungsinstrument auf dem Gebiet der Mitralinsuffizienz.

Analog zum Mitralklappensimulator wird ein Aortensimulator vorgestellt, der das Training, die Planung und die Erforschung der thorakalen endovaskulären Aortenreparatur zur Behandlung der Typ B Aortendissektion ermöglicht. Der Simulator wurde entwickelt, um vollständige, potenziell patientenspezifische, Aortenphantome einzubinden. Dieser ermöglicht die Evaluierung des Phantoms mittels Computertomographie-Angiographie sowie die Durchführung einer thorakalen endovaskulären Aortenreparatur unter digitaler Subtraktionsangiographie. Darüber hinaus können Fluss und Druck erfasst werden, um mögliche Auswirkungen der Reparatur auf die Aortenäste zu beurteilen. Der vorgestellte Aortensimulator ermöglicht es Gefäßchirurgen praktische Erfahrungen zu sammeln, Eingriffe zu planen und in Zukunft Typ B Aortendissektionen und deren Behandlung genauer zu erforschen.

Insgesamt ist der vorgeschlagene Mitralklappensimulator der erste, der eine realistische hämodynamische *in-vitro* Umgebung bereitstellt, die die Durchführung sowohl einer minimalinvasiven Mitralklappenoperation als auch einer kathetergestützten Edge-to-Edge-Therapie in einem einzigen Gerät ermöglicht. In ähnlicher Weise leistet der entwickelte Aortensimulator Pionierarbeit bei der Integration einer vollständigen patientenspezifischen Aorta in einen hämodynamischen Strömungskreislauf, der die Durchführung von thorakalen endovaskulären Reparaturen ermöglicht und gleichzeitig die Kompatibilität mit klinisch relevanten medizinischen Bildgebungsmodalitäten ermöglicht. Diese Eigenschaften machen die neuartigen Simulatoren zu wertvollen Werkzeugen für die Forschung sowie für umfassendes Training und die patientenspezifische Planung von Eingriffen.

7 Bibliography

adh30. Wiggers diagram 2, 2016. URL https://commons.wikimedia.org/wiki/File:Wiggers_Diagram_2.svg.

R. J. Adrian and J. Westerweel. *Particle image velocimetry*, volume 30 of *Cambridge aerospace series*. Cambridge Univ. Press, Cambridge, 2011. ISBN 9780521440080.

I. Akin, S. Kische, T. C. Rehders, H. Schneider, H. Ince, and C. A. Nienaber. Tevar: the solution to all aortic problems? *Herz*, 36(6):539–547, 2011. doi: 10.1007/s00059-011-3500-1.

I. Akin, S. Kische, H. Ince, and C. Nienaber. Penetrating aortic ulcer, intramural hematoma, acute aortic syndrome: when to do what. *The Journal of cardiovascular surgery*, 53(1 Suppl 1):83–90, 2012.

D. B. Alfson and S. W. Ham. Type b aortic dissections: Current guidelines for treatment. *Cardiology clinics*, 35(3):387–410, 2017. doi: 10.1016/j.ccl.2017.03.007.

E. E. Apostolakis and N. G. Baikoussis. Methods of estimation of mitral valve regurgitation for the cardiac surgeon. *Journal of cardiothoracic surgery*, 4:34, 2009. doi: 10.1186/1749-8090-4-34.

M. Arakawa, H. Sumikura, H. Okamura, A. Miyagawa, A. Homma, and A. Yamaguchi. A three-dimensional biomodel of type a aortic dissection for endovascular interventions. *Journal of artificial organs : the official journal of the Japanese Society for Artificial Organs*, 25(2):125–131, 2022. doi: 10.1007/s10047-021-01294-0.

P. J. Bártolo. *Stereolithography*. Springer US, Boston, MA, 2011. ISBN 978-0-387-92903-3. doi: 10.1007/978-0-387-92904-0.

P. J. Bartolo and J. Gaspar. Metal filled resin for stereolithography metal part. *CIRP Annals*, 57(1):235–238, 2008. ISSN 00078506. doi: 10.1016/j.cirp.2008.03.124.

N. Bhattacharjee, A. Urrios, S. Kang, and A. Folch. The upcoming 3d-printing revolution in microfluidics. *Lab on a chip*, 16(10):1720–1742, 2016. doi: 10.1039/c6lc00163g.

B. Bhushan and M. Caspers. An overview of additive manufacturing (3d printing) for microfabrication. *Microsystem Technologies*, 23(4):1117–1124, 2017. ISSN 0946-7076. doi: 10.1007/s00542-017-3342-8.

N. Boone, J. Moore, O. Ginty, D. Bainbridge, T. M. Peters, and M. Eskandari. A dynamic mitral valve simulator for surgical training and patient specific preoperative planning. *Medical Imaging 2019: Image-Guided Procedures, Robotic Interventions, and Modeling*, page 16, 2019. doi: 10.1117/12.2509818. URL https://www.

spiedigitallibrary.org/conference-proceedings-of-spie/10951/2509818/A-dynamic-mitral-valve-simulator-for-surgical-training-and-patient/10.1117/12.2509818.full.

A. Boschetto, V. Giordano, and F. Veniali. Modelling micro geometrical profiles in fused deposition process. *The International Journal of Advanced Manufacturing Technology*, 61 (9-12):945–956, 2012. ISSN 0268-3768. doi: 10.1007/s00170-011-3744-1.

W. Bothe, D. C. Miller, and T. Doenst. Sizing for mitral annuloplasty: where does science stop and voodoo begin? *The Annals of thoracic surgery*, 95(4):1475–1483, 2013. doi: 10.1016/j.athoracsur.2012.10.023.

R. Brandes, F. Lang, and R. F. Schmidt. *Physiologie des Menschen*. Springer Berlin Heidelberg, Berlin, Heidelberg, 2019. ISBN 978-3-662-56467-7. doi: 10.1007/978-3-662-56468-4.

L. Burger, L. Sharan, R. Karl, C. Wang, M. Karck, R. de Simone, I. Wolf, G. Romano, and S. Engelhardt. Comparative evaluation of three commercially available markerless depth sensors for close-range use in surgical simulation. *International journal of computer assisted radiology and surgery*, 18(6):1109–1118, 2023. doi: 10.1007/s11548-023-02887-1.

A. F. Carpentier. *Carpentier's reconstructive valve surgery: From valve analysis to valve reconstruction*. Saunders Elsevier, Maryland Heights, Mo, 2010. ISBN 9780721691688.

S. W. Chen, K. B. Lee, M. A. Napolitano, A. E. Murillo-Berlioz, A. P. Sattah, S. Sarin, and G. Trachiotis. Complications and management of the thoracic endovascular aortic repair. *Aorta (Stamford, Conn.)*, 8(3):49–58, 2020. ISSN 2325-4637. doi: 10.1055/s-0040-1714089.

A. K. Chhatriwalla, S. Vemulapalli, M. Szerlip, S. Kodali, R. T. Hahn, J. T. Saxon, M. J. Mack, G. Ailawadi, J. Rymer, P. Manandhar, A. S. Kosinski, and P. Sorajja. Operator experience and outcomes of transcatheter mitral valve repair in the united states. *Journal of the American College of Cardiology*, 74(24):2955–2965, 2019. doi: 10.1016/j.jacc.2019.09.014.

J. Chikwe, N. Toyoda, A. C. Anyanwu, S. Itagaki, N. N. Egorova, P. Boateng, A. El-Eshmawi, and D. H. Adams. Relation of mitral valve surgery volume to repair rate, durability, and survival. *Journal of the American College of Cardiology*, 2017. doi: 10.1016/j.jacc.2017.02.026.

J. W. Chung, C. Elkins, T. Sakai, N. Kato, T. Vestring, C. P. Semba, S. M. Slonim, and M. D. Dake. True-lumen collapse in aortic dissection: part i. evaluation of causative factors in phantoms with pulsatile flow. *Radiology*, 214(1):87–98, 2000a. ISSN 0033-8419. doi: 10.1148/radiology.214.1.r00ja3287.

J. W. Chung, C. Elkins, T. Sakai, N. Kato, T. Vestring, C. P. Semba, S. M. Slonim, and M. D. Dake. True-lumen collapse in aortic dissection: part ii. evaluation of treatment methods in phantoms with pulsatile flow. *Radiology*, 214(1):99–106, 2000b. ISSN 0033-8419. doi: 10.1148/radiology.214.1.r00ja3499.

A. J. Cloonan, D. Shahmirzadi, R. X. Li, B. J. Doyle, E. E. Konofagou, and T. M. McGloughlin. 3d-printed tissue-mimicking phantoms for medical imaging and computational validation applications. *3D printing and additive manufacturing*, 1(1):14–23, 2014. ISSN 2329-7662. doi: 10.1089/3dp.2013.0010.

D. Coisne, D. Erwan, L. Christiaens, P. Blouin, J. Allal, and R. Barraine. Quantitative assessment of regurgitant flow with total digital three-dimensional reconstruction of color doppler flow in the convergent region: in vitro validation. *Journal of the American Society of Echocardiography : official publication of the American Society of Echocardiography*, 15 (3):233–240, 2002. doi: 10.1067/mje.2002.117901.

J. S. Corvera. Acute aortic syndrome. *Annals of cardiothoracic surgery*, 5(3):188–193, 2016. ISSN 2225-319X. doi: 10.21037/acs.2016.04.05.

B. Del Forno, M. de Bonis, E. Agricola, F. Melillo, D. Schiavi, A. Castiglioni, M. Montorfano, and O. Alfieri. Mitral valve regurgitation: a disease with a wide spectrum of therapeutic options. *Nature reviews. Cardiology*, 17(12):807–827, 2020. doi: 10.1038/s41569-020-0395-7.

A. K. Dixon and P. Dendy. Spiral ct: how much does radiation dose matter? *Lancet (London, England)*, 352(9134):1082–1083, 1998. doi: 10.1016/S0140-6736(05)79751-8.

Dtrx. Tomography, illustration of the basic principle, 2009. URL `https://commons.wikimedia.org/wiki/File:TomographyPrinciple_Illustration.png`.

K. S. Dujardin, M. Enriquez-Sarano, K. R. Bailey, R. A. Nishimura, J. B. Seward, and A. J. Tajik. Grading of mitral regurgitation by quantitative doppler echocardiography: calibration by left ventricular angiography in routine clinical practice. *Circulation*, 96(10):3409–3415, 1997. doi: 10.1161/01.cir.96.10.3409.

A. El Sabbagh, Y. N. V. Reddy, and R. A. Nishimura. Mitral valve regurgitation in the contemporary era: Insights into diagnosis, management, and future directions. *JACC. Cardiovascular imaging*, 11(4):628–643, 2018. doi: 10.1016/j.jcmg.2018.01.009.

S. Engelhardt, S. Sauerzapf, B. Preim, M. Karck, I. Wolf, and R. de Simone. Flexible and comprehensive patient-specific mitral valve silicone models with chordae tendineae made from 3d-printable molds. *International journal of computer assisted radiology and surgery*, 14(7):1177–1186, 2019. doi: 10.1007/s11548-019-01971-9.

M. Enriquez-Sarano, J.-F. Avierinos, D. Messika-Zeitoun, D. Detaint, M. Capps, V. Nkomo, C. Scott, H. V. Schaff, and A. J. Tajik. Quantitative determinants of the outcome of asymptomatic mitral regurgitation. *The New England journal of medicine*, 352(9):875–883, 2005. doi: 10.1056/NEJMoa041451.

M. Enriquez-Sarano, C. W. Akins, and A. Vahanian. Mitral regurgitation. *Lancet (London, England)*, 373(9672):1382–1394, 2009. doi: 10.1016/S0140-6736(09)60692-9.

R. Erbel, V. Aboyans, C. Boileau, E. Bossone, R. Di Bartolomeo, H. Eggebrecht, A. Evangelista, V. Falk, H. Frank, O. Gaemperli, M. Grabenwöger, A. Haverich, B. Iung, A. J. Manolis, F. Meijboom, C. A. Nienaber, M. Roffi, H. Rousseau, U. Sechtem, P. A. Sirnes, R. S. von Allmen, and C. J. M. Vrints. 2014 esc guidelines on the diagnosis and treatment of aortic diseases: Document covering acute and chronic aortic diseases of the thoracic and abdominal aorta of the adult. the task force for the diagnosis and treatment of aortic diseases of the european society of cardiology (esc). *European heart journal*, 35(41):2873–2926, 2014. doi: 10.1093/eurheartj/ehu281.

V. Falk, D. C. H. Cheng, J. Martin, A. Diegeler, T. A. Folliguet, L. W. Nifong, P. Perier, E. Raanani, J. M. Smith, and J. Seeburger. Minimally invasive versus open mitral valve surgery: a consensus statement of the international society of minimally invasive coronary surgery (ismics) 2010. *Innovations (Philadelphia, Pa.)*, 6(2):66–76, 2011. doi: 10.1097/IMI.0b013e318216be5c.

S. Fischer, G. Romano, L. Sharan, G. Warnecke, D. Mereles, M. Karck, R. de Simone, and S. Engelhardt. Surgical rehearsal for mitral valve repair: Personalizing surgical simulation by 3d printing. *The Annals of thoracic surgery*, 115(4):1062–1067, 2023. doi: 10.1016/j.athoracsur.2022.12.039.

N. Flint, M. J. Price, S. H. Little, G. B. Mackensen, N. C. Wunderlich, M. Makar, and R. J. Siegel. State of the art: Transcatheter edge-to-edge repair for complex mitral regurgitation. *Journal of the American Society of Echocardiography : official publication of the American Society of Echocardiography*, 34(10):1025–1037, 2021. doi: 10.1016/j.echo.2021.03.240.

T. Flohr. Ct systems. *Current Radiology Reports*, 1(1):52–63, 2013. doi: 10.1007/s40134-012-0005-5.

C. Frerker, N. Karam, R. T. Hahn, H. Thiele, G. W. Stone, H. Treede, and J. Hausleiter. New esc/eacts guideline recommendations for the treatment of secondary mitral regurgitation: reflections on the evidence. *European journal of heart failure*, 24(5):746–749, 2022. doi: 10.1002/ejhf.2497.

K. Friedrich and R. Walter, editors. *Structure and properties of additive manufactured polymer components*. Woodhead publishing series in composites science and engineering. Woodhead Publishing an imprint of Elsevier, Duxford and Cambridge, MA and Kidlington, 2020. ISBN 978-0-12-819535-2.

A. Gallarello, A. Palombi, G. Annio, S. Homer-Vanniasinkam, E. de Momi, G. Maritati, R. Torii, G. Burriesci, and H. A. Wurdemann. Patient-specific aortic phantom with tunable compliance. *Journal of Engineering and Science in Medical Diagnostics and Therapy*, 2(4), 2019. ISSN 2572-7958. doi: 10.1115/1.4044611.

Y. Gao, Y. Song, X. Yin, W. Wu, L. Zhang, Y. Chen, and W. Shi. Deep learning-based digital subtraction angiography image generation. *International journal of computer assisted radiology and surgery*, 14(10):1775–1784, 2019. doi: 10.1007/s11548-019-02040-x.

O. A. García-Villarreal. Reparación valvular mitral transcatéter “borde a borde”: influencia del sesgo en estudios aleatorizados. *Gaceta medica de Mexico*, 158(5):323–327, 2022. ISSN 0016-3813. doi: 10.24875/GMM.M22000702.

G. F. Gebhart and R. F. Schmidt. *Encyclopedia of Pain*. Springer Berlin Heidelberg, Berlin, Heidelberg, 2013. ISBN 978-3-642-28752-7. doi: 10.1007/978-3-642-28753-4.

S. Gennai, N. Leone, L. A. M. Bartolotti, F. Andreoli, G. Pizzarelli, and R. Silingardi. Learning curve and long-term outcomes of thoracic endovascular repair with the relay stent-graft. *Journal of endovascular therapy : an official journal of the International Society of Endovascular Specialists*, page 15266028221136450, 2022. doi: 10.1177/15266028221136450.

O. K. Ginty, J. M. Moore, Y. Xu, W. Xia, S. Fujii, D. Bainbridge, T. M. Peters, B. B. Kiaii, and M. W. A. Chu. Dynamic patient-specific three-dimensional simulation of mitral repair: Can we practice mitral repair preoperatively? *Innovations (Philadelphia, Pa.)*, 13(1):11–22, 2018. doi: 10.1097/IMI.0000000000000463.

O. K. Ginty, J. T. Moore, M. Eskandari, P. Carnahan, A. Lasso, M. A. Jolley, M. Monaghan, and T. M. Peters. Dynamic, patient-specific mitral valve modelling for planning transcatheter repairs. *International journal of computer assisted radiology and surgery*, 14(7):1227–1235, 2019. doi: 10.1007/s11548-019-01998-y.

E. Girdauskas, J. Pausch, E. Harmel, T. Gross, C. Detter, C. Sinning, J. Kubitz, and H. Reichenspurner. Minimally invasive mitral valve repair for functional mitral regurgitation. *European journal of cardio-thoracic surgery : official journal of the European Association for Cardio-thoracic Surgery*, 55(Suppl 1):i17–i25, 2019. doi: 10.1093/ejcts/ezy344.

A. B. Goldstone, P. Atluri, W. Y. Szeto, A. Trubelja, J. L. Howard, J. W. MacArthur, C. Newcomb, J. P. Donnelly, D. M. Kobrin, M. A. Sheridan, C. Powers, R. C. Gorman, J. H. Gorman, A. Pochettino, J. E. Bavaria, M. A. Acker, W. C. Hargrove, and Y. J. Woo. Minimally invasive approach provides at least equivalent results for surgical correction of mitral regurgitation: a propensity-matched comparison. *The Journal of thoracic and cardiovascular surgery*, 145 (3):748–756, 2013. doi: 10.1016/j.jtcvs.2012.09.093.

C. Gollmann-Tepeköylü, J. Holfeld, G. Pölzl, B. Metzler, F. Hintringer, A. Adukauskaite, M. Stijnen, S. van Tuijl, L. Müller, M. Grimm, and N. Bonaros. Beating heart porcine high-fidelity simulator for the training of edge-to-edge mitral valve repair. *Multimedia manual of cardiothoracic surgery : MMCTS*, 2018, 2018. doi: 10.1510/mmcts.2018.045.

P. G. Hagan, C. A. Nienaber, E. M. Isselbacher, D. Bruckman, D. J. Karavite, P. L. Russman, A. Evangelista, R. Fattori, T. Suzuki, J. K. Oh, A. G. Moore, J. F. Malouf, L. A. Pape, C. Gaca, U. Sechtem, S. Lenferink, H. J. Deutsch, H. Diedrichs, J. Marcos y Robles, A. Llovet, D. Gilon, S. K. Das, W. F. Armstrong, G. M. Deeb, and K. A. Eagle. The international registry of acute aortic dissection (irad): new insights into an old disease. *JAMA*, 283(7):897–903, 2000. ISSN 0098-7484. doi: 10.1001/jama.283.7.897.

S. Hashmi. *Comprehensive Materials Processing*. Elsevier Science, Burlington, 2014. ISBN 978-0-08-096533-8. URL http://www.sciencedirect.com/science/referenceworks/9780080965338.

K. Iwakura, H. Ito, S. Kawano, A. Okamura, T. Kurotobi, M. Date, K. Inoue, and K. Fujii. Comparison of orifice area by transthoracic three-dimensional doppler echocardiography versus proximal isovelocity surface area (pisa) method for assessment of mitral regurgitation. *The American journal of cardiology*, 97(11):1630–1637, 2006. ISSN 0002-9149. doi: 10.1016/j.amjcard.2005.12.065.

H. Javadikasgari, R. M. Suri, B. Tappuni, and A. M. Gillinov. Minimally invasive mitral valve repair. *Heart (British Cardiac Society)*, 104(10):861–867, 2018. doi: 10.1136/heartjnl-2016-310774.

R. Karl, G. Romano, J. Marx, M. Eden, P. Schlegel, L. Stroh, S. Fischer, M. Hehl, R. Kühle, L. Mohl, M. Karck, N. Frey, R. de Simone, and S. Engelhardt. An ex-vivo and in-vitro dynamic simulator for surgical and transcatheter mitral valve interventions. *International journal of computer assisted radiology and surgery*, 19(3):411–421, 2024. doi: 10.1007/s11548-023-03036-4.

J. K. Kirklin. *Kirklin/Barratt-Boyes Cardiac Surgery: Expert Consult - Online and Print (2-Volume Set)*. Elsevier - Health Sciences Division, Philadelphia, 4th ed. edition, 2013. ISBN 978-1-4160-6391-9. URL https://ebookcentral.proquest.com/lib/kxp/detail.action?docID=1431082.

R. Kramme, editor. *Medizintechnik*. Springer Berlin Heidelberg, Berlin, Heidelberg, 2017. ISBN 978-3-662-48770-9. doi: 10.1007/978-3-662-48771-6.

R. Kramme and H. Kramme. medizintechnik@ein.querschnitt.de. In R. Kramme, editor, *Medizintechnik*, pages 3–6. Springer Berlin Heidelberg, Berlin, Heidelberg, 2017. ISBN 978-3-662-48770-9. doi: 10.1007/978-3-662-48771-6{\textunderscore}1.

P. Lancellotti, L. Moura, L. A. Pierard, E. Agricola, B. A. Popescu, C. Tribouilloy, A. Hagendorff, J.-L. Monin, L. Badano, and J. L. Zamorano. European association of echocardiography recommendations for the assessment of valvular regurgitation. part 2: mitral and tricuspid regurgitation (native valve disease). *European journal of echocardiography : the journal of the Working Group on Echocardiography of the European Society of Cardiology*, 11(4):307–332, 2010. doi: 10.1093/ejechocard/jeq031.

R. Lange, B. Voss, V. Kehl, D. Mazzitelli, P. Tassani-Prell, and T. Günther. Right minithoracotomy versus full sternotomy for mitral valve repair: A propensity matched comparison. *The Annals of thoracic surgery*, 103(2):573–579, 2017. doi: 10.1016/j.athoracsur.2016.06.055.

H. Layoun, S. C. Harb, A. Krishnaswamy, R. Miyasaka, J. Yun, and S. R. Kapadia. Patient selection for mitral transcatheter edge-to-edge repair. *Methodist DeBakey cardiovascular journal*, 19(3):26–36, 2023. doi: 10.14797/mdcvj.1199.

J. W. Lee, I. H. Lee, and D.-W. Cho. Development of micro-stereolithography technology using metal powder. *Microelectronic Engineering*, 83(4-9):1253–1256, 2006. ISSN 01679317. doi: 10.1016/j.mee.2006.01.192.

R. Leibuss, O. Posredņikova, I. Pupkeviča, K. Meidrops, D. Mackevičs, Y. Dekhtyar, P. Stradiņš, and E. Strīķe. Transcranial duplex ultrasonography measurements towards identification of blood vessel conditions: Artificial cerebral blood flow in pathologies. *Proceedings of the Latvian Academy of Sciences. Section B. Natural, Exact, and Applied Sciences.*, 76(3): 346–351, 2022. doi: 10.2478/prolas-2022-0052.

R. Leister, R. Karl, L. Stroh, D. Mereles, M. Eden, L. Neff, R. de Simone, G. Romano, J. Kriegseis, M. Karck, N. Frey, B. Frohnapfel, A. Stroh, and S. Engelhardt. Investigating the shortcomings of the flow convergence method for quantification of mitral regurgitation in a pulsatile in-vitro environment and with computational fluid dynamics, 2024. URL `http://arxiv.org/pdf/2403.05224`.

A. Leśniak-Sobelga, M. Olszowska, P. Podolec, and W. Tracz. Ilościowa ocena niedomykalności mitralnej–porównanie metody echokardiograficznej i angiograficznej. *Przeglad lekarski*, 59(9):770–773, 2002. ISSN 0033-2240.

N. Lichtenberg, P. Eulzer, G. Romano, A. Brčić, M. Karck, K. Lawonn, R. de Simone, and S. Engelhardt. Mitral valve flattening and parameter mapping for patient-specific valve diagnosis. *International journal of computer assisted radiology and surgery*, 15(4):617–627, 2020. doi: 10.1007/s11548-019-02114-w.

C. D. Little, E. C. Mackle, E. Maneas, D. Chong, D. Nikitichev, J. Constantinou, J. Tsui, G. Hamilton, R. D. Rakhit, T. M. Mastracci, and A. E. Desjardins. A patient-specific multi-modality abdominal aortic aneurysm imaging phantom. *International journal of computer assisted radiology and surgery*, 17(9):1611–1617, 2022. doi: 10.1007/s11548-022-02612-4{\#}Sec1.

K. M. Meess, R. L. Izzo, M. L. Dryjski, R. E. Curl, L. M. Harris, M. Springer, A. H. Siddiqui, S. Rudin, and C. N. Ionita. 3d printed abdominal aortic aneurysm phantom for image guided surgical planning with a patient specific fenestrated endovascular graft system. *Proceedings of SPIE–the International Society for Optical Engineering*, 10138, 2017. ISSN 0277-786X. doi: 10.1117/12.2253902.

M. Mirabel, B. Iung, G. Baron, D. Messika-Zeitoun, D. Détaint, J.-L. Vanoverschelde, E. G. Butchart, P. Ravaud, and A. Vahanian. What are the characteristics of patients with severe, symptomatic, mitral regurgitation who are denied surgery? *European heart journal*, 28 (11):1358–1365, 2007. doi: 10.1093/eurheartj/ehm001.

J. Mireles, H.-C. Kim, Hwan Lee in , D. Espalin, F. Medina, E. MacDonald, and R. Wicker. Development of a fused deposition modeling system for low melting temperature metal alloys. *Journal of Electronic Packaging*, 135(1), 2013. ISSN 1043-7398. doi: 10.1115/1.4007160.

D. S. Mix, M. C. Stoner, S. W. Day, and M. S. Richards. Manufacturing abdominal aorta hydrogel tissue-mimicking phantoms for ultrasound elastography validation. *Journal of visualized experiments : JoVE*, (139), 2018. doi: 10.3791/57984.

L. Mohl, R. Karl, M. N. Hagedorn, A. Runz, S. Skornitzke, M. Toelle, C. S. Bergt, J. Hatzl, C. Uhl, D. Böckler, K. Meisenbacher, and S. Engelhardt. Simulation of thoracic endovascular aortic repair in a perfused patient-specific model of type b aortic dissection. *International journal of computer assisted radiology and surgery*, 2024. doi: 10.1007/s11548-024-03190-3.

M. Müller, Q.-U. Huynh, E. Uhlmann, and M. H. Wagner. Study of inkjet printing as additive manufacturing process for gradient polyurethane material. *Production Engineering*, 8(1-2):25–32, 2014. ISSN 0944-6524. doi: 10.1007/s11740-013-0504-0.

E. Nader, S. Skinner, M. Romana, R. Fort, N. Lemonne, N. Guillot, A. Gauthier, S. Antoine-Jonville, C. Renoux, M.-D. Hardy-Dessources, E. Stauffer, P. Joly, Y. Bertrand, and P. Connes. Blood rheology: Key parameters, impact on blood flow, role in sickle cell disease and effects of exercise. *Frontiers in physiology*, 10:1329, 2019. ISSN 1664-042X. doi: 10.3389/fphys.2019.01329.

G. Nickenig, F. W. Mohr, M. Kelm, K.-H. Kuck, P. Boekstegers, J. Hausleiter, W. Schillinger, J. Brachmann, R. Lange, and H. Reichenspurner. Konsensus der deutschen gesellschaft für kardiologie – herz- und kreislaufforschung – und der deutschen gesellschaft für thorax-, herz- und gefäßchirurgie zur behandlung der mitralklappeninsuffizienz. *Der Kardiologe*, 7(2):76–90, 2013. ISSN 1864-9718. doi: 10.1007/s12181-013-0488-1.

V. T. Nkomo, J. M. Gardin, T. N. Skelton, J. S. Gottdiener, C. G. Scott, and M. Enriquez-Sarano. Burden of valvular heart diseases: a population-based study. *Lancet (London, England)*, 368(9540):1005–1011, 2006. doi: 10.1016/S0140-6736(06)69208-8.

M. J. Paulsen, J. H. Bae, A. M. Imbrie-Moore, H. Wang, C. E. Hironaka, J. M. Farry, H. Lucian, A. D. Thakore, M. R. Cutkosky, and Y. Joseph Woo. Development and ex vivo validation of novel force-sensing neochordae for measuring chordae tendineae tension in the mitral valve apparatus using optical fibers with embedded bragg gratings. *Journal of biomechanical engineering*, 142(1):0145011–0145019, 2020. doi: 10.1115/1.4044142.

T. J. Pedley. *The Fluid Mechanics of Large Blood Vessels*. Cambridge University Press, 2012. ISBN 9780521226264. doi: 10.1017/CBO9780511896996.

M. Raffel, C. E. Willert, F. Scarano, C. J. Kähler, S. T. Wereley, and J. Kompenhans, editors. *Particle Image Velocimetry*. Springer International Publishing, Cham, 2018. ISBN 978-3-319-68851-0. doi: 10.1007/978-3-319-68852-7.

A. Ramella, F. Migliavacca, J. F. Rodriguez Matas, F. Heim, F. Dedola, S. Marconi, M. Conti, S. Allievi, T. J. Mandigers, D. Bissacco, M. Domanin, S. Trimarchi, and G. Luraghi. Validation and verification of high-fidelity simulations of thoracic stent-graft implantation. *Annals of biomedical engineering*, 50(12):1941–1953, 2022. doi: 10.1007/s10439-022-03014-y.

E. Rodriguez, R. Raissi, M. Bott, and M. A. Morse. Mitraclip™: a step by step guide for surgeons. *Annals of cardiothoracic surgery*, 10(1):180–182, 2021. ISSN 2225-319X. doi: 10.21037/acs-2020-mv-19.

A. Rohani Shirvan, A. Nouri, and C. Wen. Structural polymer biomaterials. In *Structural Biomaterials*, pages 395–439. Elsevier, 2021. ISBN 9780128188316. doi: 10.1016/B978-0-12-818831-6.00010-0.

G. A. Roth, G. A. Mensah, C. O. Johnson, G. Addolorato, E. Ammirati, L. M. Baddour, N. C. Barengo, A. Z. Beaton, E. J. Benjamin, C. P. Benziger, A. Bonny, M. Brauer, M. Brodmann, T. J. Cahill, J. Carapetis, A. L. Catapano, S. S. Chugh, L. T. Cooper, J. Coresh, M. Criqui, N. DeCleene, K. A. Eagle, S. Emmons-Bell, V. L. Feigin, J. Fernández-Solà, G. Fowkes, E. Gakidou, S. M. Grundy, F. J. He, G. Howard, F. Hu, L. Inker, G. Karthikeyan, N. Kassebaum, W. Koroshetz, C. Lavie, D. Lloyd-Jones, H. S. Lu, A. Mirijello, A. M. Temesgen, A. Mokdad, A. E. Moran, P. Muntner, J. Narula, B. Neal, M. Ntsekhe, G. Moraes de Oliveira, C. Otto, M. Owolabi, M. Pratt, S. Rajagopalan, M. Reitsma, A. L. P. Ribeiro, N. Rigotti, A. Rodgers, C. Sable, S. Shakil, K. Sliwa-Hahnle, B. Stark, J. Sundström, P. Timpel, I. M. Tleyjeh, M. Valgimigli, T. Vos, P. K. Whelton, M. Yacoub, L. Zuhlke, C. Murray, and V. Fuster. Global burden of cardiovascular diseases and risk factors, 1990-2019: Update from the gbd 2019 study. *Journal of the American College of Cardiology*, 76(25):2982–3021, 2020. doi: 10.1016/j.jacc.2020.11.010.

P. A. Rudenick, B. H. Bijnens, D. García-Dorado, and A. Evangelista. An in vitro phantom study on the influence of tear size and configuration on the hemodynamics of the lumina in chronic type b aortic dissections. *Journal of vascular surgery*, 57(2):464–474.e5, 2013. doi: 10.1016/j.jvs.2012.07.008.

P. Rynio, A. Kazimierczak, T. Jedrzejczak, and P. Gutowski. A 3d printed aortic arch template to facilitate decision-making regarding the use of an externalized transapical wire during thoracic endovascular aneurysm repair. *Annals of vascular surgery*, 54:336.e5–336.e8, 2019. doi: 10.1016/j.avsg.2018.06.021.

M. Salmi, K.-S. Paloheimo, J. Tuomi, J. Wolff, and A. Mäkitie. Accuracy of medical models made by additive manufacturing (rapid manufacturing). *Journal of cranio-maxillo-facial surgery : official publication of the European Association for Cranio-Maxillo-Facial Surgery*, 41(7):603–609, 2013. doi: 10.1016/j.jcms.2012.11.041.

H. Samavat and J. A. Evans. An ideal blood mimicking fluid for doppler ultrasound phantoms. *Journal of medical physics*, 31(4):275–278, 2006. ISSN 0971-6203. doi: 10.4103/0971-6203.29198.

P. Sardari Nia, J. H. T. Daemen, and J. G. Maessen. Development of a high-fidelity minimally invasive mitral valve surgery simulator. *The Journal of thoracic and cardiovascular surgery*, 157(4):1567–1574, 2019. doi: 10.1016/j.jtcvs.2018.09.014.

D. Schmauss, G. Juchem, S. Weber, N. Gerber, C. Hagl, and R. Sodian. Three-dimensional printing for perioperative planning of complex aortic arch surgery. *The Annals of thoracic surgery*, 97(6):2160–2163, 2014. doi: 10.1016/j.athoracsur.2014.02.011.

A. Sengupta, S. L. Alexis, S. Zaid, G. H. L. Tang, S. Lerakis, and R. P. Martin. Imaging the mitral valve: a primer for the interventional surgeon. *Annals of cardiothoracic surgery*, 10 (1):28–42, 2021. ISSN 2225-319X. doi: 10.21037/acs-2020-mv-16.

M. L. Shofner, K. Lozano, F. J. Rodríguez-Macías, and E. V. Barrera. Nanofiber–reinforced polymers prepared by fused deposition modeling. *Journal of Applied Polymer Science*, 89 (11):3081–3090, 2003. ISSN 0021-8995. doi: 10.1002/app.12496.

D. J. Simkin, J. A. Greene, J. Jung, B. C. Sacks, and H. E. Fessler. The death of animals in medical school. *The New England journal of medicine*, 376(8):713–715, 2017. doi: 10.1056/NEJMp1612992.

W. C. Smith and R. W. Dean. Structural characteristics of fused deposition modeling polycarbonate material. *Polymer Testing*, 32(8):1306–1312, 2013. ISSN 01429418. doi: 10.1016/j.polymertesting.2013.07.014.

K. N. Sommer, L. Shepard, N. V. Karkhanis, V. Iyer, E. Angel, M. F. Wilson, F. J. Rybicki, D. Mitsouras, S. Rudin, and C. N. Ionita. 3d printed cardiovascular patient specific phantoms used for clinical validation of a ct-derived ffr diagnostic software. *Proceedings of SPIE–the International Society for Optical Engineering*, 10578, 2018. ISSN 0277-786X. doi: 10.1117/12.2292736.

S. J. Sonntag, W. Li, M. Becker, W. Kaestner, M. R. Büsen, N. Marx, D. Merhof, and U. Steinseifer. Combined computational and experimental approach to improve the assessment of mitral regurgitation by echocardiography. *Annals of biomedical engineering*, 42(5):971–985, 2014. doi: 10.1007/s10439-013-0968-2.

P. C. Spittell, J. A. Spittell, J. W. Joyce, A. J. Tajik, W. D. Edwards, H. V. Schaff, and A. W. Stanson. Clinical features and differential diagnosis of aortic dissection: experience with 236 cases (1980 through 1990). *Mayo Clinic proceedings*, 68(7):642–651, 1993. ISSN 0025-6196. doi: 10.1016/S0025-6196(12)60599-0.

W. Y. Szeto, M. McGarvey, A. Pochettino, G. W. Moser, A. Hoboken, K. Cornelius, E. Y. Woo, J. P. Carpenter, R. M. Fairman, and J. E. Bavaria. Results of a new surgical paradigm: endovascular repair for acute complicated type b aortic dissection. *The Annals of thoracic surgery*, 86(1):87–93; discussion 93–4, 2008. doi: 10.1016/j.athoracsur.2008.04.003.

TGHDoA. Tee: Standard views, 2014. URL `https://pie.med.utoronto.ca/tee/TEE_content/assets/applications/standardViewsHTML5/TEE-HTML5-SV/index.html`.

P. Thavendiranathan, D. Phelan, P. Collier, J. D. Thomas, S. D. Flamm, and T. H. Marwick. Quantitative assessment of mitral regurgitation: how best to do it. *JACC. Cardiovascular imaging*, 5(11):1161–1175, 2012. doi: 10.1016/j.jcmg.2012.07.013.

Y.-H. Tong, T. Yu, M.-J. Zhou, C. Liu, M. Zhou, Q. Jiang, C.-J. Liu, X.-Q. Li, and Z. Liu. Use of 3d printing to guide creation of fenestrations in physician-modified stent-grafts for treatment of thoracoabdominal aortic disease. *Journal of endovascular therapy : an official journal of the International Society of Endovascular Specialists*, 27(3):385–393, 2020. doi: 10.1177/1526602820917960.

Y. Topilsky. Mitral regurgitation: Anatomy, physiology, and pathophysiology-lessons learned from surgery and cardiac imaging. *Frontiers in cardiovascular medicine*, 7:84, 2020. ISSN 2297-055X. doi: 10.3389/fcvm.2020.00084.

I. O. Torres and N. de Luccia. A simulator for training in endovascular aneurysm repair: The use of three dimensional printers. *European journal of vascular and endovascular surgery : the official journal of the European Society for Vascular Surgery*, 54(2):247–253, 2017. doi: 10.1016/j.ejvs.2017.05.011.

T. T. Tsai, R. Fattori, S. Trimarchi, E. Isselbacher, T. Myrmel, A. Evangelista, S. Hutchison, U. Sechtem, J. V. Cooper, D. E. Smith, L. Pape, J. Froehlich, A. Raghupathy, J. L. Januzzi, K. A. Eagle, and C. A. Nienaber. Long-term survival in patients presenting with type b acute aortic dissection: insights from the international registry of acute aortic dissection. *Circulation*, 114(21):2226–2231, 2006. doi: 10.1161/CIRCULATIONAHA.106.622340.

G. R. Upchurch, G. A. Escobar, A. Azizzadeh, A. W. Beck, M. F. Conrad, J. S. Matsumura, M. H. Murad, R. J. Perry, M. J. Singh, R. K. Veeraswamy, and G. J. Wang. Society for vascular surgery clinical practice guidelines of thoracic endovascular aortic repair for descending thoracic aortic aneurysms. *Journal of vascular surgery*, 73(1S):55S–83S, 2021. doi: 10.1016/j.jvs.2020.05.076.

J. Urbina, J. A. Sotelo, D. Springmüller, C. Montalba, K. Letelier, C. Tejos, P. Irarrázaval, M. E. Andia, R. Razavi, I. Valverde, and S. A. Uribe. Realistic aortic phantom to study hemodynamics using mri and cardiac catheterization in normal and aortic coarctation conditions. *Journal of magnetic resonance imaging : JMRI*, 44(3):683–697, 2016. doi: 10.1002/jmri.25208.

A. Vahanian, F. Beyersdorf, F. Praz, M. Milojevic, S. Baldus, J. Bauersachs, D. Capodanno, L. Conradi, M. de Bonis, R. de Paulis, V. Delgado, N. Freemantle, M. Gilard, K. H. Haugaa, A. Jeppsson, P. Jüni, L. Pierard, B. D. Prendergast, J. R. Sádaba, C. Tribouilloy, and W. Wojakowski. 2021 esc/eacts guidelines for the management of valvular heart disease. *European heart journal*, 43(7):561–632, 2022. doi: 10.1093/eurheartj/ehab395.

J. M. Ward, S. Cherian, and M. A. Linden. Hematopoietic and lymphoid tissues. In *Comparative Anatomy and Histology*, pages 365–401. Elsevier, 2018. ISBN 9780128029008. doi: 10.1016/B978-0-12-802900-8.00019-1.

C. Westbrook. Calculate density and viscosity of glycerol/water mixtures, 2018. URL `http://www.met.reading.ac.uk/~sws04cdw/viscosity_calc.html`.

N. Yang. On the importance of proper window and level settings in temporal bone ct imaging. *Philippine Journal of Otolaryngology Head and Neck Surgery*, 35(2):51, 2020. ISSN 1908-4889. doi: 10.32412/pjohns.v35i2.1523.

K. Zilles and B. N. Tillmann. *Anatomie*. Springer Berlin Heidelberg, Berlin, Heidelberg, 2010. ISBN 978-3-540-69481-6. doi: 10.1007/978-3-540-69483-0.

J. M. Zimmermann, M. Arduini, L. Vicentini, F. Maisano, and M. Meboldt. Transcatheter mitral valve repair simulator equipped with eye tracking based performance assessment capabilities: A pilot study. *Cardiovascular engineering and technology*, 12(5):530–538, 2021. doi: 10.1007/s13239-021-00549-4{\#}Sec2.

W. A. Zoghbi, D. Adams, R. O. Bonow, M. Enriquez-Sarano, E. Foster, P. A. Grayburn, R. T. Hahn, Y. Han, J. Hung, R. M. Lang, S. H. Little, D. J. Shah, S. Shernan, P. Thavendiranathan, J. D. Thomas, and N. J. Weissman. Recommendations for noninvasive evaluation of native valvular regurgitation: A report from the american society of echocardiography developed in collaboration with the society for cardiovascular magnetic resonance. *Journal of the American Society of Echocardiography : official publication of the American Society of Echocardiography*, 30(4):303–371, 2017. doi: 10.1016/j.echo.2017.01.007.

8 Personal contribution to data acquisition / assessment and personal publications

8.1 Contributions to the mitral valve simulator

The design, manufacturing process, and validation experiments of the mitral valve simulator were entirely and solely conducted by myself or under my supervision. All experiments were orchestrated by myself, while the medical interventions were obtained by physicians. All data was collected, processed, and evaluated solely by myself.

8.2 Contributions to the assessment of the flow convergence method

The design, manufacturing process, and validation experiments of the mitral valve simulator were entirely and solely conducted by myself or under my supervision. The comparison between transesophageal echocardiography and particle image velocimetry to evaluate the flow convergence method was carried out in collaboration with the Institute of Fluid Mechanics at the Karlsruhe Institute of Technology. The transesophageal echocardiography experiments with experts were organized, conducted, and analyzed by me. The particle image velocimetry experiments were planned collaboratively by myself and the Institute of Fluid Mechanics. The execution and evaluation of the experiments were performed by the Institute of Fluid Mechanics.

8.3 Contributions to the aortic simulator

Segments of this comprehensive project were addressed within the framework of an as-yet-unpublished medical dissertation authored by Mr. Lukas Mohl, under Jun. Prof. Sandy Engelhardt's and my supervision. The development of the aortic simulator rested within my domain of responsibility, wherein the technical evolution and implementation of the simulator were orchestrated. Conversely, the development and evaluation of the aortic phantom was undertaken by Mr. Lukas Mohl, encompassing the conception, design, and realization of this counterpart.
Mr. Lukas Mohl orchestrated and planned the flow and pressure measurement experiments. The data was collected in equal collaboration. Processing and analyzing the flow and pressure data was done by myself. I solely conducted the computed tomography angiography tests, gathering and processing the corresponding data. The planning, execution, evaluation, and data processing of the thoracic endovascular repair and digital subtraction angiography were collaborative efforts between Mr. Lukas Mohl and myself.

8.4 Publications related to thesis

8.4.1 First author journal publications directly related to thesis

Roger Karl, Gabriele Romano, Josephin Marx, Matthias Eden, Philipp Schlegel, Lubov Stroh, Samantha Fischer, Maximilian Hehl, Reinald Kühle, Matthias Karck, Norbert Frey, Raffaele De Simone Raffaele, Sandy Engelhardt.
An ex-vivo and in-vitro dynamic simulator for surgical and transcatheter mitral valve interventions
International Journal of Computer Assisted Radiology and Surgery, 19(3):411-421, 2024. doi: 10.1007/s11548-023-03036-4 .

Robin Leister[1], **Roger Karl**[1], Lubov Stroh, Derliz Mereles, Matthias Eden, Luis Neff, Raffaele de Simone, Gabriele Romano, Jochen Kriegseis, Matthias Karck, Norbert Frey, Bettina Frohnapfel, Alexander Stroh, Sandy Engelhardt.
Investigating the shortcomings of the Flow Convergence Method for quantification of Mitral Regurgitation in a pulsatile in-vitro environment and with Computational Fluid Dynamics
Preprint is available on arXiv: 2403.05224v2. Manuscript submitted to *Cardiovascular Engineering and Technology.*

Lukas Mohl[1], **Roger Karl**[1], Matthias Hagedorn, Armin Runz, Stephan Skornitzke, Malte Toelle, Carl Soeren Bergt, Johannes Hatzl, Christian Uhl, Dittmar Böckler, Katrin Meißenbacher, Sandy Engelhardt.
Simulation of thoracic endovascular aortic repair in a perfused patient-specific model of type B aortic dissection
International Journal of Computer Assisted Radiology and Surgery, 2024. doi: 10.1007/s11548-024-03190-3 .

8.4.2 Awards

Roger Karl, Lalith Sharan, Samantha Fischer, Josephine Marx, Julian Brand, Maximilian Hehl, Gabriele Romano, Raffaele De Simone, Sandy Engelhardt
Patient-specific Mitral Valve Simulation to Support Therapy
***Poster** at Informatics for Life annual meeting in Heidelberg, Germany - 2021 **1st place poster award**.*

Lubov Stroh, **Roger Karl**, Robin Leister, Derliz Mereles, Matthias Eden, Luis Neff, Raffaele de Simone, Gabriele Romano, Alexander Stroh, Jochen Kriegseis, Matthias Karck, Norbert Frey, Markus Weigand, Christoph Lichtenstern, Bettina Frohnapfel, Sandy Engelhardt

[1] These authors contributed equally.

Comparison of Transesophageal Echocardiography and Particle Image Velocimetry to quantify Mitral Regurgitation in a High-Fidelity Environment
Poster *at the 35th fall meeting of the wissenschtlicher Arbeitskreis Kardioanästhesie in Fulda, Germany - 2023* ***2nd place AbbVie poster award.***

8.4.3 Publications related to patient-specific simulations

Lukas Burger[1], Lalith Sharan[1], **Roger Karl**, Christina Wang, Matthias Karck, Raffaele De Simone, Ivo Wolf, Gabriele Romano, Sandy Engelhardt.
Comparative evaluation of three commercially available depth sensors for close-range use in surgical simulation.
Presented at the 14th International Conference on Information Processing in Computer-Assisted Interventions in Munich, Germany, 2023.
International Journal of Computer Assisted Radiology and Surgery, 18(6):1109–1118, 2023. doi: 10.1007/s11548-023-02887-1

Christina Wang, **Roger Karl**, Lalith Sharan, Andela Grizelj, Samantha Fischer, Matthias Karck, Raffaele De Simone, Gabriele Romano[1], Sandy Engelhardt[1].
Surgical Training of Minimally Invasive Mitral Valve Repair on a Patient-Specific Simulator Improves Surgical Skills
European Journal of Cardio-Thoracic Surgery, 65(3), 2023. doi: 10.1093/ejcts/ezad387

8.4.4 Publications related to echocardiography to diagnose and grade mitral regurgitation

Josephin Marx, Andela Grizelj, Christoph Lichtenstern, **Roger Karl**, Derliz Mereles, Philippe Grieshaber, Mathias Konstandin, Philipp Schlegel, Philip Raake, Samantha Fischer, Norbert Frey, Matthias Karck, Raffaele De Simone, Gabriele Romano, Lalith Sharan, Sandy Engelhardt.
Unrolled mitral valve visualization and quantification to assess geometric modification after surgical repair and catheter-based interventional procedures
Manuscript in preparation for submission.

8.4.5 Talks, poster, abstracts

Roger Karl, Gabriele Romano, Raffaele De Simone, Mathias Konstandin, Philipp Schlegel, Philip Raake, Josephin Marx, Maximilian Hehl, Reinald Kühle, Frederic Weichel, Mats Scheurer, Matthias Karck, Norbert Frey, Sandy Engelhardt
Towards Hemodynamic Simulation for Surgical and Interventional Training and Patient-Specific Preoperative Planning
Talk *at Young DZHK partnerside retreat in Heidelberg, Germany, 2022.*

[1] These authors contributed equally.

Roger Karl, Gabriele Romano, Matthias Eden, Philipp Schlegel, Lubov Stroh, Josephin Marx, Samantha Fischer, Maximilian Hehl, Reinald Kühle, Matthias Karck, Norbert Frey, Raffaele De Simone, Sandy Engelhardt
An ex-vivo and in-vitro dynamic simulator for surgical and transcatheter mitral valve interventions
Poster *at Informatics for Life annual meeting in Heidelberg, Germany, 2022.*

Lukas Mohl, **Roger Karl**, Armin Runz, Matthias Hagedorn, Stephan Skornitzke, Malte Toelle, Johannes Hatzl, Katrin Meißenbacher, Christian Uhl, Dittmar Böckler, Sandy Engelhardt.
3d-printed Patient-specific Aortic Dissection Model for Training of endovascular interventions
Abstract *at the 14th CARS conference in Munich, Germany, 2023.*

Roger Karl
Medical 3D Printing für die Interventionsplanung
Invited Talk *at eCardiology at the Deutsche Gesellschaft für Kardiologie – Herz- und Kreislaufforschung e.V. (DGK) annual meeting in Mannheim, Germany 2023.*

Christina Wang, **Roger Karl**, Matthias Karck, Raffaele De Simone, Gabriele Romano, Sandy Engelhardt.
Quantification of the Learning Progress in Minimally Invasive Mitral Valve Repair on a Patient-Specific Simulator
Abstract *at the Deutsche Gesellschaft für Kardiologie – Herz- und Kreislaufforschung e.V. (DGK) annual meeting in Mannheim, Germany, 2023.*

Matthias Niklas Hagedorn, Katrin Meisenbacher, Lukas Mohl, **Roger Karl**, Armin Runz, Johannes Hatzl, Christian Uhl, Sandy Engelhardt, Dittmar Böckler.
3D-gedruckte, patientenspezifische und perfundierte Aortenmodelle zur Simulation der Implantation thorakaler Endoprothesen bei Patienten mit Standford Typ B Dissektionen
Abstract *at the Deutsche Gesellschaft für Gefäßchirurgie und Gefäßmedizin (DGG) annul meeting in Osnabrück, Germany, 2023.*

Curriculum Vitae

Name:	Roger Frederick Karl
Date of birth:	November 12^{th} 1992
Place of birth	Mannheim
Nationality	German

Education and Studies

2003 - 2012	Abitur, Carl-Benz-Gymnasium Ladenburg
2012	Higher Education Entrance Qualification (Grade 2.0)
2012 - 2019	Bachelor- and Master Studies Mechanical Engineering Karlsruhe Institute of Technology
2019	Master Thesis (Grade 1.0) Institute of Mobile Machines, Karlsruhe Institute of Technology
2019	Master of Science Certificate (Grade 1.5)
since 2020	PhD Studies University Hospital Heidelberg Working Group Artificial Intelligence in Cardiovascular Medicine Head of Group Jun. Prof. Dr. Sandy Engelhardt

Stays Abroad

2018 - 2019	Master's Thesis at ZF Windpower in Lommel, Belgium

Scholarships

2017 - 2019	stipendium@ZF, ZF Friedrichshafen AG

Acknowledgments

Liebe Sandy, vier Jahre Doktorarbeit neigen sich dem Ende. Vielen Dank, dass ich helfen durfte diese Arbeitsgruppe sowie ein Netzwerk inner- und außerhalb der der Uniklinik aufzubauen, und dem Teilbereich hemodynamische Simulation meinen Stempel mitaufzudrücken. Vor allem aber möchte ich dir danken für die Freiräume, die du mir gegeben hast, nicht nur was die Arbeitszeiten und den finanziellen Rahmen angeht, sondern auch, wie ich mein Projekt gestalten will, und mit wem ich gerne zusammen arbeiten möchte. Ich hatte immer das Gefühl, dass du mir vertraust, bei meinen Entscheidungen mitgehst und mich unterstützt. Du hast dir immer meine Probleme angehört und mit mir konstruktiv nach Lösungen gesucht. Du hast mich auch nach jedem Rückschlag wieder motiviert es noch mal zu versuchen. Vielen Dank, dass du meine Doktormutter warst.

Gabriele, du bist der Grund dafür, dass ich froh bin nicht Medizin studiert zu haben. Niemals würde ich deinen Zeitplan gegen meinen tauschen und trotzdem hast du so viele Stunden, nach einer Nachtschicht, am Wochenende, spät abends, egal wann, mit mir statt mit deiner Frau verbracht. Zig mal hast du Herzen zerschnitten und wieder zusammengenäht, deine Ideen geteilt, die ich nicht mal alle umgesetzt habe, und mit mir Versuche noch und nöcher durchgeführt. Für mich, aber ich denke hier spreche ich im Namen der kompletten Arbeitsgruppe, warst und bist du ein großer Glücksfall. Grazie mille!

Liebes AICM, vielen Dank, dass ihr mich sofort aufgenommen habt. Ich hatte eine sehr schöne Zeit mit euch sowohl im Büro als auch außerhalb. Ganz besonders bedanken möchte ich mich bei euch Sven und Lalith, für eure Unterstützung sowohl in fachlichen als auch in menschlichen Belangen. Lukas B. vielen Dank für deine ganzen Botengänge, das Neustarten des Laptops, usw., ohne dich wäre so vieles sehr viel komplizierter gewesen.

Ein ganz besonderer Dank gilt auch meinen „Schützlingen“, Christina, Lukas M., Sören, Luis, Julian, Max und Sarah. Ich habe sehr viel durch euch gelernt und hoffe euch ging es umgekehrt genauso. Ich habe es sehr genossen mit euch zusammen zu arbeiten und bin gespannt wie ein Flitzebogen, wie eure Lebenswege verlaufen werden.

Ganz herzlich bedanken möchte ich mich auch bei dem eingangs erwähnten Netzwerk innerhalb der Uniklinik. Aus der Herzchirurgie möchte ich besonders Raffaele, Mina, Herrn Karck, und Frau Weber für die Unterstützung danken. In der Gefäßchirurgie gilt dieser Dank Matze und Katrin. Ein großes Dankeschön und eine Entschuldigung für die Unordnung geht an das Herzlabor, mit Karin, Tobias und Sevil, sowie and die Mund-Kiefer-Gesichtschirurgen

Reinald, Frederic und Mats. Ein großes Dankeschön geht auch in die Kardiologie, an Herr Schlegel und Matthias. Vielen Dank auch an Lubov und Derliz für euren Einsatz am Echo! Genauso wie Martin im CT! Alles Weitere würde hier leider den Rahmen sprengen, aber ich denke es wird klar, dass ich mich in der Uniklinik sehr wohl und gut aufgehoben gefühlt habe und irgendjemand immer ein offenes Ohr für meine Ideen hatte!

Neben dem Netzwerk intern, möchte ich mich auch bei meiner alten Heimat dem KIT bedanken. Vielen Dank für die Kooperation mit geht and das IAM. Ein ganz großer Dank geht natürlich an das ISTM, allen voran Robin, aber natürlich auch Alex und Jochen. Nicht nur habt ihr mir die Möglichkeit gegeben noch ein paar Mal in den Genuss meiner veganen Lieblingscurrywurst zu kommen, vielmehr auch habt ihr mir sofort das Gefühl gegeben bei euch willkommen zu sein. Es war so einfach bei und mit euch zusammen zu arbeiten. Ich hoffe wirklich von ganzem Herzen, dass diese Kooperation noch lange weitergeht!

Auch wenn Arbeit für mich nicht nur der Tausch von Lebenszeit gegen Geld ist, spielt Freizeit eine sehr wichtige Rolle in meinem Leben und die Protagonisten sind hier ganz klar meine Freunde: Keule, Horsti, Lukas H., Lukas S., Josi, Anke, Hans, Jan, Julia, Xio, Eric, Lisa. Ihr müsst euch nicht nur alles Mögliche anhören, was mich so belastet ihr seid auch noch direkt verantwortlich für die beste Zeit meines Lebens. Egal ob Liebeskummer, Doktorarbeitsfrust, Familienstress, Konzerte, WG-Partys, Ski-(Hoch)touren, Wanderungen, Kletterpartien, Rennradtouren, Reisen, einfach Abenteuer. Ich weiß gar nicht, wie ich euch dafür je genug danken kann, aber bitte hört niemals damit auf!

Liebe Familie, Mama, Papa, Jochen, Björn, Armin, Lela, Annina, und natürlich auch ihr 13 anderen Karls und Gewinner. Die Leute können ja sagen was sie wollen, aber so eine Familie hat niemand. Für jede Lebenslage, für jede Not, hier bekommt man Unterstützung. Auch wenn es bei uns häufiger mal laut ist und man auch des Öfteren mal nicht einer Meinung ist, wenn es darauf ankommt, seid ihr immer alle da! Mit euch als Familie hat man immer mindestens ein Ass im Ärmel und ich bin sehr froh, euch alle zu haben! Vielen Dank.

Und dann gibt es da noch die Familie, die man sich selbst sucht, für mich heißt dieser Teil Berit. Beri, was ich auch schreibe fühlt sich nicht angemessen an, gemessen an dem was du für mich leistest. Ich kann mir eigentlich gar nicht vorstellen, dass jemand diese Unterstützung verdient hat. Dass jemand dich verdient hat. Du bist immer da zum Lachen, zum Weinen, um über Schatten zu springen, und Welten entdecken. Danke für jeden Moment "Wir".

Eidesstattliche Versicherung

1. Bei der eingereichten Dissertation zu dem Thema
   Patient-specific hemodynamic simulators for cardiovascular therapies
   handelt es sich um meine eigenständig erbrachte Leistung.

2. Ich habe nur die angegebenen Quellen und Hilfsmittel benutzt und mich keiner unzulässigen Hilfe Dritter bedient. Insbesondere habe ich wörtlich oder sinngemäß aus anderen Werken übernommene Inhalte als solche kenntlich gemacht.

3. Die Arbeit oder Teile davon habe ich bislang nicht an einer Hochschule des In- oder Auslands als Bestandteil einer Prüfungs- oder Qualifikationsleistung vorgelegt.

4. Die Richtigkeit der vorstehenden Erklärungen bestätige ich.

5. Die Bedeutung der eidesstattlichen Versicherung und die strafrechtlichen Folgen einer unrichtigen oder unvollständigen eidesstattlichen Versicherung sind mir bekannt. Ich versichere an Eides statt, dass ich nach bestem Wissen die reine Wahrheit erklärt und nichts verschwiegen habe.

Ort und Datum

Roger Frederick Karl